OPTIMIZED SILVER NANOWIRE NETWORKS FOR TRANSPARENT SMART DEVICES

A THESIS SUBMITTED TO
THE GRADUATE SCHOOL OF NATURAL AND APPLIED SCIENCES
OF
MIDDLE EAST TECHNICAL UNIVERSITY

BY

ONURALP ÇAKIR

IN PARTIAL FULFILLMENT OF THE REQUIREMENTS
FOR
THE DEGREE OF MASTER OF SCIENCE
IN
METALLURGICAL AND MATERIALS ENGINEERING

AUGUST 2023

Approval of the thesis:

OPTIMIZED SILVER NANOWIRE NETWORKS FOR TRANSPARENT SMART DEVICES

submitted by **ONURALP ÇAKIR** in partial fulfillment of the requirements for the degree of **Master of Science** i**n Metallurgical and Materials Engineering, Middle East Technical University** by,

Prof. Dr. Halil Kalıpçılar
Dean, Graduate School of **Natural and Applied Sciences**

Prof. Dr. Ali Kalkanlı
Head of the Department, **Metallurgical and Materials Eng.**

Prof. Dr. Hüsnü Emrah Ünalan
Supervisor, **Metallurgical and Materials Eng., METU**

Assoc. Prof. Dr. Simge Çınar Aygün
Co-Supervisor, **Metallurgical and Materials Eng., METU**

Examining Committee Members:

Prof. Dr. Alpan Bek
Physics, METU

Prof. Dr. Hüsnü Emrah Ünalan
Metallurgical and Materials Eng., METU

Assoc. Prof. Dr. Simge Çınar Aygün
Metallurgical and Materials Eng., METU

Assist. Prof. Dr. Yusuf Keleştemur
Metallurgical and Materials Eng., METU

Assist. Prof. Dr. Şahin Coşkun
Metallurgical and Materials Eng., Eskisehir Osmangazi University

Date: 04.08.2023

I hereby declare that all information in this document has been obtained and presented in accordance with academic rules and ethical conduct. I also declare that, as required by these rules and conduct, I have fully cited and referenced all material and results that are not original to this work.

Name Last name : Onuralp Çakır

Signature :

ABSTRACT

OPTIMIZED SILVER NANOWIRE NETWORKS FOR TRANSPARENT SMART DEVICES

Çakır, Onuralp
Master of Science, Metallurgical and Materials Engineering
Supervisor : Prof. Dr. Hüsnü Emrah Ünalan
Co-Supervisor: Assoc. Prof. Dr. Simge Çınar Aygün

August 2023, 123 pages

In the realm of transparent conductors, transparent conducting oxides have been chief among all materials. Specifically, indium tin oxide (ITO) has reigned for a long time, seen use in many applications. However, the scarcity of indium in the Earth's crust and the innate brittleness of ITO arising from its oxide nature necessitates development of alternatives. Throughout the years, materials such as graphene, carbon nanotubes (CNTs), conductive polymers, metal meshes and metallic nanowires have been proposed as alternatives. Among metallic nanowires, silver nanowire (Ag NW) networks emerged as the strongest candidate to replace ITO. One aspect that needs to be resolved, though, is the junction resistance between two nanowires. The problem stems from the polyvinyl pyrrolidone (PVP) capping agent surrounding Ag NWs. Many researchers tried to tackle this issue by welding the nanowires together using a variety of ways. Some works were concerned with cleaning the nanowires' surface. Yet in all the works, the Ag NWs used had widely different properties such as length, diameter, PVP thickness, and network deposition methods. In this thesis, treatments with different aims, taken from the literature, were developed in-house and later applied to the same batch of Ag NWs. The realization of the effects of all reported treatments on one type of nanowires was facilitated by this approach. The two most effective methods were combined in reaching a sheet resistance of 11.4 Ω/sq, optical transmittance of 90%, and optical figure of merit (FoM) of 305. The optimized Ag NW network was first used as a current collector layer in a transparent liquid-solid interface triboelectric nanogenerator (TENG). The TENG exploited the electrification between incident water droplets and the PDMS overcoat on the Ag NWs. The generated electrical output was utilized in sensing the pH and chemical concentration of the water droplets. The device was also used as a switch to activate an Ag NW-based thin film heater. Secondly, the Ag NWs were implemented in electrochromic devices (ECDs) as the transparent conductors. WO$_3$, WO$_x$, and NiO nanoparticles were used as the electrochromic layers. WO$_x$ films provided high optical contrast and coloration efficiency. These findings display the versatility of Ag NWs in state-of-the-art applications.

Keywords: Silver Nanowires, Triboelectric Nanogenerators, Liquid-Solid Interface, Electrochromic, Electrochromic Devices

ÖZ

TRANSPARAN AKILLI CİHAZLAR İÇİN OPTİMİZE EDİLMİŞ GÜMÜŞ NANOTEL AĞLARI

Çakır, Onuralp
Yüksek Lisans, Metalurji ve Malzeme Mühendisliği
Tez Yöneticisi: Prof. Dr. Hüsnü Emrah Ünalan
Ortak Tez Yöneticisi: Doç. Dr. Simge Çınar Aygün

Ağustos 2023, 123 sayfa

Şeffaf iletken elektrotlar arasında, ince film oksitler diğer tüm malzemeler arasında öncelikli bir konumdadır. Özellikle indiyum kalay oksit (ITO), en yaygın kullanılan malzeme olarak birçok uygulamada kullanılmıştır. Bununla birlikte, ITO'nun oksit yapısından kaynaklanan gevrekliği ve indiyumun yüksek fiyatı ve az bulunurluğu, ITO'nun yerine alternatif malzemelerin araştırılmasını gerekli kılmıştır. Literatürde, grafen, karbon nanotüpler (CNT'ler), iletken polimerler, metal ağlar ve metalik nanoteller gibi malzemeler ITO'nun yerine önerilmiştir. Metalik nanoteller arasında gümüş nanoteller (Ag NW'ler), ITO'nun yerine kullanmak için en güçlü aday olarak öne çıkmıştır. AgNW'lerin etkili kullanımı önündeki bir engel, iki nanotelin arasındaki bağlantı direncidir. Bu problem, Ag NW'leri çevreleyen polivinil pirolidon (PVP) tabakasından dolayı elektron iletiminin zorlaşmasından kaynaklanmaktadır. Yapılan birtakım çalışma, nanotelleri birbirine kaynaklayarak bu sorunu çözmeye çalışmıştır. Bazı çalışmalar, nanotellerin yüzeyini PVP'den arındırma üzerinedir. Ancak yapılmış olan bütün çalışmalarda, kullanılan Ag NW'lerin uzunluk, çap, PVP kalınlığı ve yüzeye kaplama yöntemleri farklıdır. Bu tezde, literatürden taranan ve özgünce geliştirilen farklı amaçlara yönelik üretim sonrası işlemler aynı sentez ve kaplama yöntemi ile üretilmiş Ag NW ağlarına uygulanmıştır. Bu şekilde, uygulanmış olan işlemlerin tek tip Ag NW'ler üzerindeki etkinliği analiz edilmiştir. İki en etkili yöntemi birleştirerek, 11.4 Ω/sq yüzey direnci, %90 optik transmitans ve 305 optoelektronik performans (FoM) elde edilmiştir. Optimize edilmiş Ag NW ağları, önce şeffaf sıvı-katı arayüz triboelektrik nanojeneratöründe (TENG) akım toplayıcı tabaka olarak kullanılmıştır. TENG cihazı, su damlacıkları ve Ag NW'ler üzerine kaplanmış olan PDMS tabakası arasındaki yüzey elektrifikasyonu ile triboelektrik sinyal oluşturmuştur. Elde edilen çıktı, su damlacıklarının pH değeri ve kimyasal derişimini algılamak için sensör olarak kullanılmıştır. Sensör ayrıca, Ag NW'ler ile üretilmiş bir ince film ısıtıcıyı etkinleştirmek için kullanılmıştır. Ayrıca, Ag NW'ler şeffaf iletken tabakaları olarak elektrokromik cihazlarda (ECD'ler) kullanılmıştır. WO_3, WO_x ve NiO nanoparçacıkları sentezlenmiş ve elektrokromik tabakalar olarak kullanılmıştır. WO_x filmlerinin elektrokimyasal ölçümleri sonucu, yüksek optik kontrast ve renklenme etkinliği elde edilmiştir. Bulgular, Ag NW'lerin transparan elektrot gerektiren modern uygulamalarda çok yönlülüğünü göstermektedir.

Anahtar Kelimeler: Gümüş Nanotel, Triboelektrik Nanojeneratör, Sıvı-Katı Arayüzü, Elektrokromik, Elektrokromik Cihazlar

To my family,

ACKNOWLEDGMENTS

First, I would like to express my gratitude to my advisor Prof. Dr. H. Emrah Ünalan for his support, patience, and mentoring during this study. This endeavor would not have been possible without his guidance. I would also like to thank my co-advisor Assoc. Prof. Dr. Simge Çınar Aygün for her valuable inputs. Special thanks to Assist. Prof. Dr. Şahin Coşkun, with whom I learned much about everything on silver nanowires.

This work was financially supported by the Scientific and Technological Research Council of Turkey (TÜBİTAK) under grants no 119N413 and 121N708.

I am deeply indebted to Dr. Doğa Doğanay, who took me under his wings and mentored me throughout this work. I would also like to thank my lab-mates Melih Ögeday Çiçek, Caner Görür, Mete Batuhan Durukan, Onur Demircioğlu, Öykü Çetin, Ali Deniz Uçar, Tufan Bölükbaşı, Dr. Ceren Başköse, Yusuf Tutel, Serkan Koylan, Murathan Çuğunlular, Sümeyye Kandur, Eda Çevik, Behiye Demirtaş, Barkın Bayram, Ahmet Keskin, Loay Madbouly, Deniz Keskin, Şensu Tunca, Alptuğ Calasın, Dr. Yaqoob Khan, Dr. Muhammad Khan, and Dr. Alptekin Aydınlı. I'm grateful for all the good times we had together.

I would also like to thank the members of Nanooptics Research Laboratory, chief among them Prof. Dr. Alpan Bek for his support and guidance during my studies. In addition, I would like to thank Özge Demirtaş and Hilal Oğuz for their assistance.

My sincere thanks go out to my friends Mert Ertan, Aydın Tozman, Oğuz Dindar, Utku Arda Töre, Orçun Dinçer, Burak Anıl İnce, Oğuzhan Şakar, Can Özcan, Derin Mert Ataman, Berk Yiğit Demirel, and Halil Karahaliloğlu.

Finally, I owe my deepest gratitude to my parents Mustafa Çakır and Seval Çakır for their unfaltering support throughout my life, and to my sister İnci Gamze Çakır who understood me best when other couldn't. I wouldn't have achieved this without you.

TABLE OF CONTENTS

CHAPTERS

APPENDIX

LIST OF TABLES

TABLES

LIST OF FIGURES

FIGURES

CHAPTER 1

INTRODUCTION

Transparent conducting electrodes (TCEs) are electrically conductive and highly transparent in the visible light spectrum. They have been researched since the beginning of the 20th century. Baedeker reportedly[1] developed the first transparent conducting oxide (TCO) film in 1907, cadmium oxide (CdO), achieving high electrical conductivities. Scientists further explored the field of TCOs, and SnO_2-based thin films were made available on airplane windshields as de-icers by the 1930s[2]. Later, in the 1950s, indium tin oxide (ITO) was developed by Corning, which is currently the most commonly used TCO material. The demand for TCEs has been on the rise, especially in the 2010s. Nowadays, TCEs are used in applications such as photovoltaics[3], sensors[4], smart windows[5,6], thin film heaters[7], and various display screens[8–10]. With the human population increasing rapidly, there will be a surge in the need for more smart devices. Therefore, research in the field of TCEs has shifted its focus to producing high-output, low-cost electrodes. Figure 1.1 shows the TCE materials available and commonly used recently throughout the literature[11].

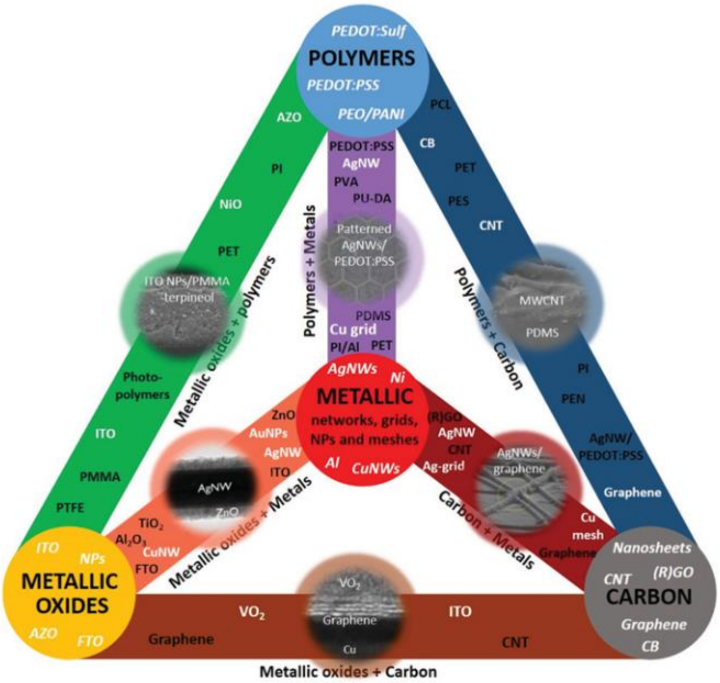

Figure 1.1 TCE materials commonly used in the literature[11].

1.1 Transparent Conducting Oxides

In the field of TCEs, TCOs have been the dominant materials, particularly ITO, fluorine-doped tin oxide (FTO), and aluminum-doped zinc oxide (AZO). ITO has been the most successful among all TCOs as it is the most commonly used and commercialized TCE material. It is a mixture of indium (III) oxide and tin (IV) oxide. Its promising optical transmittance, electrical conductivity, and excellent thermal and chemical resistance[12] have placed ITO in a prevalent position among TCEs. ITO has found vast application areas such as smartphones, smartwatches, and display screens[13]. Thin film heaters using ITO have been developed and used as defrosters as seen in Figures 1.2 (a-f)[14]. Yet, ITO suffers from some significant drawbacks in front of its widespread use. The production routes of ITO often require complex vacuum systems[15] that are not convenient for large-scale production. Physical vapor deposition (PVD)[16] and magnetron sputtering[17] are the main deposition methods of ITO. It is usual to have an annealing step during or post-deposition at a temperature above 200°C[18]. As an oxide material, ITO usually performs poorly in flexible applications, with frequent delamination[19] or cracking[20] failures upon bending. In addition, indium is a scarce element that will increase in price continuously with the growing demand for more TCEs[21]. With flexible and wearable transparent electronics also developing at their current rate, scientists have concerns about whether ITO can keep up with the escalating demand for TCEs in the near future. Many candidates emerged in the pursuit of replacing ITO with carbonaceous materials such as graphene, carbon nanotube (CNT) networks, reduced graphene oxide (rGO), conductive polymers, metallic grids, and metallic nanowire networks. The electrical, optical, and physical properties of the materials along with the manufacturing cost are decisive in the selection of these TCEs.

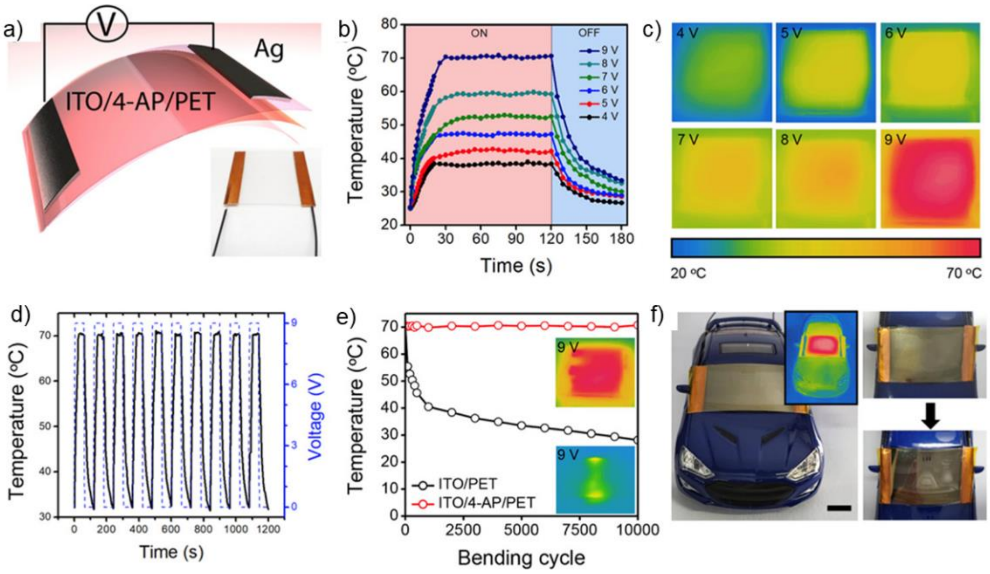

Figure 1.2 a) The schematic illustration, b) the heating and cooling curves, c) thermal camera infrared images, d) cyclic heating-cooling performance, e) mechanical test results, and f) demonstration as a defrosting device of an ITO-based thin film heater.[14]

1.2 Graphene

Carbonaceous materials have the advantage of being produced from carbon (C), one of the most abundant elements on Earth. The discovery of graphene created waves throughout the scientific community. Graphene is a 2D hexagonal structure consisting of only C atoms forming one-atom-thick sheets. It can also be described as the monolayer form of graphite. The sp^2 hybridization of C atoms allows electron transport in all directions. The high thermal and electrical conductivity combined with high flexibility made graphene a very attractive material as a TCE. Yet, there still are some issues regarding its production methods. Chemical vapor deposition (CVD) is the most commonly used method for the production of high-quality graphene thin films. Optical transmittance of up to 90% and sheet resistances of several hundred Ω/sq can be achieved by thin films grown through CVD[22], which is not conductive enough to rival ITO. CVD systems are expensive and require high-vacuum environments, which are not optimal for large-scale production. Top-down approaches involve the exfoliation of graphite into graphene sheets. Geim and Novoselov[23] first reported graphene using scotch tape to separate sheets. Since then, physical and chemical means for the exfoliation of graphene sheets have been studied to increase the amount of graphene produced. Shear exfoliation has been proposed to physically separate graphite into flakes by applying intense shear forces. Paton et al.[24] demonstrated production of few-layer graphene sheets in large quantities. Still, the sizes of the obtained flakes are often smaller than 1 µm, too small to efficiently be used in a TCE. At this stage, it should be noted that the flakes need to percolate, forming a patchwork to cover the entire substrate area. Chemical exfoliation of graphene started off by oxidizing graphite. Separating the graphene oxide (GO) layers and then reducing them into reduced graphene oxide (rGO) allowed for TCEs to be produced. The degree or reduction determines the conductivity of rGO. The sheet resistance of the rGO TCEs on their own is still high[25]. Therefore, the material was often used together with other TCE materials[26] to obtain a synergistic effect in reducing overall sheet resistance. In summary, graphene is not the strongest competitor among the candidates to replace ITO.

1.3 Carbon Nanotube Networks

Another carbonaceous material, CNTs, are one-dimensional nanomaterials akin to graphene. There are two types of CNTs, namely single-walled carbon nanotubes (SWCNTs) and multi-walled carbon nanotubes (MWCNTs). Their structure is also hexagonal and only consists of carbon atoms. CNTs possess optoelectronic properties similar to that of graphene as well. SWCNT networks are more prevalent in the field of TCEs. One issue regarding the use of SWCNT networks is the junction resistance that controls electron transfer. Junction resistance is found to be much higher than the intrinsic resistance of the material[27]. One reason is that the junctions are point contacts, and the electron transfer is similar to graphite. The other reason is that most junctions in SWCNTs are heterojunctions due to the type of SWCNTs produced. While same type of SWCNTs have near ohmic junctions, different types create a Schottky junction and significantly increase the resistance [28]. Doping the SWCNTs[29] is a popular solution for improving the optoelectronic properties of the TCEs. A competitive sheet resistance and optical transmittance of 25 Ω/sq and 90 %, respectively, were reached by Jiang et al.[30] by nitric acid (HNO_3) doping. Li et al. dual-doped the CNTs with phosphotungstic acid and gold towards fabrication of a flexible thin film heater, the characteristics of which can be seen in Figure 1.3[31]. The cyclic stability of the CNT film heater operated between 15 and 0 V is given in Figure 1.3 (a). Figure 1.3 (b) shows the temperature change upon applying a periodic voltage change starting with a cycle starting at 5 V; continuing through 0 V, 10 V, 0 V, 15 V and ending at 0 V. The long-term performance of the heater is displayed in Figure 1.3 (c), with the corresponding relative electrical resistance change during the operation time given in Figure 1.3 (d). Figure 1.3 (e) shows the defrosting process using the CNT-based heater. Still, the production of CNTs poses similar problems to that of graphene, as typically CVD processes need to be deployed. It is unlikely to produce large amounts of materials by using such vacuum processes in a short timespan.

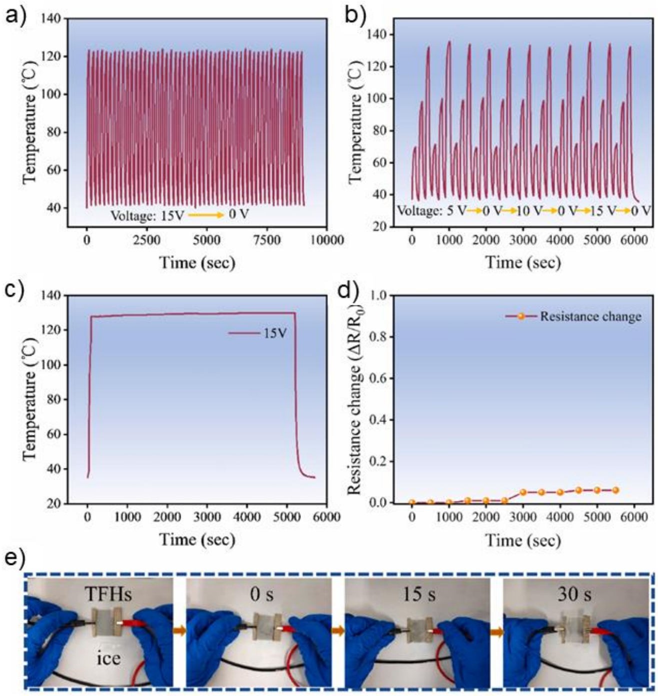

Figure 1.3 a) The cyclic stability test of the CNT film heater at applied voltage values of 15 V (on), 0 V (off); b) The cyclic stability of the film under a periodic voltage change from 5 V – 0 V – 10 V – 0 V – 15 V – 0 V for 11 cycles; c) The long term stability of the thin film at 15 V; d) The relative change in the resistance with respect to time; e) The process of defrosting, at 15 seconds no more ice remains on the film[31].

1.4 Conductive Polymers

Conductive polymers are exciting materials with high flexibility, stretchability, and solution processability. These properties piqued the interest of many researchers focused on flexible transparent electrodes in the pursuit of replacing ITO. Particularly, poly(3,4-ethylene dioxythiophene) polystyrene sulfonate (PEDOT:PSS) has been the most frequently investigated conductive polymer in the literature. Some PEDOT-based polymer TCEs[32] developed can reach a sheet resistance and optical transmittance of ~60 Ω/sq and ~89%, respectively, with 1% haze. Still, the material is not as conductive as other candidates. In addition, there are major concerns regarding its high temperature stability and moisture sensitivity[33]. Earlier studies claim PEDOT:PSS films are stable up to 150°C, and full degradation occurs at 390°C[34]. More recent studies argue that prolonged use of PEDOT:PSS films above 55°C also leads to degradation[35]. Therefore, conductive polymers are not used by themselves, but are included primarily as a supporting layer in applications such as organic solar cells[36] and strain sensors[37].

1.5 Metallic Mesh Networks

Metallic meshes are TCEs usually made from gold, silver, or copper. Considering the cost-effectiveness of the production, silver and copper are preferred. The metals can be deposited in a controlled and orderly manner using techniques such as lithography, imprinting, laser patterning, and printing techniques or randomly by crackle templates and electrospinning[38]. The controlled deposition methods allow fine-tuning of each grid unit's width, thickness, and length. The periodic pattern of each grid can also be in various geometries such as square, triangular, hexagonal, or even coffee-ring shaped. The advantage of using metallic meshes is being able to tailor a network according to the exact needs of the device. The obtained TCEs are highly competitive to ITO and other strong candidates. Some applications of the metal mesh TCEs include transparent thin film heaters[39], strain sensors[40], and electromagnetic interference shielding[41]. Such TCEs reached a sheet resistance of 6-79 Ω/sq and optical transmittances of 85-91%. Photos and characteristics of a transparent strain sensor monitoring human motion is given in Figure 1.4. Figure 1.4 (a) displays the performance of the sensor at different bending angles, and rapid finger motion. The sensing during the clenching and releasing of the fist is given in Figure 1.4 (b). The sensor could omnidirectionally sense strain and had a short response time[42]. The downsides of metallic meshes are the poor adhesion to the substrates[43], high surface roughness with thicker deposited lines, and lots of wasted material due to all the patterning done to achieve the final product. The required equipment for patterning is generally expensive as well.

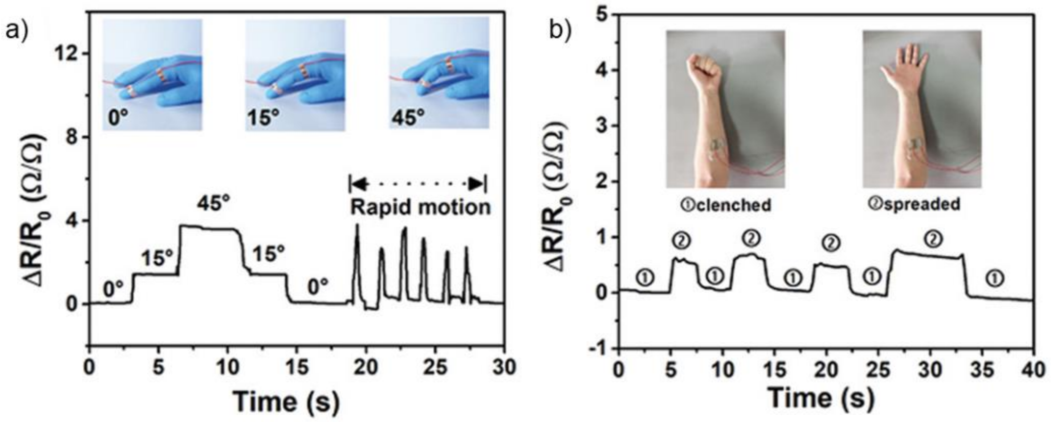

Figure 1.4 The Ag-mesh electrode sensing a) the finger bending and b) fist clenching motion[42].

1.6 Metallic Nanowire Networks

For metallic nanowire networks, the most conductive metals were first considered. Gold, copper, and silver were the ones researched the most. Metallic nanowire networks include copper[44], gold[45], and silver nanowires[46] (Ag NWs). For these 1D nanomaterials, a solution-based synthesis method was often used. However, the high cost and lesser availability of gold[47] and oxidation stability issues regarding copper nanowires[48] made Ag NWs the strongest candidate among metallic nanowires.

1.6.1 Silver Nanowires

Ag NWs were first introduced to the literature by Xia’s group in the early 2000s[46,49,50]. In the early 2010s[51], the first transparent Ag NW networks were produced successfully. Silver's electrical conductivity and color neutrality, especially in nanowire network form, gathered significant interest. Scalable solution-based techniques were often applied when synthesizing and depositing Ag NWs. The obtained TCEs competed well against the optoelectronic performance benchmarks fielded by ITO. They usually have reached >90% optical transmittance while maintaining a sheet resistance of around 20 Ω/sq. In addition, they required less material per unit area and were cost-effective and easy to manufacture. These attractive qualities have made Ag NWs the prime candidate to replace ITO in TCEs.

1.6.2 Polyol Synthesis of Silver Nanowires

While different approaches for the synthesis such as chemical[52], hydrothermal[53], and template-based[54] have been used, the self-seeded polyol synthesis of Ag NWs is the mainstream means of production[55]. In a typical Ag NW synthesis, a silver source, a reducing agent, a capping agent, and a trace amount of seeding agent are used. The polyol method is the most widely preferred means of production. In many recipes, silver nitrate ($AgNO_3$) is used as the silver source, ethylene glycol (EG) is used as both the solvent and reducing agent, and polyvinyl pyrrolidone (PVP) is used as the capping agent. Halide salts such as sodium chloride (NaCl) and sodium bromide (NaBr) are used as seeding agents. The reaction temperature for various syntheses is usually between 120 - 170°C. The high temperature allows EG to act as the reducing agent. Throughout the reaction, EG first oxidizes into glycolaldehyde and then into glyoxal. The seeding process starts with the dissolved Ag ions forming complexes with the halide ions. Ag ions get adsorbed onto clusters, and by Ostwald ripening, smaller clusters dissolve back into the solution, and larger clusters grow in size. The larger clusters form “multi-twinned particles” (MTP). Growth starts from the MTPs as more Ag ions adsorb onto the (111) planes exposed to the solution. Furthermore, PVP molecules adsorb onto the (100) planes and facilitate one-dimensional growth along the [110] direction. An illustration of the Ag NW growth is provided in Figure 1.5.

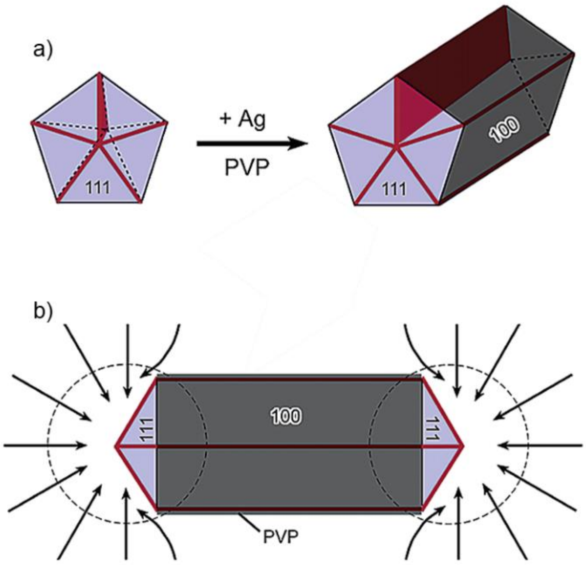

Figure 1.5 a) The growth of Ag NWs though MTPs; b) The addition of Ag atoms to the (111) planes[49].

1.6.3 Deposition of Silver Nanowire Networks

Before the deposition of Ag NWs, a purification step is required. The as-synthesized nanowires include unreacted ingredients and nanoparticles, and such impurities are inevitable[56]. Obtaining a pure Ag NW solution improves the optoelectronic properties of the as-deposited Ag NW network. The main means of purification include centrifugation[57], precipitation[58], membrane filtration[59], and cross-flow filtration[60].

Following purification, Ag NWs are deposited onto the desired substrates in the form of conductive networks. Various deposition techniques are reported in the literature, such as drop casting, spin coating, bar coating, and spray coating. The methods were viable depending on the device's aim and the substrates' shape and size, each with their pros and cons. In drop casting, drops of Ag NW solution are deposited onto the substrates, and the solvent is evaporated. The uniformity and thickness of such networks cannot be controlled well, and the process is highly prone to coffee ring occurrence[61]. Spin coating is a low-cost and facile method that uses centrifugal force to spread the solution and evaporate the solvent. It is a good choice for small-sized flat substrates. Still, the technique is not applicable outside the lab scale, a substantial amount of material is wasted[62] and the nanowires in the network are prone to have a oriented radially. Mayer rod coating utilizes an automated bar system moving over a substrate with controlled speed. It is simple and roll-to-roll applicable[63]. The solution is dropped onto the substrate, and deposition occurs as the bar sweeps over. The solvent is evaporated later by placing the substrate in an oven. However, using dynamic heating during the coating process Zhang et al.[64] yielded superior results compared to static drying. Using spray coating, the Ag NW solution is deposited onto the substrates through a nozzle with compressed gas. The substrates are mounted on a heated surface so incident droplets can dry immediately. Spraying pressure can be adjusted to achieve better coating homogeneity on the substrate[65]. Hence, a large-scale applicable deposition of Ag NWs can be achieved, ensuring a highly uniform distribution.

1.6.4 Performance Evaluation of Silver Nanowire Networks

1.6.4.1 Optical Transmittance and Haze

The obtained networks are best characterized by three essential parameters: optical transmittance, haze, and sheet resistance. Optical transmittance is the ratio of the light transmitted by the material to the incident light. UV-Vis spectrophotometers are used to measure optical transmittance. It is often designated in a percentage value (%T), and the benchmark for a TCE is having an optical transmittance above 90% at a wavelength of 550 nm.

Haze (%H) is an optical property associated with the TCE’s visual blurriness. Incident light scatters upon meeting various obstacles, causing a hazy TCE. Regarding Ag NW networks, haze could stem from dirt from the substrate, silver nano or microparticles, dense Ag NW networks, and thick nanowires[66]. While calculating haze, the network's diffuse transmittance (T_D) is measured. The ratio of diffuse transmittance to total transmittance yields haze[67]. The haze of a TCE must be as low as possible, and values below 3% are considered to be acceptable[68].

1.6.4.2 Sheet Resistance

Sheet resistance (R_{sh}) is the two-dimensional resistance of the material. TCEs are considered as thin films; therefore, the sheet resistance is a better means of expressing electrical resistance. The electrical resistance R is related to the resistivity (ρ), the length (L), and the cross-sectional area ($W.t$) of the material, given in Eq 1.1.

$$R = \rho \frac{L}{W.t} \qquad \text{Eq 1.1}$$

where, W is the width, and t is the thickness where current passes through the material. Combining resistivity with thickness, Eq 1.2 can be reached.

$$R = \frac{\rho}{t}\frac{L}{W} = R_{sh}\frac{L}{W} \qquad \text{Eq 1.2}$$

The thickness of thin films is often challenging to measure. Thus, the sheet resistance is defined as the resistance per square area of the film. Its units are Ω/sq. A TCE with a sheet resistance below 20 Ω/sq is considered to have a low sheet resistance[69].

1.6.4.3 Optical Figure of Merit

In combining T with R_{sh}, it is possible to devise an optoelectronic figure-of-merit (FoM). One such FoMs for thin films was introduced by Haacke[70] in 1976, given in Eq 1.3.

$$FoM = \frac{T^{10}}{R_{sh}} \qquad \text{Eq 1.3}$$

Another FoM[71] for TCEs was introduced as the electrical conductivity (σ_{DC}) to optical conductivity (σ_{OP}) ratio, given in Eq 1.4.

$$\frac{\sigma_{DC}}{\sigma_{OP}} = \left(\frac{188.5}{R_{sh} \times (T^{-0.5} - 1)}\right) \qquad \text{Eq 1.4}$$

Then, a commercially available ITO film with an optical transmittance of 85% and a sheet resistance of 10 Ω/sq (Sigma-Aldrich, CAS No: 50926-11-9) has an FoM (σ_{DC}/σ_{OP}) of around 223, which can be defined as a baseline value. With the introduction of these FoMs, it is clear that there is a trade-off between optical transmittance and electrical conductivity. Increasing the deposited Ag NW amount will increase the electrical conductivity at the expense of optical transmittance. Figure 1.6 shows the target performance of TCEs, reaching an optical transmittance as close to 100% as possible while maintaining a low sheet resistance.

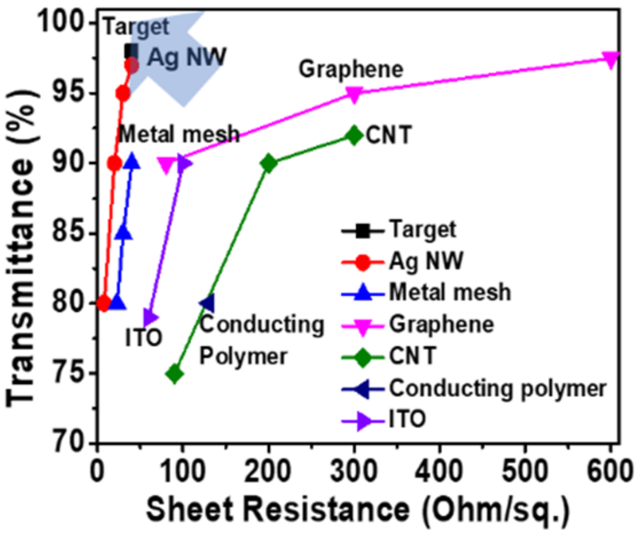

Figure 1.6 Optoelectronic properties of common TCE materials[72].

The percolation theory of nanowires dictates that the shorter the nanowire, the more the contact points. Having more contact points lead to increasing junction resistance. Junction resistance arises from the PVP used as a capping agent during the synthesis. As mentioned, PVP molecules encapsulate the Ag NWs and facilitate one-dimensional growth. Even though purification steps eliminate some residual PVP on the nanowire surface, a few nanometers thick PVP layer still persists. Therefore, electron transfer between two nanowires must occur through a metal-polymer-polymer-metal interface. Ag NWs are defect-free structures with very high conductivity, allowing electrons to move freely with practically no resistance. The junction resistance, however, is substantial compared to individual nanowires[73]. To eliminate this problem, researchers have made great efforts to reduce the junction resistance while trying to keep the optical transmittance as high as possible.

1.6.5 Post-Treatments on Silver Nanowire Networks

Post-treatments on Ag NW networks have been an intriguing topic since the fabrication of the first Ag NW TCEs. Making the most out of the produced Ag NW networks has been a focal point of study. Since the synthesized nanowires have a certain aspect ratio, the optoelectronic properties are limited to an extent. Researchers tried to tackle the junction resistance problem to improve the optoelectronic properties of Ag NW networks. Different approaches to the prospect of increasing the optical FoM of TCEs have been used in the past. These efforts can be divided into three main segments: thermal welding, chemical methods, and cold welding.

1.6.5.1 Thermal Welding

For thermal welding, the main aim was to use localized heat or overall applied heating to fuse the junctions together. The optical transmittance was generally not significantly altered by these methods since no other material was deposited onto the TCEs. The processes differed by the applied heat source. Such methods included heat treatment[74,75], laser welding[76,77], welding by Joule heating[78,79], and plasmonic welding[80,81].

Langley et al.[74] have thoroughly investigated the heat treatment of Ag NWs. In their work, the annealing of Ag NW networks at temperatures between 200-320°C was studied. SEM images from Ag NWs subjected to different annealing temperatures are provided in Figure 1.6. The temperature was ramped up gradually (15°C/min) and the phenomena occurring during heat treatment were explained. The degradation of organics and PVP, local sintering, and Rayleigh instability were detected as the primary mechanisms involved. At lower temperatures (30 - 140°C), organics adhered to the substrate were found to desorb and leave the surface. At 150°C, the glass transition temperature (T_g) of PVP, Ag NWs were found to move closer due to flowing PVP. PVP started to undergo degradation at higher temperatures (150-250°C). This can be visualized in Figures 1.7 (b) and (c). Rayleigh instability was the fragmentation and spheroidization of Ag NWs upon being subjected to high temperatures. The Ag NW network was broken, with nanowires losing their morphology, turning into small, disconnected silver islands as shown in Figure 1.7 (d). The temperature at which Rayleigh instability occurs depends on the thickness of the nanowires. Thicker nanowires withstand higher annealing temperatures. Furthermore, the Ag NW network's sheet resistance dropped from 10^7 Ω/sq to 9.5 Ω/sq by heat treatment at 200°C for 2 hours. An optical transmittance of 90% was maintained at a wavelength of 550 nm.

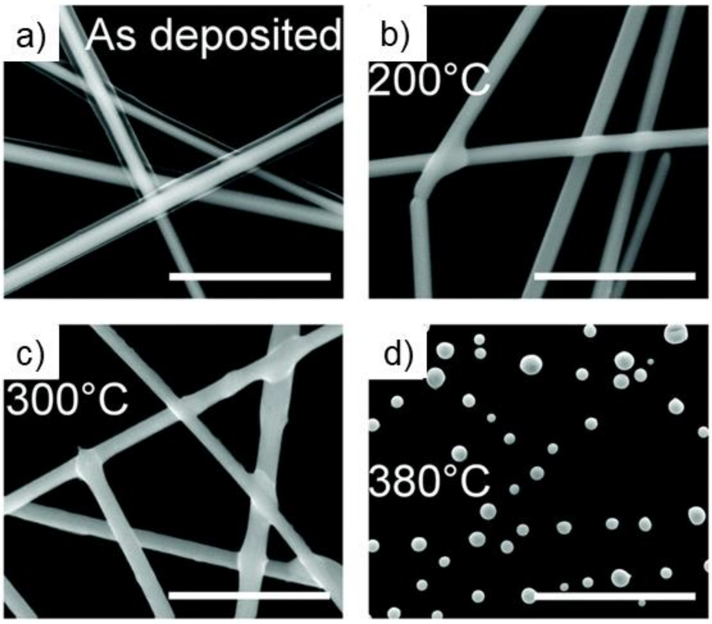

Figure 1.7 SEM images of a) pristine Ag NWs and heat treated Ag NWs at b) 200, c) 300, and d) 380 °C [74].

Liang et al.[76] used a spatial-light-modulated femtosecond laser to sinter the nanowire junctions. PET substrates were spin-coated with Ag NWs and irradiated with the femtosecond laser. The Gaussian laser beam was modulated into 773 μm lines, amplifying welding efficiency compared to the traditional spherical lens-focused lasers. Only the junctions were found to be affected by the laser due to the local electric field enhancement occurring in those areas. This proved laser welding is a self-limited process as well. Tape testing results also demonstrated that the Ag NW became embedded in the PET substrate due to high local temperatures at the junctions. The welded Ag NW TCE exhibited a sheet resistance of 14.7 Ω/sq and an optical transmittance of 89.5%. Consequently, it was deemed suitable for use as a transparent thin film heater.

Joule heating allows conductors to be heated when a current is passed through. Joule’s law gives the power of heat generated by a particular device in Eq 1.5.

$$P = I^2 R \qquad \text{Eq 1.5}$$

Song et al[78]. used the Joule heating principle to locally increase the Ag NW junction temperatures in an attempt to weld them. Ag NWs were spin-coated, and two metal contacts were evaporated on two opposing sides of the substrate. As the current was passed through the TCE, due to the presence of PVP at the junctions, enough power was generated to facilitate fusion. The mechanism for this was explained as electromigration occurring at high current density areas. In their experiments, electrodes were subjected to a current treatment at 0.2 A, limited to 25 V compliance voltage, for 30 seconds. Figure 1.8 (a) shows a schematic of the experiment setup. The SEM image of the pristine Ag NW network is given in Figure 1.8 (b). The different morphologies observed in Figures 1.8 (c), (d) and (e) show that one nanowire deformed towards the other, proving the electromigration of Ag atoms. This morphology is not typically observed in heat-treated or plasmonic welded Ag NW networks. After the treatment, the TCE was found to have a sheet resistance of 19.7 Ω/sq and an optical transmittance of 86.7%.

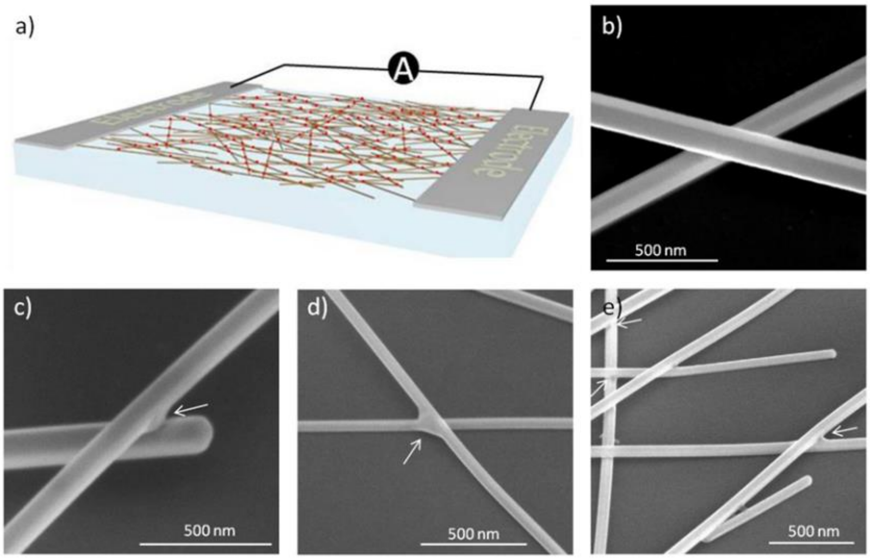

Figure 1.8 Schematic Joule heating setup. SEM images of the Ag NWs in b) pristine and (c, d, e) electro welded condition having different morphologies. Arrows show the electromigration between Ag NWs[78].

Plasmonic welding of Ag NW networks has been demonstrated by Park et al. [81] , where a xenon flash lamp was used to perform local welding of the nanowires. Figure 1.9 schematically shows the experimental setup and welding mechanism. A photothermal reaction arose from localized heat energy supplied by the flash lamp. A xenon flash lamp with a pulse duration of 660 μs was used. The resultant TCEs had a sheet resistance of around 5 Ω/sq with an optical transmittance of 90%. A simulation of the treatment setup was developed using 3D finite-difference time-domain (FDTD) analysis. It was found that the spectral peaks in the near-infrared region (NIR) could locally melt and embed the nanowires into the polyethylene terephthalate (PET) substrate, enhancing the adhesion of Ag NWs. The peaks in the ultraviolet (UV) and NIR frequencies provided intense effective heat generation in the confined areas between Ag NWs. The electromagnetic waves were focused by gap plasmons to these areas within the diffraction limit, creating hot spots for the welding of the nanowires. Once the junctions were welded together, the electromagnetic field between the nanowires dissipated, providing the self-limiting aspect of this welding method. Therefore, multiple runs of flash irradiation did not harm the nanowires, keeping the one-dimensional morphology.

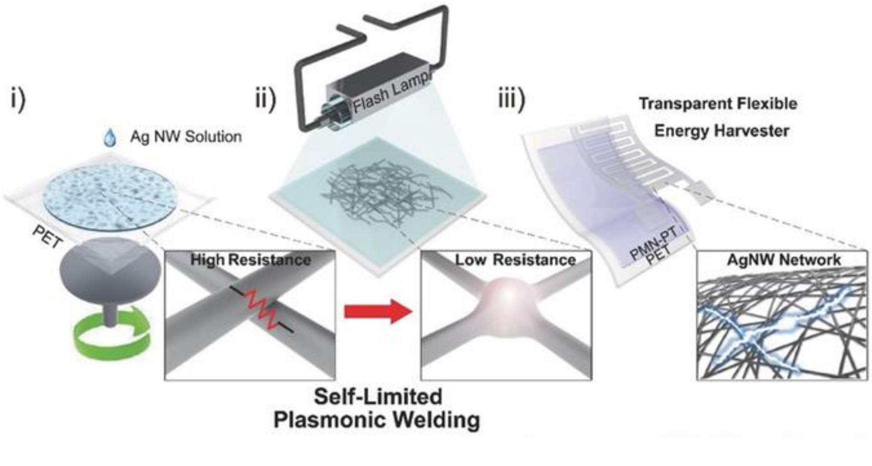

Figure 1.9 Schematic showing i) Ag NW TCE production; ii) xenon lamp plasmonic welding; iii) flexible transparent device production[81].

1.6.5.2 Chemical Methods in Post-Treatments

Throughout the years, many different chemical approaches have been suggested for welding nanowires. Generally, most of these methods involve Ag^+ ion deposition to selectively fuse the junction regions. This process often involves various reducing agents and other additives. Some other chemical methods used the preexisting nanowires as the Ag source and applied redox reactions. The Ag from the nanowires were dissolved and redeposited onto the surface to fuse the network. A completely different approach involved the removal of PVP molecules around the Ag NWs in reducing junction resistance. As a result, a metal-metal contact interface is maintained, facilitating efficient electron transfer.

Kang et al.[82] engineered a roll-to-roll Ag NW TCE production and chemical treatment method. In this work, Ag NWs were deposited onto PET substrates via Mayer rod coating, and Ag electroplating was used to cover the nanowires using the galvanostatic mode. An electroplating bath was prepared with $AgNO_3$ providing the solvated Ag. Sodium hyposulfide ($Na_2S_2O_3$) and potassium metabisulfude ($K_2S_2O_3$) were used as conductivity enhancers and stabilizers, ammonium acetate ($CH_3COOHNH_4$) was added as a pH buffer, and aminothiourea (CH_3N_3S) acted as the substrate protector. The Ag NW network was used as the cathode, and an Ag plate was used as the anode during electroplating. The process was regulated with the current density and electroplating time, allowing the control of sheet resistance and optical transmittance. Figure 1.10 (a) shows the coating setup of the roll-to-roll device. It was found that an Ag shell grew epitaxially on the Ag NWs. As the electroplating time increased, it was observed that the nanowires grew thicker, and the junctions became fused, as can be seen in Figure 1.10 (b). The time required to achieve a low sheet resistance was shorter in higher current density depositions. The Ag-coated Ag NW networks displayed a sheet resistance and optical transmittance (at 550 nm) of 19 Ω/sq and 90%, respectively.

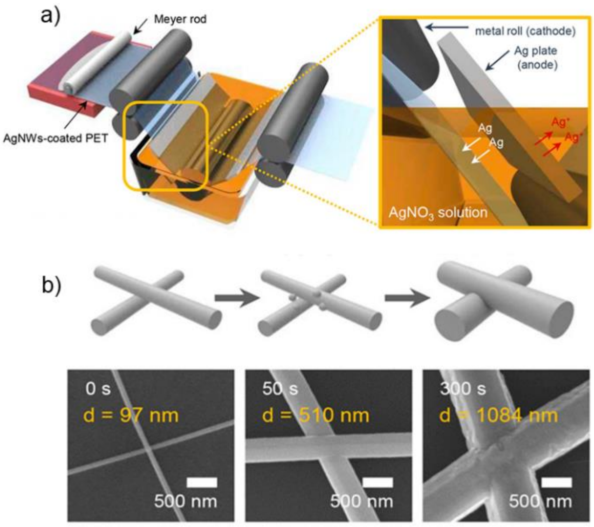

Figure 1.10 a) The roll-to-roll chemical treatment setup for Ag NW networks; b) Ag NW junction morphology with increasing treatment time[82].

In an attempt of welding Ag NW networks without external Ag ion addition, Kang et al[83]. explored the effect of aqueous halide salts on the nanowires. The TCEs were prepared by spray coating the nanowires onto polyethylene naphtalate (PEN) substrates. Four sodium halide salts, namely: sodium fluoride (NaF), sodium chloride (NaCl), sodium bromide (NaBr), and sodium iodide (NaI) were dissolved in deionized water. The molarity of the solutions was fixed at 0.5 M, and the TCEs were dipped into the solutions for 10 - 60 seconds. The films were washed with deionized water to remove any residual solution. It was proposed that, in the presence of dissolved oxygen, Ag atoms from the Ag NWs' surface dissolve into the solution. The halide ions act as catalysts for Ag ions to redeposit onto the surface and junctions. The welding, specifically at junctions, was explained by the electrostatic potential near the junctions being higher than the surfaces. NaI and NaBr salts provided a lower amount of reduction after 60 seconds of treatment, whereas NaCl and NaF were more potent. Figure 1.11 shows the required treatment time for each halide salt and the effectiveness of NaF compared to NaBr. SEM images show the clear fusion of nanowire junctions. NaF even required a treatment time of 20 seconds to reach the minimum level. The high solubility product constant of AgF in water, formed by NaF, improves the autocatalytic reaction by increasing the amount of readily available F ions. The halide welded TCE displayed a sheet resistance and optical transmittance of 9.3 Ω/sq and 92%, respectively.

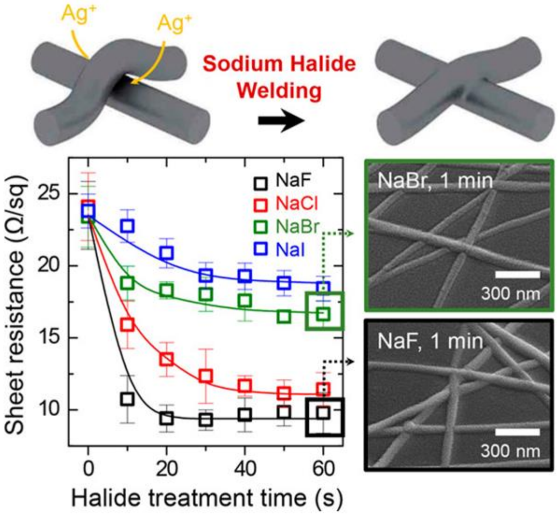

Figure 1.11 Reduction in sheet resistance and consequent changes in Ag NW morphology as a result of halide welding[83].

In their work, Ge et al.[84] cleaned the PVP layers covering the Ag NWs by means of electrochemical desorption. Ag NWs were deposited onto PET substrates via spin-coating and placed as the working electrode in a three-electrode setup. The network was polarized at -0.85 V in an N_2-saturated $NaClO_4$ solution for 15 seconds, followed by gentle rinsing and blow drying. Electrochemically polarizing the Ag NW network in the hydrogen evolution reaction region allowed H ions to adsorb onto the nanowires' surface. The strength of the Ag-H bond overpowered that of the Ag-O bond and displaced the PVP molecule adsorbed to the Ag NWs. Afterwards, the H atoms combined and bubbled out as H_2 gas, completing the reaction. The result was a completely clean Ag NW network. Another piece of evidence for this was given in the form of cyclic voltammetry (CV) studies, where the current density increased as more cycles were applied up to a certain point where it reached a plateau. Meanwhile, the electrochemically active areas increase, and the overpotential for hydrogen evolution reaction decreases, proving that the process cleans Ag NWs' surface. Eventually, a sheet resistance and optical transmittance of 13 Ω/sq and 90.91% were achieved in the TCE, respectively.

1.6.5.3 Cold Welding Methods

Cold welding methods were carried out at room temperature and performed using high pressure to weld Ag NWs. Mechanical appliances such as hydraulic machines or isostatic pressure pumps have been used to exert pressure on the nanowires. Capillary forces have also been applied to weld the nanowires. The benefit of the cold welding method lies in avoiding the need for high annealing temperatures or the use of chemicals that could potentially damage certain substrates.

Tseng et al.[85] have developed a pressure welding method that does not damage the glass substrate and allowed a clean transfer of Ag NWs to a transparent polymethyl methacrylate (PMMA) substrate. Initially, they spin-coated the Ag NWs and 1 μm thick PMMA on separate glass substrates. Then, the substrates were placed between the metal sheets of a hydraulic press. A pressure of 200 kg/cm^2 was applied, and the Ag NW network was transferred from glass to PMMA. The transfer process can be visualized in Figure 1.12 (a)[85]. The exerted pressure caused PMMA to deform elastically, and Ag NWs were embedded into the new substrate. Therefore, the surface roughness of the TCE could be reduced significantly, which is advantageous for applications such as OLEDs. The morphological changes between pristine, direct-glass-pressed, and PMMA-mediated Ag NW networks can be seen in Figures 1.12 (b, c, and d). It is clear that adding the PMMA buffer layer improved the welding compared to the directly-pressed networks. In the PMMA-mediated case, the surface roughness decreased from 76.1 nm to 12.6 nm. The obtained TCE had an optical transmittance and sheet resistance of 93% and 34.3 Ω/sq, respectively, with a 2.58% haze.

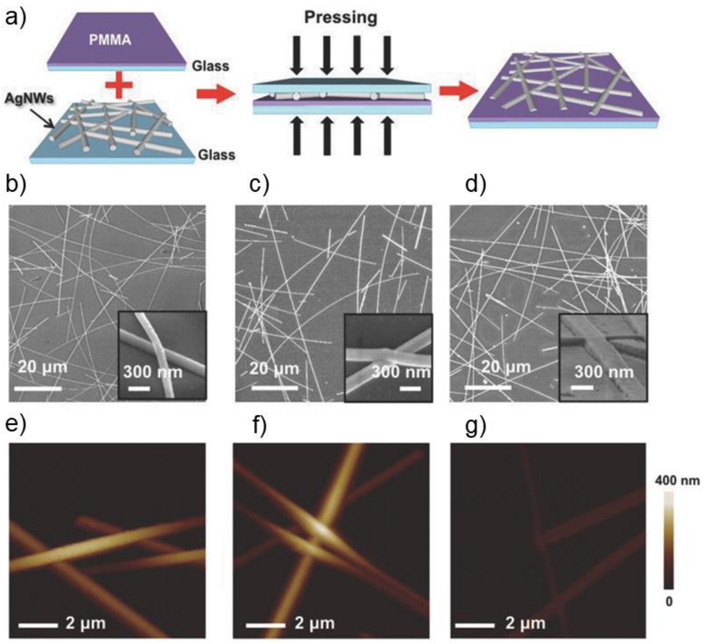

Figure 1.12 a) Schematic drawing of the pressure welding; SEM images of the Ag NWs in b) pristine, c) direct-glass-pressed, and d) PMMA-mediated pressure welded form. Insets show magnified images of the junctions[85].

Using capillary forces is a self-limited and facile method of welding nanowires. Liu et al. have drastically improved the optoelectronic performance of Ag NW networks by applying moisture. The controlled application of water vapor through a water mist humidifier with a 30 cm/s flow rate at a distance of about 5 cm for 3 seconds was enough to facilitate welding. It has been reported that warm exhalation for about the same amount of time also works. The water droplets condensed around the gaps at the nanowire junctions formed during the deposition. Once the droplets started to dry out assisted by gentle fanning, a meniscus formed the liquid bridge, as seen in Figure 1.13 (b)[86]. The capillary forces between the nanowires could reach 10 nN, corresponding to GPa level pressures initially, dropping down to MPa levels as nanowires are joined together. The exerted force is enough to weld the Ag NWs in a self-limited manner. Sheet resistance of the TCE was found to decrease from 2.24 x 10^5 Ω/sq to 179 Ω/sq with this facile treatment at an optical transmittance of 89.4%.

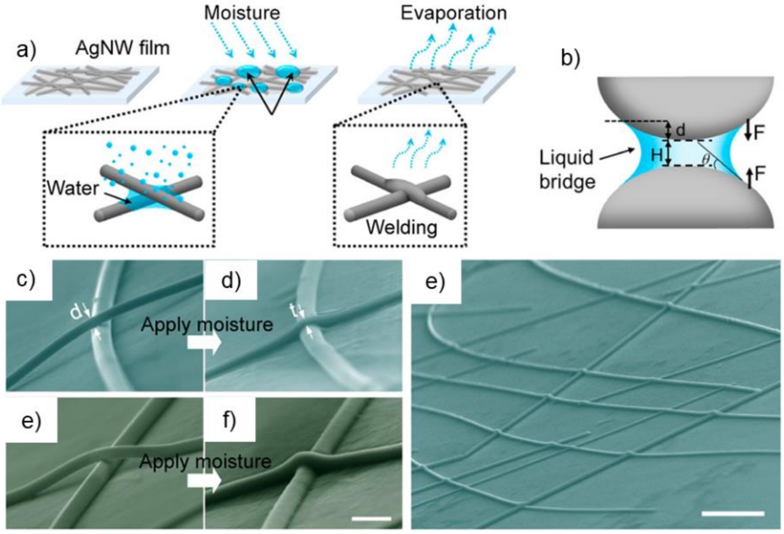

Figure 1.13 a) The schematic drawing of the capillary welding mechanism; b) the meniscus formed between two Ag NWs; tilted-angle SEM images of Ag NWs before and after moisture welding c, d) showing a significantly thinner top nanowire; e, f) showing two nanowires of similar size being welded; e) multiple welded junctions[86].

1.6.6 Motivation for This Thesis

Throughout the years, Ag NWs have been synthesized in various ways, leading to diverse outcomes. The focus of research has been to develop a recipe for high-yield syntheses with Ag NWs exhibiting a large aspect ratio. While having longer and thinner nanowires is important, extremely large aspect ratio nanowires bring deposition problems. To fix these, post-treatments on Ag NW networks have been studied extensively. Many different approaches were tried, and promising results were published. However, in all the studies conducted, Ag NWs used from different vendors and synthesis approaches have different lengths, diameters, PVP thicknesses, and molecular weights, as well as different deposition methods, which may affect the post-treatment response. The efficacy of any given post-treatment method on a Ag NW network is unknown. This study investigates the efficacy of various post-treatment methods derived from different studies on the same Ag NW batch. This approach removes the variability of the factors mentioned above. Post-treatments developed in-house are also considered. The most effective post-treatment methods are combined to create the optimal method of improving the optoelectronic performance of Ag NW networks. Chapter 2 displays the results from all the post-treatments applied, with different means, and provides an optimized Ag NW network for further chapters.

Chapters 3 and 4 exemplify two applications for the optimized Ag NW networks. In Chapter 3, the optimized Ag NW network is utilized as a current collector in a transparent triboelectric nanogenerator (TENG). This transparent TENG utilizes the liquid-solid interface electrification to provide a device which is pH and solution concentration sensitive, and is used as a switch to power-up an Ag NW-based thin film heater. In Chapter 4, the TCEs are utilized in electrochromic devices. Tungsten trioxide (WO_3) and non-stochiometric tungsten oxide (WO_x) are deposited onto the Ag NW network as the electrochromic layer, with nickel oxide (NiO) acting as the counter electrode. The coloration efficiency and stability of the electrochromic devices are investigated in detail and reported.

CHAPTER 2

POST-TREATMENTS ON SILVER NANOWIRE NETWORKS

2.1 Experimental Details

2.1.1 Synthesis of Silver Nanowires

All chemicals were purchased from Sigma Aldrich and were used without further purification. The synthesis glassware was washed with anionic detergent (Alconox) and air-dried. Then, the glassware was ultrasonically cleaned with acetone (99.8%), ethanol (99.8%), and deionized water (18.3 MΩ). In a typical synthesis, 80 ml of ethylene glycol (EG) was measured using pipettes and placed in a beaker along with 1.77 g polyvinyl pyrrolidone (PVP) (monomer-based calculation MW=55,000) and 5 mg sodium chloride (NaCl). The solution was stirred at 80°C and 1000 rpm until the PVP was completely dissolved. The solution was then left to cool down to room temperature. In a round bottom flask, 40 ml EG was added with 680 mg silver nitrate ($AgNO_3$). The solution was stirred at room temperature in a dark environment until fully dissolved. The flask was then moved into a silicone oil bath heated to 120°C. The EG/PVP/NaCl solution was quickly added into the EG/$AgNO_3$ solution, and the temperature was immediately increased to 160°C, stirred at 1000 rpm. After 90 minutes, the reaction was complete, and the flask was removed from the silicone oil. The solution was left to cool down to room temperature and transferred to a beaker for storage.

2.1.2 Purification of Silver Nanowires

The synthesized Ag NWs were stored for at least three days before purification to allow the settlement of nanowires to the bottom of the beaker. Carefully, the top of the solution was decanted into another beaker without disturbing the contents lying underneath. The settled nanowires were agitated and diluted using acetone. Then, once the nanowires sank to the bottom of the beaker, the supernatant acetone and unreacted ingredients and nanoparticles were discarded. The Ag NWs were diluted with acetone again and centrifuged twice at 7000 rpm for 10 minutes before being washed with ethanol and centrifuged twice at 7000 rpm for 20 minutes. Ultimately, Ag NWs were dispersed in ethanol and stored in a cool, dark environment for further use.

2.1.3 Preparation and Post-Treatment of Silver Nanowire Networks

Ag NWs in ethanol were diluted to a concentration of 0.5 mg/ml before deposition. All soda-lime-silica glass substrates were cut into 1 x 1 inch squares. Then, ultrasonically cleaned with acetone, ethanol, and deionized water for at least 10 minutes each. The glasses were then dried with N_2 gas to eliminate any residual stains. The Ag NWs were deposited onto the glass substrates by spray coating. All cleaned glassware were mounted on a hot plate set at 120°C for instant evaporation of ethanol. The N_2 feed gas pressure and coating distance were was set to 2 atm and 10 cm, respectively. The deposition of Ag NWs continued until the target resistance was attained. The electrical resistance was monitored through control samples with silver paste contacts on opposite sides using a digital multimeter (Tenma 72-7730).

Many different post-treatment methods were tested in this work: heat treatment, electroless welding, ascorbic acid-assisted soldering, sodium borohydride ($NaBH_4$) cleaning, nitric acid (HNO_3) assisted Ag welding, halide welding, hot water treatment, and capillary welding. A combination of the most promising methods was also applied to find the optimally treated Ag NW network. The ambient stability of the optimized networks was also measured weekly. The sheet resistance of the Ag NW networks was measured after each treatment cycle. The optical transmittance of the samples was analyzed before and after the treatments. The scanning electron microscopy (SEM) images were taken after the treatment was concluded.

Heat treatment experiments were conducted by inserting the Ag NW networks into a furnace set at temperatures 180, 200, 220, 240, 260, and 280°C. The sheet resistance of the samples was taken in 15-minute intervals, and their optical transmittances were measured before and after the entire treatment.

Electroless welding is the work proposed by Xiang et al.[87], and the treatment was used without any modification. Briefly, 10 ml $AgNO_3$ (0.2%) solution is mixed with 1 ml sodium hydroxide (NaOH) and 6 ml aqueous ammonia (0.2%). Then, a 0.5% glucose solution was prepared and mixed 1:1 with the silver-ammonia solution. The Ag NW network was immersed in the solution for 2 minutes and rinsed with deionized water. Finally, the TCE was left in a vacuum oven at 60°C for 1 hour. This treatment was applied for multiple cycles, and after each cycle, sheet resistance was measured, and optical transmittance spectra were taken before and after the treatment.

Ascorbic acid-assisted soldering (AA solder) was adapted from Lu et al.[88], where an aqueous $AgNO_3$ solution (1.5 mM) was prepared, and the HNO_3 was added to set the pH precisely at 3. Then, 1 mM ascorbic acid was added to the mixture. The resultant solution was spin-coated or drop-casted onto the Ag NW networks before being dried with N_2 gas. After each treatment cycle, sheet resistance and optical transmittance measurements were taken from the samples.

$NaBH_4$ treatment was adapted from prior works in the literature[89,90]. 12.5 ml each of deionized water and ethanol was placed in a beaker, and $NaBH_4$ was added in various molarities. 0.1, 0.25, 0.5, 1, and 2 M solutions were prepared, and the TCE was immersed into the solution for 15 seconds each cycle, followed by rinsing in deionized water and ethanol for 15 seconds each. The TCE was finally dried by gentle N_2 blowing.

The HNO_3-assisted welding (HNO_3-Ag) method is a post-treatment developed in-house. Briefly, 0.01 g $AgNO_3$ was dissolved in 25 ml deionized water. Then, 1.25 ml HNO_3 was added. The Ag NW networks were immersed in the solution for 30 seconds and oven-dried at 100 °C for 1 hour.

Halide welding[83] and its mechanism are explained in Chapter 1. The applied treatment consisted of NaF aqueous solutions with different molarities. 0.5, 1, and 5 M solutions were investigated. The immersion times were 30 seconds per cycle. The samples were gently rinsed in deionized water and ethanol.

Hot water treatment is an in-house developed method where the water temperature was set at 90 °C. Ag NW networks were immersed in hot water for 30 seconds each cycle before being rinsed with ethanol to prevent watermarks from forming on the TCE surface.

Finally, the $NaBH_4$ treatment and HNO_3-assisted welding methods were performed sequentially to produce the most effective post-treatment method. The stability of this network was monitored for a period of 2 months.

2.2 Characterization Methods

2.2.1 Scanning Electron Microscopy (SEM)

The SEM images of the post-treated Ag NW networks were obtained to analyze the effectiveness of each post-treatment method. FEI NOVA NANO SEM 430 was used at an operating voltage of 15 kV. Samples on glass and Si wafers were used for SEM analyses. A very thin layer of gold coating on the glass samples was applied to ensure conductivity through the sample. The morphologies of Ag NWs and, specifically, junction areas were considered. It was possible to see the difference between welded and pristine junctions clearly. Deposited Ag also affected the morphology.

2.2.2 Sheet Resistance Measurements

The sheet resistance measurements were taken by a Signatone Pro4 4-point probe station using a Keithley 2400 source meter. Sheet resistances of pristine and post-treated Ag NW networks were taken after each treatment cycle. Samples deposited on glass substrates were used for the measurements. Stability tests were also conducted.

2.2.3 Optical Transmittance Measurements

The optical transmittance measurements were carried out using Shimadzu 3600 UV-Vis-NIR spectrophotometer equipped with an integrated sphere. Total and diffuse optical transmittances of samples were measured, which allowed haze calculations to be made. A wavelength interval of 300 - 800 nm was considered during the measurements. The optical transmittance values used to calculate FoM and haze were obtained at a wavelength of 550 nm.

2.2.4 Surface Enhanced Raman Spectroscopy (SERS) Measurements

SERS measurements give powerful information about the PVP layers surrounding Ag NWs. The measurements were provided by the setup in Nano Optics Laboratory, Department of Physics, METU. The sample was irradiated by the light source of the integrated camera in the Raman head. A 532 nm wavelength light was used with a frequency-doubled DPSS Nd-YAG SLM laser (Laser Quantum torus). The power of measurements was set at 0.32 W. A f/6.4 550 mm Raman spectrometer (Horiba Jobin-Yvon iHR550) with a 1024x256 pixel CCD (Horiba Synapse) was used to collect the data for further analysis.

2.2.5 X-Ray Photoelectron Spectroscopy Measurements

The XPS analysis was carried out using PHI 5000 Versa Probe Spectrometer. CasaXPS was used for XPS fitting and analysis of the peaks, and a Gaussian-Lorentzian function was used in the fitting process. C 1s charge correction was made at 284.8 eV. XPS was used to analyze the removal of PVP surrounding Ag NWs following the most promising post-treatment method.

2.3 Results and Discussion

2.3.1 Silver Nanowire Networks

Figure 2.1 (a) schematically shows the deposition of Ag NWs networks. A photograph of the obtained Ag NW networks is provided in Figure 2.1 (b). The SEM image in Figure 2.1 (c) displays the clean and purified Ag NW network, proving a high-yield synthesis. In this work, each sample was sprayed to a sheet resistance of about 50 Ω/sq and had an optical transmittance of 90%. The total and diffuse spectral transmittance values are provided in Figure 2.1 (d), where a total transmittance and diffuse transmittance of 90.6% and 3.4% was achieved, respectively.

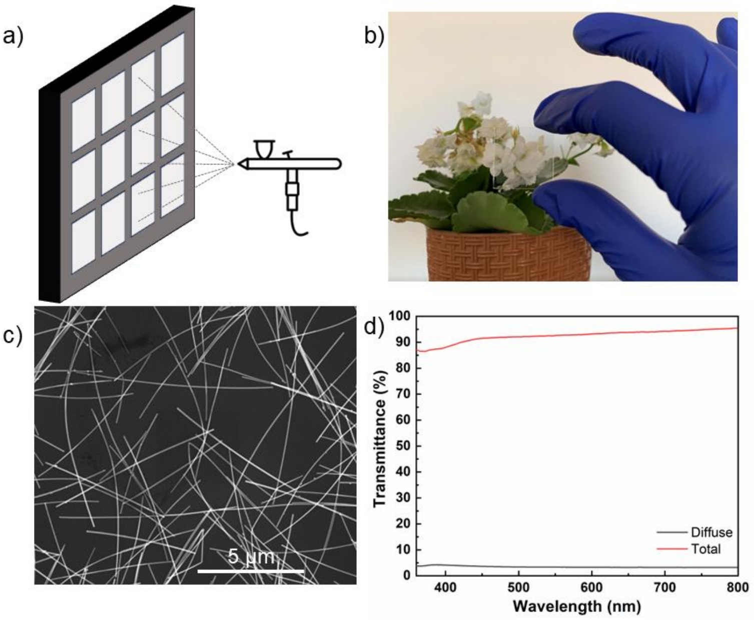

Figure 2.1 a) The schematic representation of spray coating of Ag NWs. b) Photograph of the resultant Ag NW network. c) SEM image from the sample. d) Optical transmittance spectra of the sample.

2.3.2 Effect of Heat Treatment

The Ag NW networks underwent heat treatment by subjecting them to various temperatures for different durations. Other works conducting heat treatment experiments have often controlled heating from room temperature to above 180 °C. This temperature was selected as the starting point according to results reported in the literature. In this work, the samples were directly placed into the preheated furnace and, after 15 minutes, were removed to cool down to room temperature. Sheet resistance measurements were taken between cycles to optimize the heat treatment temperature and duration. Optical transmittance measurements were taken from the optimized heat-treated sample. The treatment was halted after 8 cycles due to time concerns or when the electrode conductivity was lost.

Figures 2.2 (a), (b), and (c) display the characteristics of a Ag NW network heat treated at 180°C. The sheet resistance values did not change drastically throughout the treatment. The fusion of nanowires could not be seen after 2 hours of total treatment time, as seen in the SEM images provided in Figures 2.2 (b) and (c). The treatment was no longer continued.

Heat treatment performed at 200 °C also did not affect the Ag NW network after 8 treatment cycles. Figure 2.2 (d) shows the change in sheet resistance, which stagnated throughout the treatment. The SEM images in Figures 2.2 (e) and (f) also support this claim, as no morphological change was observed. The treatment temperature was increased further.

The optimized heat treatment temperature was reached at 220°C. Figure 2.2 (g) shows the change in sheet resistance values. After an initial decrease, through cycles 2 and 3, an increase was observed. Then, through cycle 8, a steady reduction in the sheet resistance and its standard deviation was observed, reaching 23 ± 4.2 Ω/sq. This behavior was first attributed to the welding of smaller nanowires, followed by their braking at 3rd cycle. Then, thicker nanowires started to fuse, forming a welded Ag NW network. Figure 2.2 (h) shows fused junctions in dashed red circles. More welded junctions can be seen in Figure 2.2 (i). The treatment time was optimized at 120 minutes for 220°C.

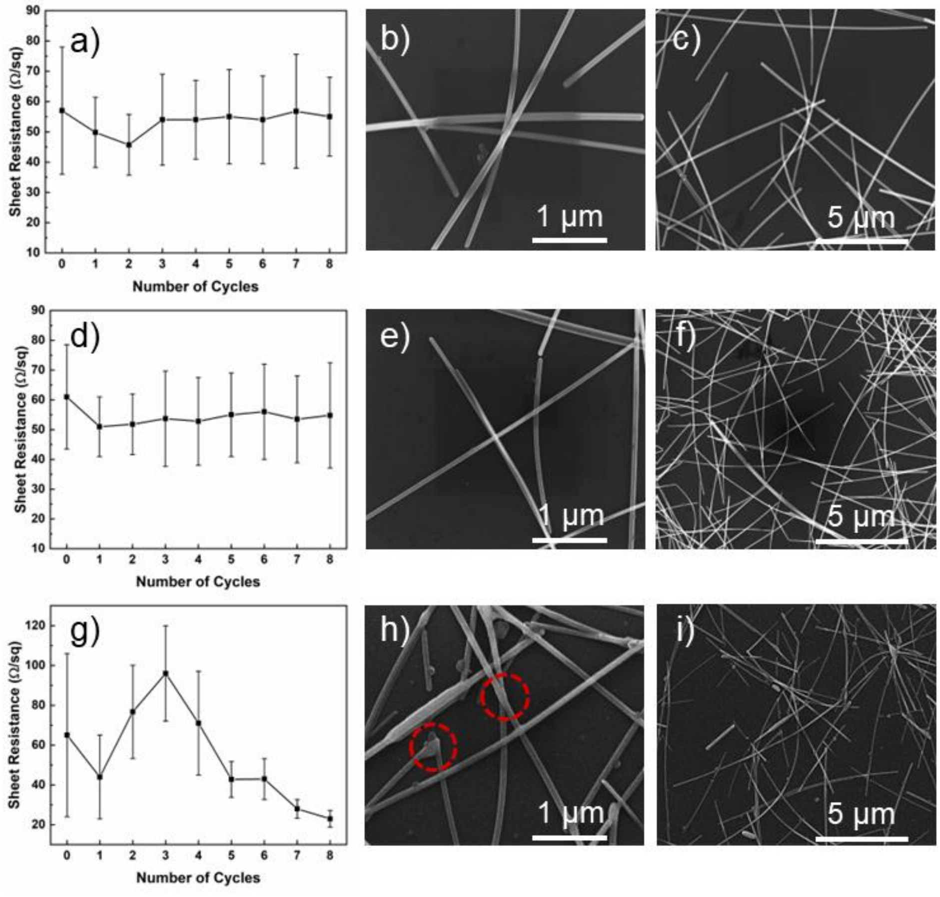

Figure 2.2 Changes in the sheet resistances and SEM images of samples annealed at (a-c) 180, (d-f) 200, and (g-i) 220 °C.

Figure 2.3 (a) shows the change in sheet resistance for heat treatment completed at 240 °C. A similar behavior was found when the thinner nanowires were damaged; an initial increase in the sheet resistance was observed. Again, the reduction in sheet resistance continued through cycle 6, after which the resistance started to increase. Welded junctions can be seen in Figures 2.5 (b) and (c). The reduction in sheet resistance was not as significant as in the treatment at 220 °C, only reaching as low as 35 Ω/sq. Therefore, this treatment was not continued.

Heat treatment at 260 °C had poor results. The sheet resistance values quickly rose to 130 MΩ/sq after the 3rd cycle, as shown in Figure 2.3 (d). Figures 2.3 (e) and (f) show many broken nanowires and small islands of Ag formed throughout the sample due to Rayleigh-Plateau instability. This treatment was discontinued.

Heat treatment at 280 °C had a similar result to that of 260 °C, where just after the 2nd cycle, the sheet resistance reached 50 MΩ/sq, as shown in Figure 2.3 (g). SEM images in Figures 2.3 (h) and (i) clearly show the disintegration of the entire Ag NW network. Remnants of thinner nanowires can also be seen.

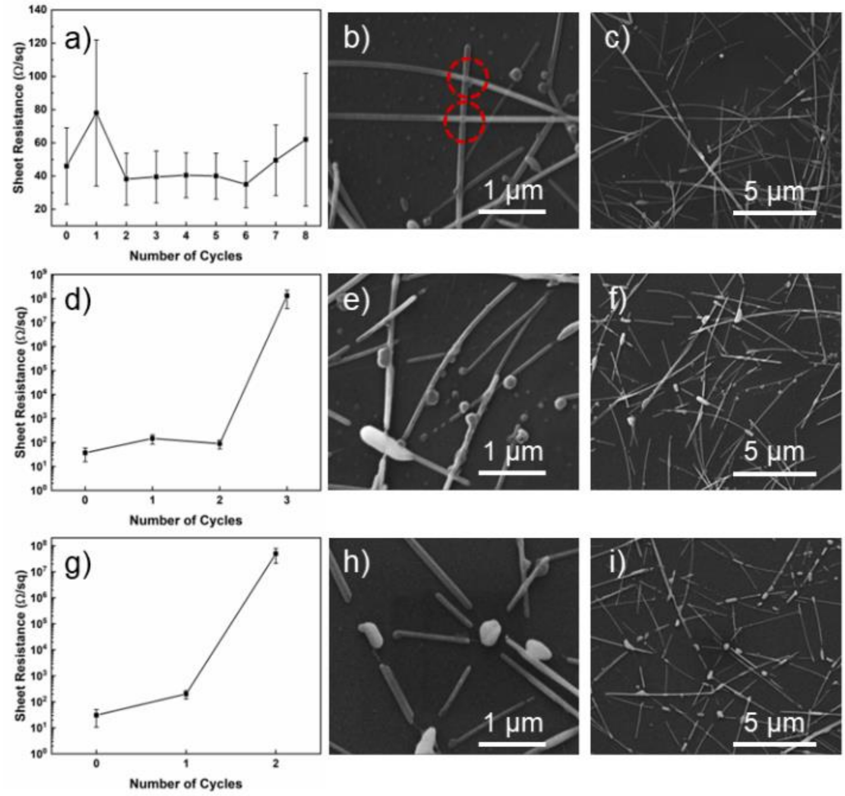

Figure 2.3 Changes in the sheet resistances and SEM images of samples heat treated at (a-c) 240, (d-f) 260, and (g-i) 280 °C.

According to the results, the optimum heat treatment was chosen as 220 °C for 8 cycles, giving a total of 120 minutes. The treatment’s effect on optical transmittance at 550 nm was also analyzed. A new sample was treated in the same manner, and optical transmittance measurements were taken at the end of each cycle. The results of the treatment are provided in Figure 2.4. The sheet resistance decreased to 24.1± 4.3 Ω/sq (Figure 2.4 (a)), and the change in both total and diffuse optical transmittance was negligible (Figures 2.4 (b)). Degree of deviation in sheet resistance got less with the increase in the number of cycles. The fusion of nanowires can also be seen in Figures 2.4 (c) and (d) in dashed red circles. The resultant FoM and haze were calculated at 152.83 and 3.6%, with starting values of 65.06 and 3.7%, respectively. There is a substantial increase in the FoM and a marginal decrease in haze, which was expected from this treatment.

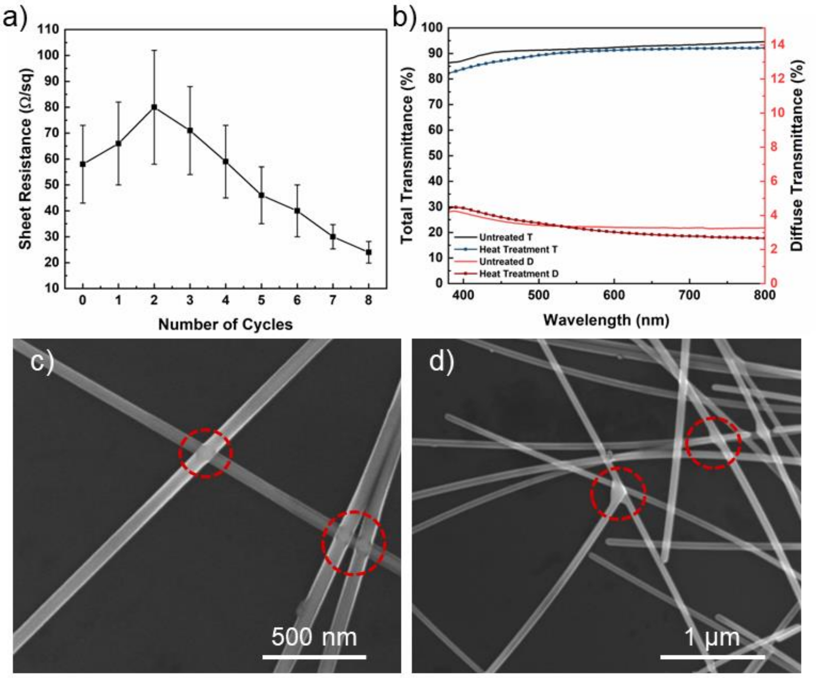

Figure 2.4 The optoelectronic characteristics of heat treated Ag NWs. a) Sheet resistance values and b) spectral optical transmittance. (c-d) SEM images from the treated sample.

2.3.3 Effect of Electroless Welding

The electroless welding treatment is a remedy for incomplete junction contact. The Ag ions contained in the solution remain adhered to the substrate even after rinsing.

Upon exposure to heat in a vacuum oven, these ions become strongly deposited onto the nanowires. The treatment was applied as given in the literature, and the results can be seen in Figure 2.5. The sheet resistance decreased drastically to 10.64 ± 1.24 Ω/sq (Figure 2.5 (a)). The optical transmittance measurement of the sample was taken in every treatment step, starting from 91% and going down to 85% by the end. In terms of the FoM, the end of the 2nd cycle was identified as the ideal point to conclude the treatment. The sample also had a homogeneous distribution of sheet resistance. The SEM images taken after the 2nd cycle are provided in Figures 2.5 (b) and (c), and at the end of the treatment are given in Figures 2.5 (d) and (e). After the 2nd cycle, nanowire junctions were fused well with a tiny amount of irregular Ag particles deposited around some junctions. After the 5th cycle, many nanoparticle formations occurred throughout the sample, which reduced the optical transmittance. The treatment was applied on a substrate with an FoM of 81.57 and a haze of 3.6%. After the 2nd treatment cycle, the FoM and haze was found to increase to 220.80 and 7%, respectively. While the resultant FoM was high, the increasing haze made this treatment sub-optimal. This treatment was discontinued.

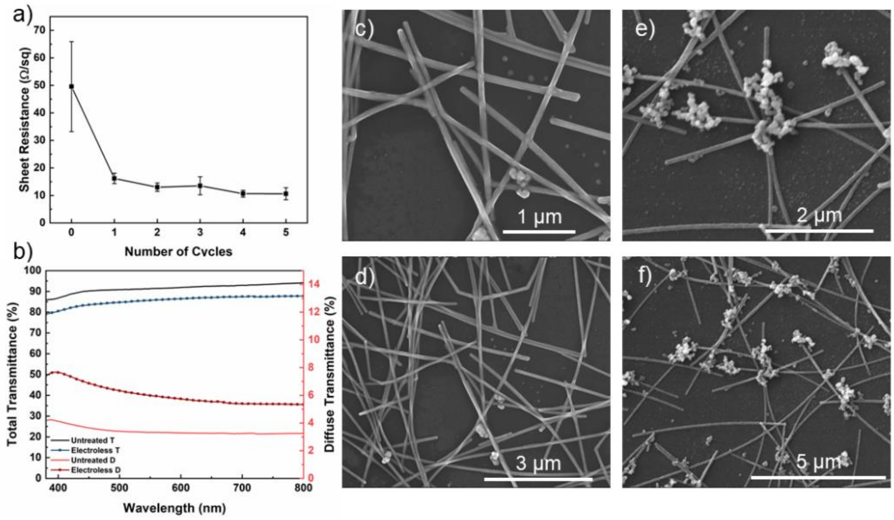

Figure 2.5 a) The sheet resistance and b) optical transmittance of the optimized electroless welding. SEM images after the 2nd treatment cycle c) and d). SEM images after the 5th treatment cycle e) and f).

2.3.4 Effect of AA Soldering

The ascorbic acid-assisted soldering method was implemented directly from the literature. Notably, ascorbic acid is a strong reducing agent that readily reduces Ag ions. Therefore, the pH of the Ag solution was set precisely to 3. Values even slightly above or below 3 caused Ag to precipitate immediately. After the solution was set, it was spin-coated onto the Ag NW network. Drop casting the solution adversely affected the transmittance, leaving coffee ring marks on the surface. Therefore, it was not considered in the experiments. The resultant change in sheet resistance is given in Figure 2.6 (a). The change was drastically lower compared to that of the literature. The treatment was repeated six times, and only a reduction of 35% in sheet resistance could be achieved. After the treatment, there was also a drop in the optical transmittance, as shown in Figure 2.6 (b). SEM images in Figure 2.6 (c) and (d) also show negligible junction fusion with many irregular Ag depositions on the nanowire surfaces. The FoM of the Ag NW network did not improve much, only changed from 51.25 to 53.12. The haze, however, substantially increased from 4% to 5.1%. This treatment was discontinued since it did not improve optoelectronic properties much.

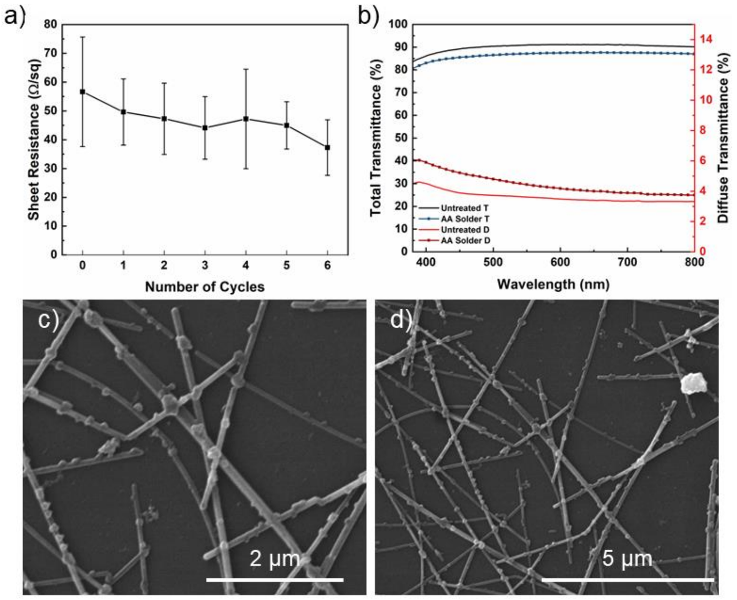

Figure 2.6 a) The sheet resistance and b) spectral optical transmittance and c) and d) SEM images after the AA soldering.

2.3.5 Effect of $NaBH_4$ Treatment

$NaBH_4$ treatment was adapted from the works in the literature. The simplicity and the reported PVP removal efficiency made this treatment attractive. To optimize the treatment, samples were immersed in solutions with different molarities. The sheet resistance of the samples was monitored with each cycle. Higher molarity treatments (1 and 2 M solutions) caused damage to the integrity of the film. $NaBH_4$ produces H_2 bubbles when dissolved in water, and the degree of bubbling is higher in concentrated solutions. This, coupled with $NaBH_4$'s ability to detach Ag-O bonds formed through the carbonyl end of PVP, removes the network altogether from the substrate. The comparison between the solution molarities is shown in Figure 2.7 and the inset photos illustrate the network damage caused at the specified molarities.

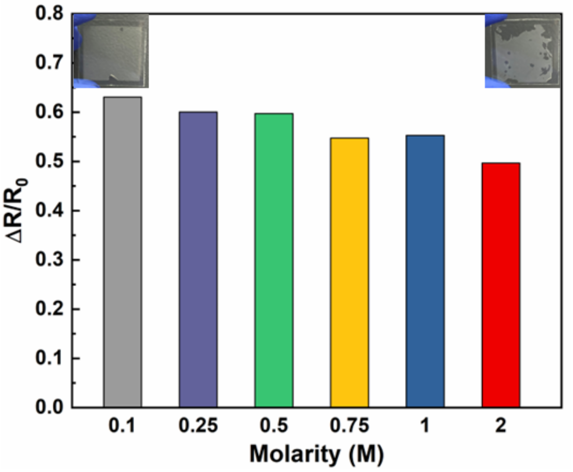

Figure 2.7 The effect of $NaBH_4$ solution molarity on the sheet resistance. Inset photos show the damage on the electrodes.

Compared to the other studies, this treatment was found to be the most effective in reducing the sheet resistance without hindering optical transmittance. Figure 2.7 shows the characteristics of the treatment. The sheet resistance and optical transmittance changes are given in Figures 2.8 (a) and (b), respectively. The SEM images given in Figures 2.8 (c) and (d) do not show any fusion of the nanowires, yet the junction resistance was found to decrease due to PVP removal. The efficacy of the treatment was seen in the FoM, improving from 69.18 to 218.79. The haze did not change much, decreasing from 3.8% to 3.7%, which could be within measurement error limits.

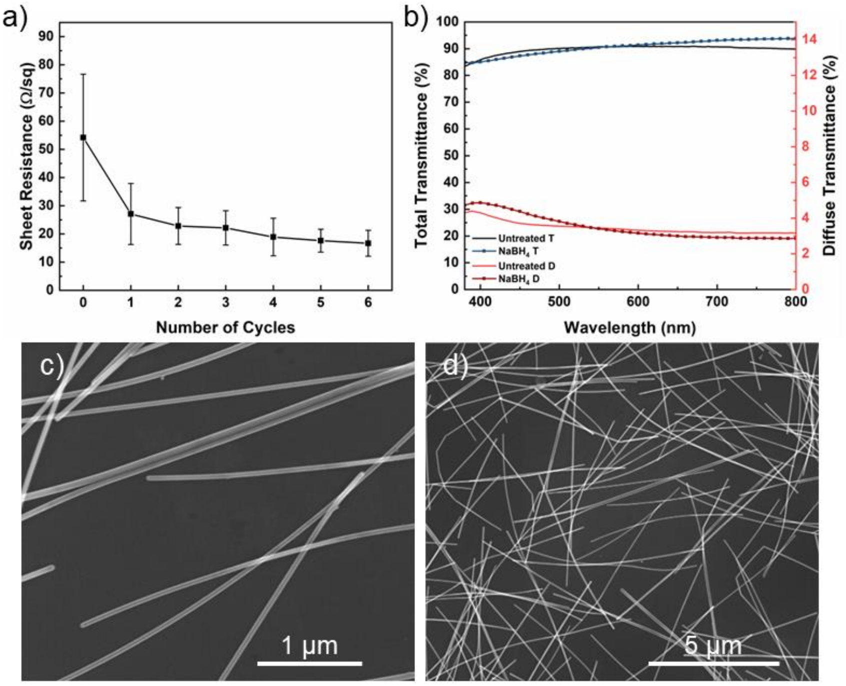

Figure 2.8 a) The sheet resistance and b) spectral optical transmittance and SEM images c) and d) after $NaBH_4$ cleaning.

The PVP removal efficiency was monitored by SERS and XPS studies. SERS is a useful tool due to the plasmonic effect provided by Ag NWs enhancing the signal acquired from PVP. Figure 2.9 (a) shows three stages of the treatment. Before the treatment, three significant peaks were evident that appear at 239, 1591, and 2930 cm^{-1} denoted with red arrows, correspond to Ag-O stretching vibration, C=O stretching vibration and CH_2 skeletal vibration from the PVP molecule, respectively[91]. As the treatment was made, two peaks remain at 562 and 1086 cm^{-1}, which can be attributed to peaks coming from the soda-lime silica glass substrate[92] denoted by green arrows. At the end of the treatment, the vibrations corresponding to PVP adsorption were found to disappear. Therefore, it is possible to say that PVP was cleaned from the nanowire surface. In addition, XPS measurements were made to support the claims, where Ag 3d peaks were analyzed. There is a visible shift in the binding energy of Ag $3d_{5/2}$ peaks from 367.30 eV to 368.30 eV for the treated

Ag NWs. The peak value of 368.3 eV[93] belongs to Ag^0 and the bonded PVP causes a negative shift[84]. This change in the peak positions prove PVP removal from the surface of Ag NWs.

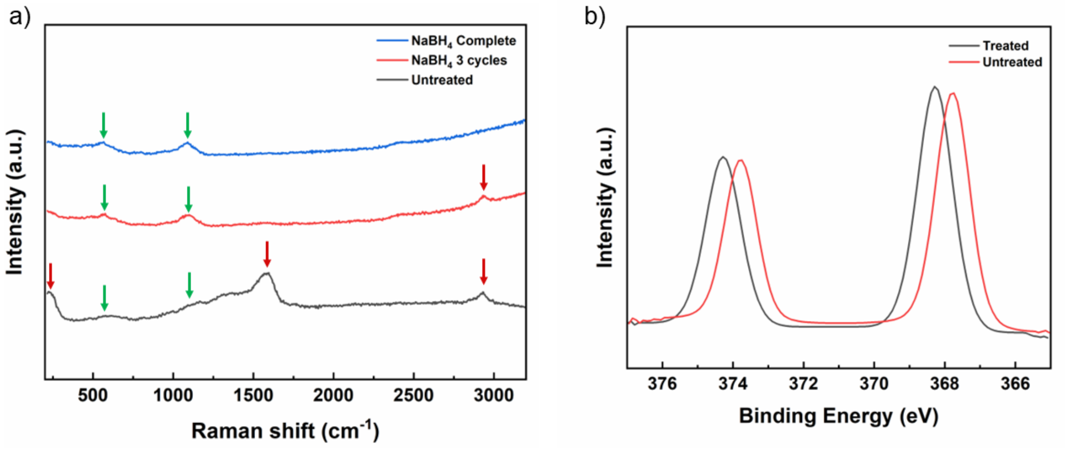

Figure 2.9 a) SERS and b) XPS analyses results from $NaBH_4$ treated Ag NW networks.

2.3.6 Effect of HNO_3-Ag Welding

The HNO_3-Ag treatment was developed in-house, drawing inspiration from various other methodologies. The treatment aimed to use HNO_3 to activate the nanowire surfaces, allowing Ag to be adsorbed. After rinsing, there would be enough Ag adhered to the network, and the heat provided by the furnace would promote Ag welding. The results demonstrated decreased sheet resistance and significant welding at the junctions. Higher Ag amount was examined in the treatment, and the results can be seen in Figures 2.10 (a) and (b) for 0.02 g and 0.05 g $AgNO_3$, respectively. SEM images confirmed the excessive Ag deposition, indicating the need for a lower molarity.

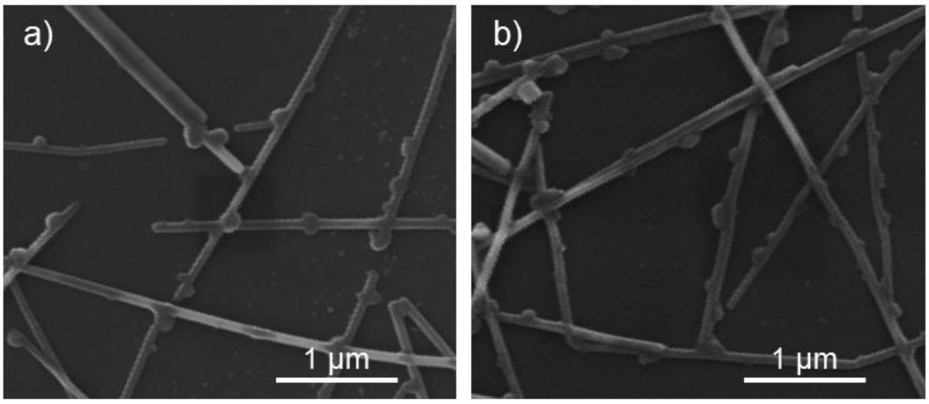

Figure 2.10 The SEM images of a) 0.025 g and b) 0.05 g $AgNO_3$ added solution for HNO_3-Ag welding.

Upon using the 0.01 g $AgNO_3$ solution, the formation of irregular Ag particles was kept to a minimum, though some were still visible in the morphological analysis. The sheet resistance dropped significantly as can be seen in Figure 2.11 (a), and the standard deviation of the sheet resistance was also reduced drastically. SEM image in Figure 2.11 (c) proved the welding in junction areas. This result adversely affected the optical transmittance but not to a noticeable extent. A drop in total transmittance from 91.1% to 90.5% was measured as can be seen in Figure 2.11 (b). The sample's FoM improved from 74.69 to 189.34, while its haze increased from 3.6% to 3.8%. This treatment was therefore considered to be an effective chemical welding process.

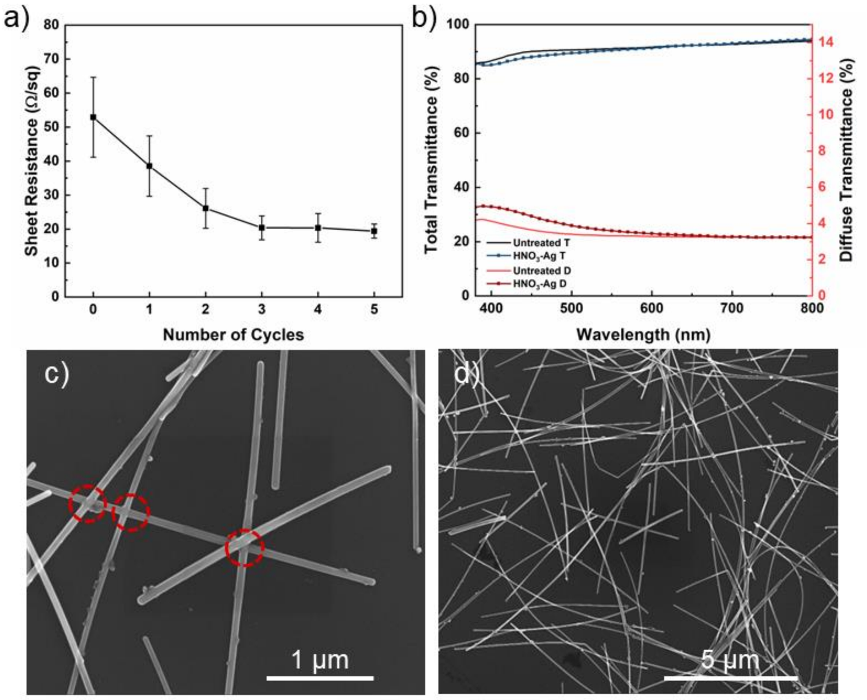

Figure 2.11 a) The sheet resistance and b) spectral optical transmittance and SEM images c) and d) following HNO_3-Ag welding.

2.3.7 Effect of Halide Welding

The halide welding treatment was taken from the literature without any alterations. The welding process and mechanism were explained thoroughly in Chapter 1. Initially, 0.5 M NaF solution was used in the study, though the results indicated no change in the sheet resistance of the sample through the increased exposure time. Higher NaF concentrations were investigated; however, the results were similar. Figure 2.12 (a) shows the sheet resistance change using 2 M NaF solution. No appreciable change could be observed. The SEM images given in Figures 2.12 (c) and (d) prove that there was no fusion of nanowires, as indicated with the dashed red circles. The optical transmittance also did not change, as Figure 2.12 (b) suggests. FoM increased minimally from 68.78 to 70.24. The haze also did not change, staying still at 4.1% for both samples. This treatment was determined to be unsuitable for the batch of Ag NWs used in this work.

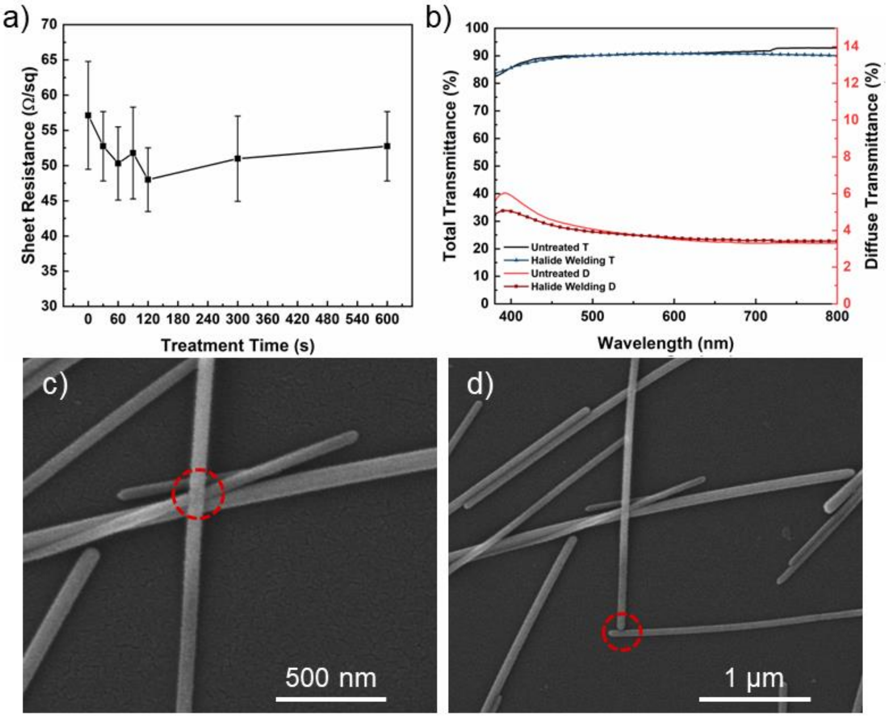

Figure 2.12 a) The sheet resistance and b) spectral optical transmittance and SEM images c) and d) after halide welding.

2.3.8 Effect of Hot Water Treatment

The hot water treatment was performed on Ag NWs to remove excess PVP around the network. Following rinsing with ethanol, one would expect the welding of the junctions due to capillary forces. The sheet resistance measurements and SEM images provided in Figure 2.13 (a) show no significant change from the untreated sample. SEM images provided in Figures 2.13 (c) and (d) display no fusion of the Ag NWs. The reduction in the sheet resistance of the sample resulted in the FoM improving from 80.85 to 133.28. The calculated haze for this sample changed minimally from 3.6% to 3.8%. The treatment was discontinued due to the limited enhancement in the optoelectronic performance of the Ag NW network.

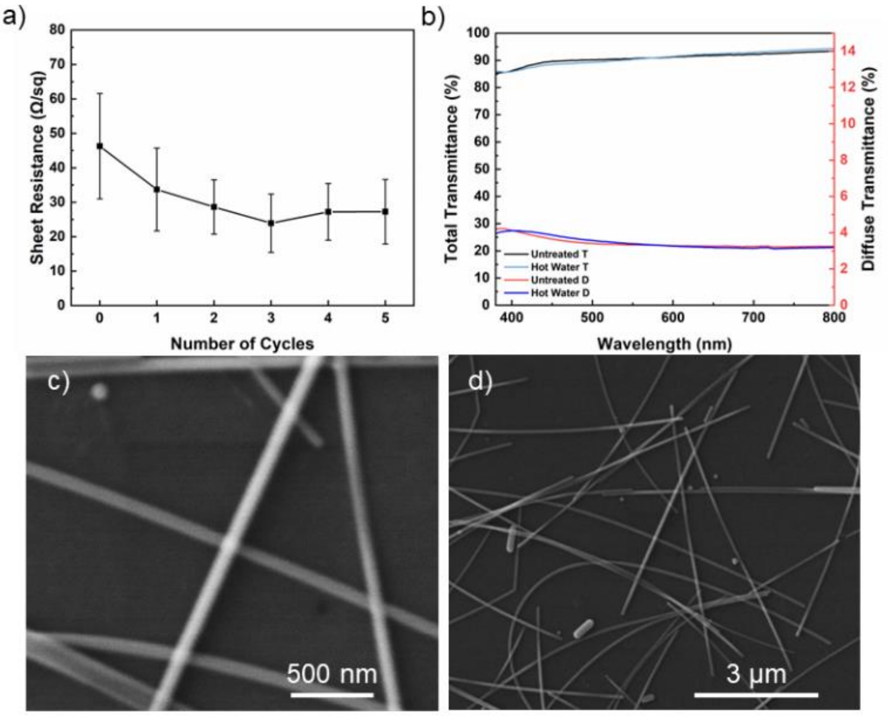

Figure 2.13 a) The sheet resistance and b) spectral optical transmittance SEM images and c) and d) after halide welding.

2.3.9 Fabrication of Optimized Silver Nanowire Networks

After finding the most successful treatments for the Ag NW networks, it was noticed that the treatments followed different aims. The $NaBH_4$ treatment was applied to remove PVP from the surface, and the HNO_3-Ag treatment deposited Ag to weld the nanowires. The combination of the two treatments was realized in Figure 2.14 (a). The sheet resistance values were dropped to 12.4 Ω/sq, the lowest achieved without hindering the optical transmittance as can be seen in Figure 2.14 (b). The reduced standard deviation suggested that the treatment also homogenized the resistance distribution along the surface of the Ag NW network. The SEM images provided in Figures 2.14 (c) and (d) support the claim of clean, welded nanowires without redundant Ag deposition around the junctions. A small increase in the haze was observed, though this was also expected due to the deposition of Ag around the nanowires. The final FoM of 304.67 was the highest among all treatments applied, starting from 66.20. The increase in the haze was also within acceptable means, increasing from 4% to 4.5%. Measuring the stability of the sample, it was found that there was a 30% increase in the sheet resistance after 2 months. A considerably longer period of measurements is still required to comprehensively assess the stability.

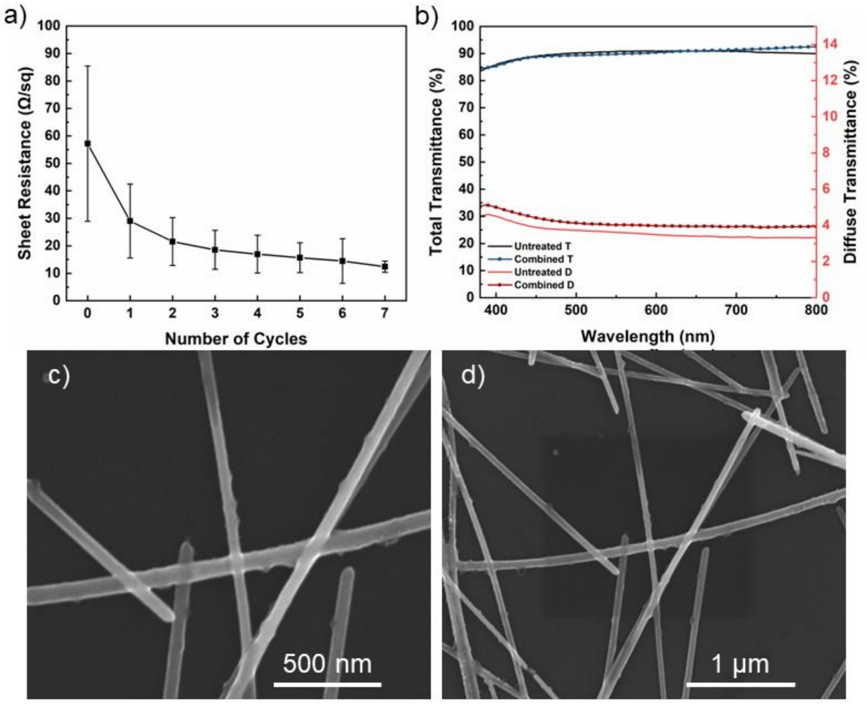

Figure 2.14 a) The sheet resistance and b) spectral optical transmittance and SEM images c) and d) after combined optimized post-treatment method.

Figure 2.15 compares the FoM obtained after each treatment and provides guidelines for FoM values. The primary objective was to attain the highest possible FoM, with the optimized combined treatment emerging as the one that achieved the highest FoM. Table 2.1 summarizes the applied treatments and provides the initial sheet resistance, optical transmittance, haze, and FoM values compared to the post-treated ones.

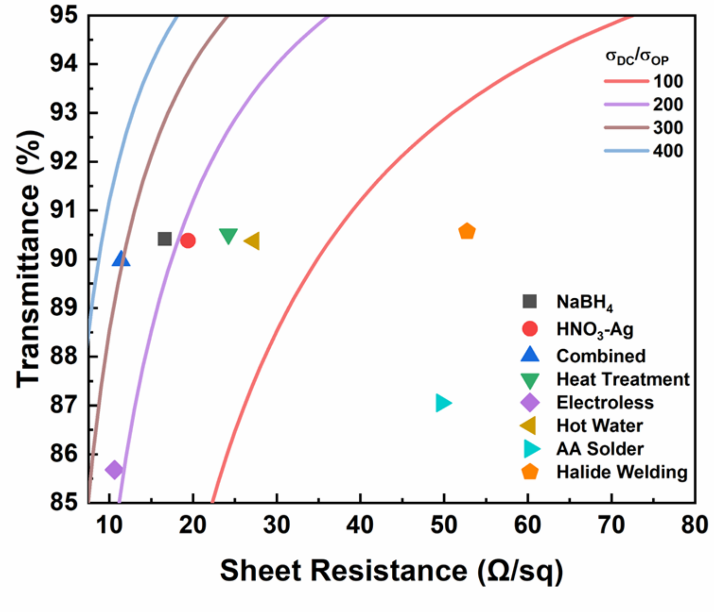

Figure 2.15 The resultant optoelectronic properties of all post-treatments performed on Ag NW networks. Solid lines provide FoM values of 100, 200, 300, and 400.

Table 2.1 Optoelectronic characteristics of Ag NW networks before and after the post-treatments.

	Before					*After*				
Treatment	R_{sh} (Ω/sq)	Tt (%)	Td (%)	FoM	Haze (%)	R_{sh} (Ω/sq)	Tt (%)	Td (%)	FoM	Haze (%)
Heat Treatment	58.2	90.7	3.3	65.06	3.7	24.1	90.5	3.2	152.83	3.6
Electroless	49.57	91.3	3.3	81.57	3.6	10.63	85.4	6	220.89	7
AA Solder	56.65	90.9	3.6	68.34	4	37.27	87.1	4.4	70.73	5.1
$NaBH_4$	54.21	90.7	3.5	69.12	3.8	16.69	90.4	3.4	218.7	3.8
HNO_3-Ag	52.88	91.1	3.3	74.63	3.6	19.4	90.5	3.6	189.43	3.8
Hot Water	46.28	90.6	3.4	80.78	3.6	27.25	90.4	3.4	133.35	3.8
Halide Welding	57.13	90.7	3.8	65.74	4.1	52.75	90.6	3.7	70.38	4.1
Combined	57.21	90.7	3.6	66.18	4	11.4	90	4	304.69	4.5

2.4 Conclusions

This work compared the effectiveness of various post-treatment methods on improving the FoM of Ag NW networks. Investigated post-treatment methods were obtained from literature or developed in-house. Since the reported works use completely different Ag NWs with diverse intrinsic properties and deposition methods, their applicability to any given set of Ag NWs was unknown. The results of each method were reported and analyzed by measuring the sheet resistance and optical transmittance of the samples. SEM images provided support to the analysis. A two-step post-treatment method was developed, where first the PVP layer was removed from the network by applying a facile $NaBH_4$ treatment, followed by chemical welding through HNO_3-Ag treatment. The FoM of the electrodes was calculated through the sheet resistance and total optical transmittance values. FoM values were initially measured at 66.20 and improved to 304.67, which was a highly competitive value. The network was also stable in ambient conditions, showcasing its potential in many optoelectronic applications.

CHAPTER 3

OPTIMIZED SILVER NANOWIRE NETWORKS FOR TRANSPARENT LIQUID-SOLID INTERFACE TRIBOELECTRIC NANOGENERATORS

3.1 Introduction

3.1.1 Contact Electrification and Triboelectric Nanogenerators

Contact electrification (CE) is a phenomenon where charge transfer occurs between two materials that come into contact. It has been known for more than 2600 years[94]. Many concepts were developed using CE, such as triboelectric nanogenerators (TENGs)[95], air filtration[96], and interface spectroscopy[97]. TENGs arise from triboelectrification, which is the CE of matter. Solids, liquids, and gases are known to exhibit CE. Triboelectrification is observed in numerous situations, with most being byproducts of mechanical motion occurring naturally. Examples of mechanical motion include human motion[98], wind[99], vibration[100], water flow[101], and droplets[102], which can be harvested. Wang and his coworkers realized the potential of triboelectrification and found a niche for energy harvesters. They first introduced TENGs that aim to harvest the energy generated through triboelectrification. Scientists manipulated the CE and, through intelligent circuit and electrode design, reported numerous devices capable of harvesting energy. These works inspired other researchers to pursue the underlying mechanisms of CE and develop more efficient and robust TENGs.

TENGs have been popular among energy harvesting devices due to their low cost of materials, simple designs, and robustness. Many devices have been developed to harvest energy from biomechanical motion[103], wind[99], and water waves[104]. The power outputs of TENGs were high enough to charge capacitors, power digital calculators, and light up tens of LEDs. TENGs provided creative solutions to some everyday issues. Through machine learning, tactile sensors have been used for pressure sensing[105], digital twin controlling[106] and object recognition[107]. Wind speed and direction sensors[108] were developed to monitor the behavior of the wind. Acoustic sensors[109] could identify the speakers and had clear resonance spectra.

Most of the research on TENGs considered the CE between two solid surfaces. In order to comprehensively comprehend the origins of CE and explore methods of manipulation, extensive studies have been conducted. Mechanisms for CE in solid-solid contact modes have been developed. Electron transfer, ion transfer, and material transfer have been designated as the three main mechanisms of CE. In this chapter, the solid-solid interface mechanisms will not be discussed further. Extensive work on liquid-solid interface mechanisms has been conducted and the following section provides insight into the development of liquid-solid CE models.

3.1.2 Liquid-Solid Interface Contact Electrification

Liquid-solid interface CE is a relatively recent development in the TENG field[110]. The full story regarding the mechanism is still debated, yet a couple of theories exist as plausible explanations. Two main problems are stated in liquid-solid interface CE[111]: the charge carriers' identity and the electrical double layer (EDL) formation. Proposals on charge transfer included the adsorption of ions in the liquid to the solid surface or chemical reactions occurring on the surface providing the electrons transfer.

In liquid-solid CE, electron transfer is found to be the dominating mechanism. The Wang transition model, also known as the electron cloud model[94], explains the condition necessary for electron transfer in CE. Figure 3.1 (a) shows the two atoms in equilibrium conditions, separated by a distance of *d*. When this distance becomes larger than *d*, the two atoms will attract each other, and conversely, when the distance becomes lower than *d*, the two atoms will repel each other. Wang argued that for electron transfer in CE to occur between two atoms, their electron clouds must overlap. Figure 3.1 (a) shows the two atoms at the equilibrium distance *d*, with atom A having more electrons occupying higher energy levels than atom B. No electron transfer occurs at this distance. However, when the two atoms' electron cloud overlap, that is, when two surfaces come in close contact, electron transfer occurs from atom A to atom B. Electrons flow from the highest energy level, reducing the potential difference between the two, as shown in Figure 3.1 (b). As the electrons move to atom B, photon emission is observed as described in Figure 3.1 (b, i-iii). The overlap of electron clouds reduces the potential barrier and creates a bond between the two atoms allowing the electron flow. As the two surfaces are separated, atom A is dragged away along with the rest of the surface, and the bond between atoms is eventually broken. The result is CE between the two surfaces; in the case where the attraction between atoms A and B is stronger than atom A and the bulk, it remains on the surface by forming a chemical bond with atom B. Therefore, CE cannot be detected. Liquid-solid TENGs work on this basis, and the motion of the liquid on the solid surface provides electron transfer.

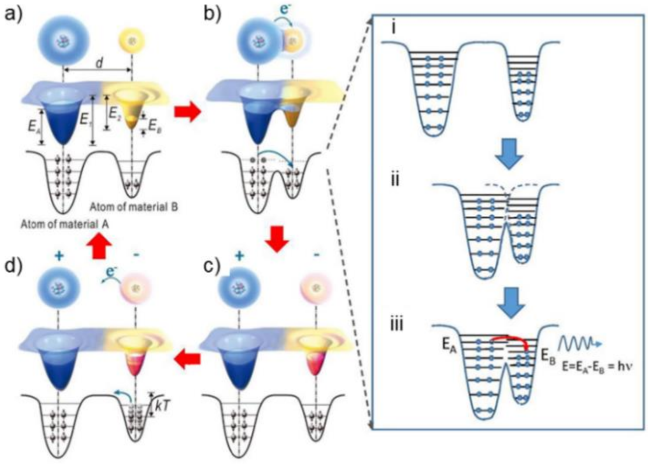

Figure 3.1 A schematic describing the electron transport mechanism of CE. a) Atoms A and B in equilibrium conditions. b) Atoms come in contact and electron transport occurs (i-iii) shows the process in detail. c) Atoms separate and are charged. d) charges are released from the atom upon fulfilling energy barrier[94].

The ions in the liquid might also stick to the solid surface[112]. This is explained in the ion transfer model, where ions naturally occurring or dissolved in water interact with the atoms on the solid surface. The phenomena depend on a couple of factors; hydrophobicity of the surface and chemical reactions involving the surface and dissolved ions. It was found that hydrophobic surfaces exhibit less ion transfer due to the high water contact angle providing less surface contact area. Therefore, fewer ions stick to the surface and provide less ion transfer. The surface material is of great concern due to free ions' affinity to some materials. It was found that some materials, such as silica, interact with dissolved sodium hydroxide, where -OH ions stick to the surface, manipulating the EDL. Furthermore, the ions remaining on the surface often reduce the electrical output of the devices upon continuous exposure.

To distinguish electron and ion transfer on the surface, the samples were heated up to temperatures above 200 °C. Thermionic emissions were documented[113] by measuring the surface charges before and after each heating cycle. It was found that initially, most charge accumulated was released, proving that electron transfer is the leading mechanism in CE. However, as the surface was subjected to more dissolved ions, the 'sticky charges' accumulated and reached saturation, meddling with the EDL further. This necessitated an expansion of the explanation of EDL.

Wang developed a hybrid two-step EDL[94] model combining electron and ion transfer mechanisms to explain the whole picture. In the first step, the liquid wets the surface allowing ions and molecules within the liquid to interact with the surface. Electron transfer between the atoms from the solid and water molecules takes place by the overlapping of electron clouds. The electron transfer occurs from a high energy state to a lower energy state. Solid surfaces with high electron capturing ability can directly obtain electrons from water molecules and even ions dissolved in the liquid. As the liquid flows through the surface, the initial contact formed by water is broken. The electrons can stay in the transferred surface provided and the energy required to surpass the energy barrier is high enough to keep them at that energy state. In the second step, due to the charging of the solid's surface, free ions in the liquid are attracted to the surface by van der Waals attraction. This process forms an EDL akin to that of a traditional model. Simultaneously, ionization reactions occur on the surface, and when water molecules lose an electron, they form H_2O^+. This is an unstable molecule that reacts with a nearby water molecule to form OH^- and H_3O^+ ions, further enhancing the EDL. These two ions are situated near the solid's surface. The formation of the Stern or diffuse layers is no different in the two-step model.

Another important facet of TENGs is the triboelectric series. The triboelectric series is a quantitative ranking of materials' triboelectric polarization. It was found that materials such as polydimethylsiloxane (PDMS), polytetrafluoroethylene (PTFE), and fluorinated ethylene propylene (FEP) rank on the negative side, and poly(vinyl) alcohol (PVA), silk, and leather are positively polarized[114]. As is the case with solids, liquids, too, have a triboelectric series[115]. Yoo et al. developed a method of testing various liquids and ranked them according to their triboelectric polarization. An FEP-coated aluminum electrode was immersed in the test liquid. A Faraday cage surrounding the setup ensured precise measurements. Through continuous ascent and descent into the liquid, the charging around FEP was measured. To neutralize charge distribution on the surface, ethanol was sprayed onto FEP to provide a "reset" in between each measurement. On the positive side, Sorbitol F ranked first, followed by glycerol and deionized water, whereas, on the negative side, Hyamine 1622, butyl acetate, and methyl acetate were ranked. Deionized water ranking among the tribopositive materials leads it to be paired with tribonegative surfaces such as PDMS, PTFE, and FEP.

3.1.3 Droplet-Based Liquid-Solid Triboelectric Nanogenerators

Within liquid-solid TENGs, droplet-based devices provide an intriguing alternative in rain energy harvesting and sensing. Energy harvesters could successfully light LEDs, whereas the sensors were self-powered and could measure pH and chemical concentration. The first proposals of such setups were seen in 2014 when Wang et al. used a single-electrode device to measure the voltage and current of the incident water droplets.

In a study by Hu et al.,[116] a droplet-based sensor was developed for biomedical applications. The device consisted of an interdigital-cut copper sheet sandwiched between two double-sided tapes. Then, it was dip-coated with fumed silica particles providing superhydrophobicity. The device was flexible enough to roll into a tube and could be placed into a silicon drop counter often found in serum kits. The schematic in Figure 3.2 (a) shows the device structure. The number of incident droplets could be counted regardless of the liquid impacting the electrode, showcasing the device's versatility, as shown in Figure 3.2 (b). Furthermore, the device was proposed as a real-time infusion monitoring system, which could be combined with a wireless signal transmitter. Therefore, the situation of a patient could be followed closely and precisely.

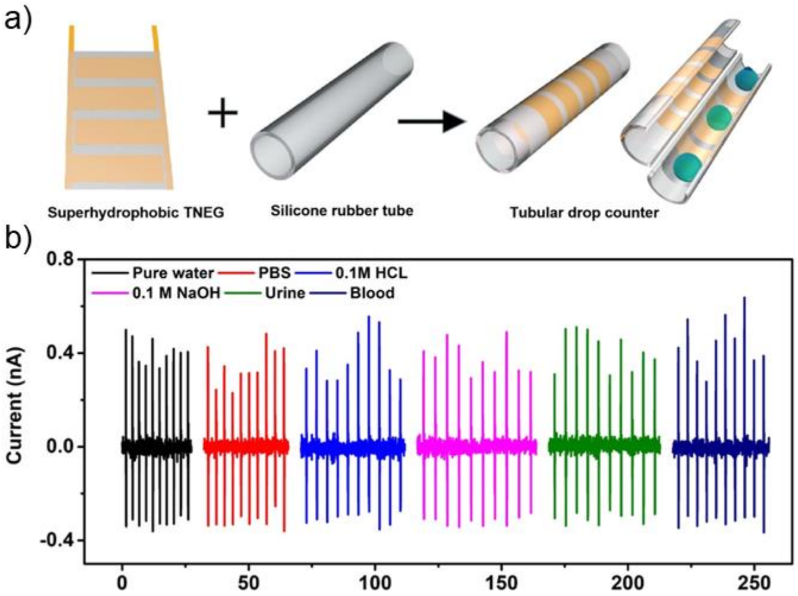

Figure 3.2 a) The schematic drawing of the droplet-based TENG. b) The electrical output of the device using various liquids[116].

Displaying the energy harvesting potential of droplets, Xu et al.[117] reported their transparent droplet-based energy generator (DEG) device. They utilized the CE between the positively charged droplets and tribonegative PTFE coated on an ITO glass, a schematic of which is given in Figure 3.3 (a). The device consisted of two electrodes, one being ITO and the other a thin aluminum wire, to harvest energy from droplets. A setup utilizing multiple DEGs was prepared, and droplets coming from a water reservoir resulted in the generation of 143.5 V and 0.27 mA in one DEG, displayed in Figures 3.3 (e) and (f). The charge saturation with each impinging droplet is given in Figure 3.3 (c). Figure 3.3 (b) shows a photograph of the multiple DEG units. The instantaneous power density achieved was 50.1 W/m^2 per droplet. The capability of the DEG was shown with 4 connected DEG units lighting up 400 LEDs with each impinging droplet, as shown in Figure 3.3 (d).

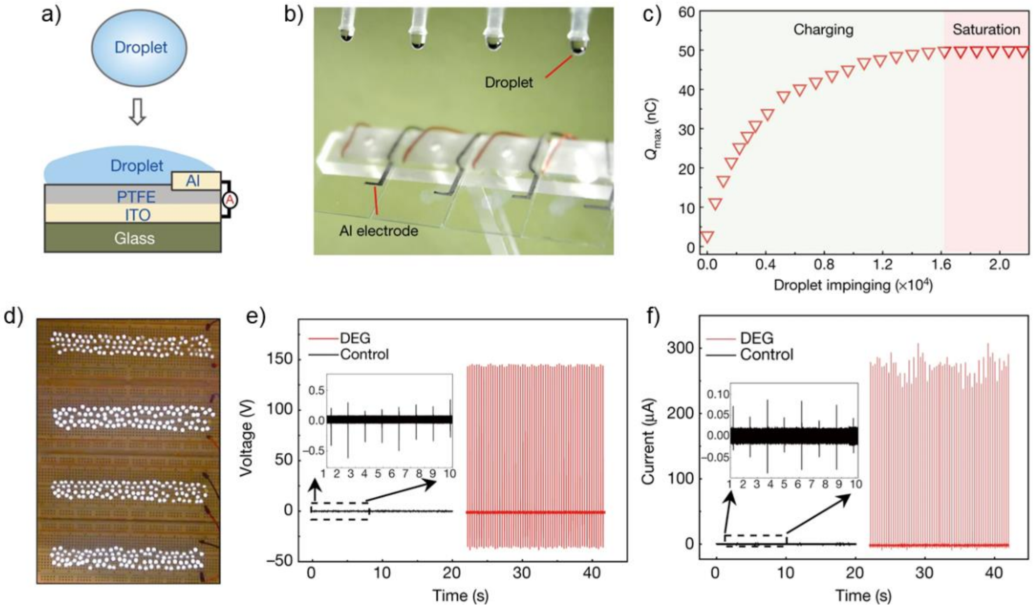

Figure 3.3 a) The device setup. b) Photos of 4 DEG units. c) The charge characteristics of DEG. d) Lit LEDs powered by DEGs. e) voltage and f) current output of DEG compared to the control device.

A position sensor for droplets using liquid-solid interface TENGs was developed by Hu et al.[118] In the study, four identical PDMS/copper tape units were prepared. An inkjet nozzle sprayed the droplets to different points along each unit. Each unit's voltage output was measured upon contact with a droplet. The voltage was related to the spreading droplet's radius, and using 4 electrodes, it was possible to determine the droplet's position precisely. A software was developed to monitor the exact location of the droplet with the error. The work paves the way for novel applications in droplet-based TENGs, drawing attention to machine-learning interfaces and IoT-controlled devices.

Still, in every transparent droplet-based TENG, TCOs are used. This chapter demonstrates the use of the optimized Ag NW networks as the current collector in the TENG devices. PDMS is coated onto the Ag NWs as the tribonegative layer. Incident water droplets provide the CE, which allows the production of voltage and current. The proposed TENG sensor is capable of sensing solution concentration and pH levels. A large-area Ag NW-based transparent heater is integrated to the transparent TENG sensor that is used to active the heater.

3.2 Experimental Details

3.2.1 Preparation of the Liquid-Solid Interface Transparent TENGs

The Ag NWs were synthesized and purified, as explained in Chapter 2. Soda-lime-silica glass slides were cut into 1 x 1 inch squares and ultrasonically cleaned with acetone, ethanol, and deionized water for 10 minutes each. The silver paste was applied to opposite sides of the cut glasses as contacts. The spray coating and post-treatment of the Ag NW networks were applied as per Chapter 2. A nanosecond laser (FiberLAST-NanoMark Energy Series) patterned the Ag NWs into interdigital electrodes. For patterning, Ag NWs were removed from the surface using 20 W power, 50 kHz frequency, and 100 mm/s scanning speed. 8, 12, and 16 interdigitated fingers were patterned. Then, PDMS (Sylgard 184) was mixed with the curing agent in a 10:1 ratio by weight. A vacuum oven at room temperature was used to remove the bubbles inside the PDMS. Then, PDMS was spin-coated onto the patterned electrodes to obtain a thin and continuous coating and cured at 100°C for 45 minutes.

The large-area droplet sensor-activated heater was prepared similarly. The 15 cm x 15 cm soda-lime-silica glass was cleaned with acetone, ethanol, and deionized water.

Then, the silver paste was applied separately as contacts for the sensor and the heater. Afterwards, Ag NWs were deposited as described earlier. The large-area coating of PDMS was performed by a modified Mayer rod system followed by curing at 100°C for 1 hour. An aluminum tape was cut and placed in a line along the PDMS layer for the second electrode.

For heater activation, a simple MOSFET circuit was devised. A power supply was set to provide a bias voltage of 30 V. An Arduino processor was used to read the voltage data from the sensor. The voltage produced by the incident droplets allowed the MOSFET to transfer the current from the power supply to the heater. A thermal camera (Optris PI-400) was used to monitor the changes in temperature and obtain images of the heater.

3.3 Characterization of the Liquid-Solid Interface Transparent TENGs

3.3.1 Scanning Electron Microscopy (SEM) Analysis

The SEM analysis of the TENG devices were made through FEI NOVA NANO SEM 430 at an operating voltage of 15 kV. For images on glass substrates, a very thin gold layer was sputtered onto the sample.

3.3.2 Triboelectric Measurements

Platforms with 60° slots for TENG measurements were 3D printed. Using a syringe pump, water droplets were delivered to hit the device. The open circuit voltage (V_{OC}) and the short circuit current (I_{SC}) of the TENGs were measured using a Keithley 6514/E-Electrometer, a LabView code was used for data collection.

3.3.3 TENG-Activated Heater Measurements

The droplet sensor TENG was combined with Ag NW heater in a single device. In this device TENG signal generated with water droplets were used as a switch for controlling the Ag NW-based heater. TENG output generated with individual droplets were passed through a full bridge rectifier and connected to analog input of the microcontroller unit (MCU) (Arduino Mega). Depending on the frequency and amplitude of the TENG signals, the gate voltage of the logic-level n-type MOSFET (IRL540N) was controlled with the digital output of the MCU. Consequently, the DC source powering the Ag NW heater was turned on after activation through water droplets.

3.4 Results and Discussion

The optimized Ag NW networks were prepared as droplet-based transparent TENG devices. In order to serve as a current collector, the sheet resistance of the Ag NW network was minimized to achieve the lowest possible level. The obtained electrode had a sheet resistance of 6.32 Ω/sq. Laser patterning was then utilized to separate the electrode into two. A photo of the prepared interdigitated electrode is provided in Figure 3.4 (a). The drawing of the interdigitated pattern shape for laser patterning, with the dimensions is given in Figure 3.4 (b). The interface separating the laser patterned region and the Ag NW network was clear, as can be seen in Figure 3.4 (c). The laser patterned region ablated and spheroidized the Ag NWs due to immense localized heating. The thickness of the spin-coated PDMS layer can be seen in Figure 3.4 (d). PDMS was 48 μm thick, was covering the entire surface of the Ag NWs and was electrically insulating.

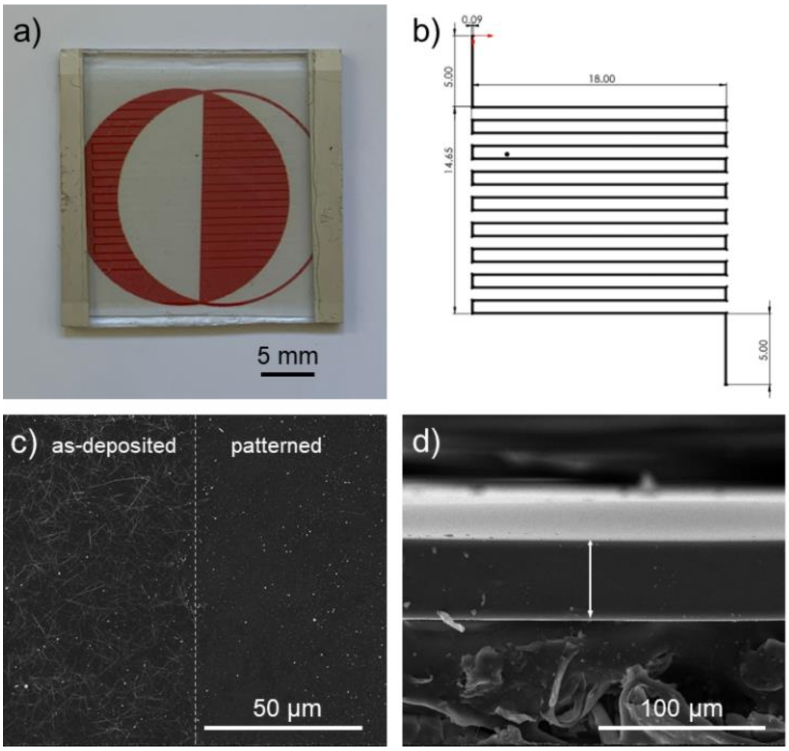

Figure 3.4 a) Photograph of patterned Ag NW electrode. b) The drawing of the interdigitated pattern shape. c) SEM images of patterned and as-deposited regions. d) Cross-sectional SEM image of the PDMS layer.

Figure 3.5 provided the working mechanism of the device in a freestanding mode. Herein, the Ag NWs acted as the current collector, PDMS was the tribonegative layer, and the water droplets were the tribopositive layer. Once a droplet impacts PDMS, CE occurs, and negative charges were induced on the surface of PDMS while the water droplet was positively charged as seen in Figure 3.5 (ii). The interdigitated structure on which the droplet resides were first negatively charged to screen the positive charges of the droplet. The electrode surface without droplet was charged positively to neutralize the charges of negatively charged PDMS. As the droplet slides down over the other parts of the interdigitated electrode, electrons move through the contact and create a peak, as observed in Figure 3.5 (iii). The new part of the interdigitated electrode becomes negatively charged and screens the positive charge of the water droplets. As the droplet moves through the surface of PDMS, an alternating peak can be seen typical of a freestanding mode TENG[119].

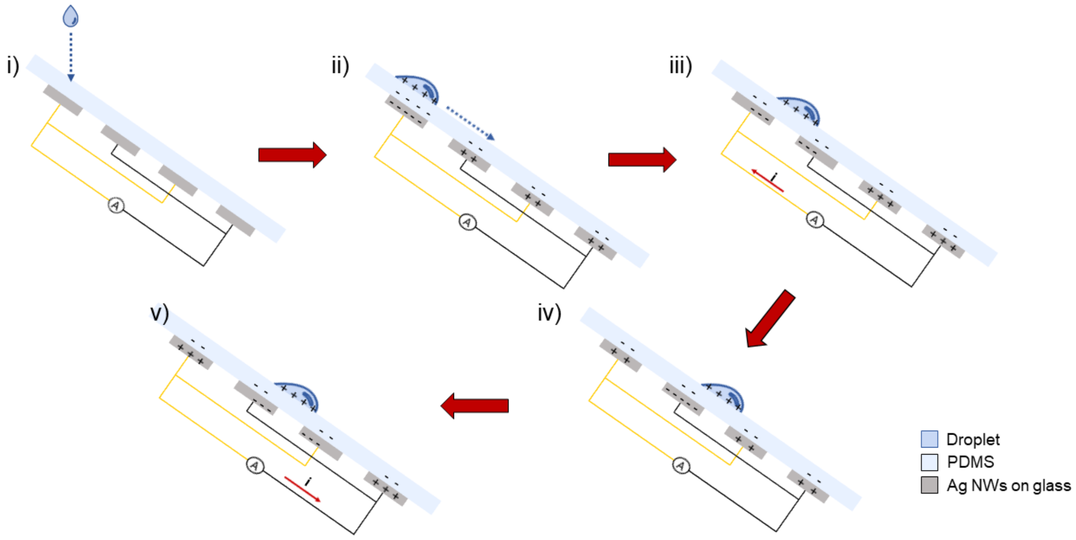

Figure 3.5 The working mechanism of the freestanding mode droplet TENG.

In order to hold the TENG device firmly and reproducibly at an angle of 60°, a 3D printed sample holder was prepared. Additionally, the sample holder allowed easy connection of the TENG device to the measurement setup with allocated spaces for cords, given in Figure 3.6.

Figure 3.6 A photograph of the 3D printed TENG sample holder.

As the droplets move between the interdigitated electrodes, a backflow of electrons was observed, creating the peaks. This way, alternating current peaks were observed as droplets continue sliding down the device. The characteristics of the alternating short-circuit current and open-circuit voltage are given in Figures 3.7 (a) and (b), respectively.

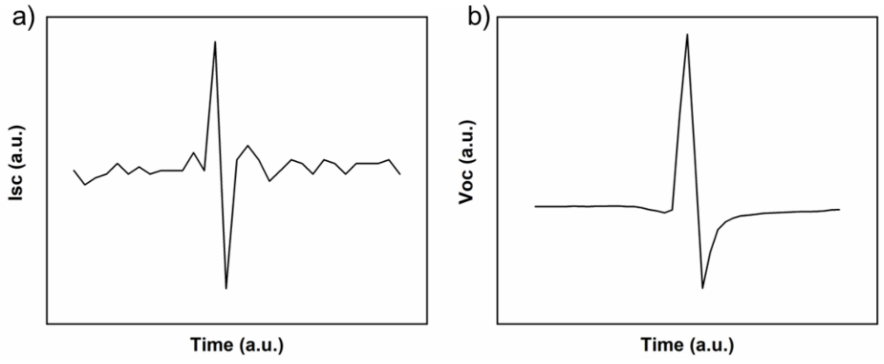

Figure 3.7 The Isc and b) the Voc outputs of for a single peak of the interdigitated TENG structure.

There were multiple factors that affect the electrical output of the fabricated devices. Namely, the droplet height, size of the droplets, and angle of incident droplets. The height of the droplets was fixed at 10 cm above the substrate due to limitations regarding the experimental setup. The volume of the droplets was fixed at 0.3 microliters. The angle of incidence was fixed at 60° to ensure that droplets slide down smoothly. From this point, the parameters of the syringe pump were considered. The flow rate of water from the syringe pump was discovered to be an effective factor in the analysis and flow rates of 25, 50, and 100 ml/h were investigated in initial TENG tests. Figures 3.8 (a) and (b) shows the Isc and Voc values obtained with respect to the flow rates. The variation in flow rate was observed to have minimal impact on the electrical output. For flow rates of 25, 50, and 100 ml/h, currents of 7.4, 7.1, and 7.3 nA, and voltages of 0.26, 0.28, and 0.27 V were obtained, respectively. However, at a flow rate of 100 ml/h, it was found that droplets impact the surface too frequently. At times, droplets impinged on the surface before the other droplet was sliding out. This flow rate was deemed to be far too fast for effective sensing. Therefore, further experiments were conducted using flow rates of 25 and 50 ml/h.

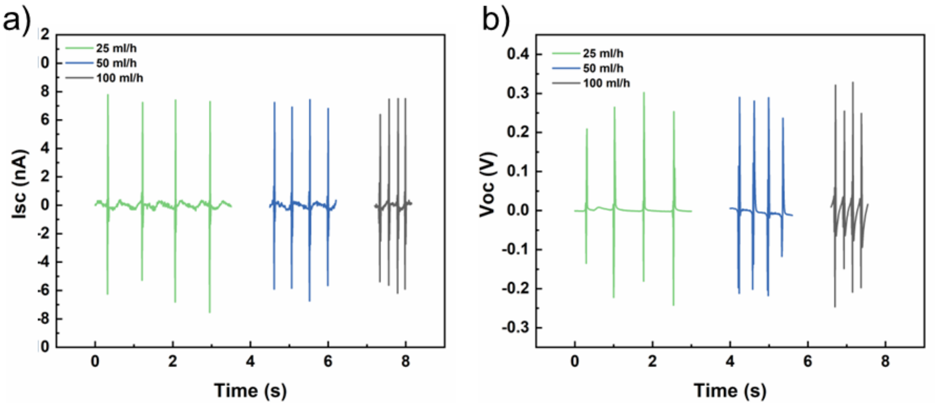

Figure 3.8 a) Isc and b) Voc output of the TENG under liquid flow rates of 25, 50, and 100 ml/h.

To gauge the effect of the optimized sheet resistance values arising from the post-treatments, an untreated Ag NW network at a sheet resistance of 55 Ω/sq was used as the current collector. The electrical output of the TENG device was compared to that of the treated Ag NW network. The resulting Isc and Voc values using a droplet flow rate of 50 ml/h are given in Figures 3.9 (a) and (b), respectively. The peak Isc and Voc values reached were found to be slightly lower at 6.5 nA and 0.25 V, respectively. Having a current collector with high electrical conductivity is essential for large range of signal detection for TENGs. Factoring in the magnitude of Isc and Voc values, the reduction in the sheet resistance did not make a significant improvement. However, striving for a lower sheet resistance value would necessitate depositing a higher quantity of Ag NWs, consequently impeding optical transmittance.

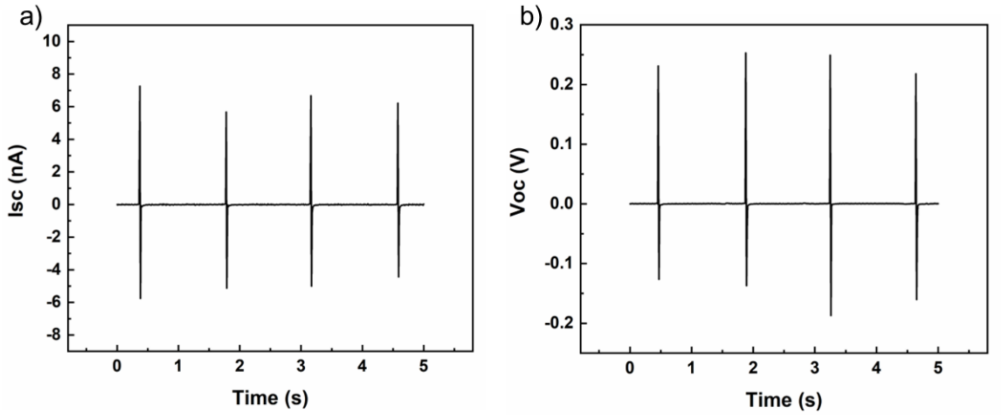

Figure 3.9 The Isc (a) and Voc (b) output of the TENG using an untreated Ag NW network as its current collector.

The pH sensitivity of the TENG was displayed in acidic pH values. Aqueous solutions of HCl with pH values of 1, 3, and 5 along with DI water (pH 7) was used for the measurements. The same experimental setup was used. The Isc and Voc outputs of the device provided the sensing data. The outputs of the device operated at flow rates of 25 and 50 ml/h are given in Figures 3.10 (a-d). It was seen that the flow rate of droplets did not affect the output performance significantly. Similar Isc and Voc values were obtained from both flow rates. The average Isc values obtained for pH values of 1, 3, 5, and 7 were 1.43, 3, 5.11, and 7.85 nA, respectively. For those samples average Voc values of 0.022, 0.11, 0.18, and 0.26 V were obtained. However, there was an increase in the Isc and Voc values with increasing pH. A trend could clearly be seen correlating the pH with the peak voltage and current levels. This behavior could be attributed to Wang's hybrid model, clearly showing the number of foreign ions in DI water affecting the output performance of TENGs. The EDL formed at the droplet-PDMS interface consists of more densely populated H^+ and Cl^- ions at lower pH values. This reduces the surface charge density of PDMS and therefore impedes the current generation.

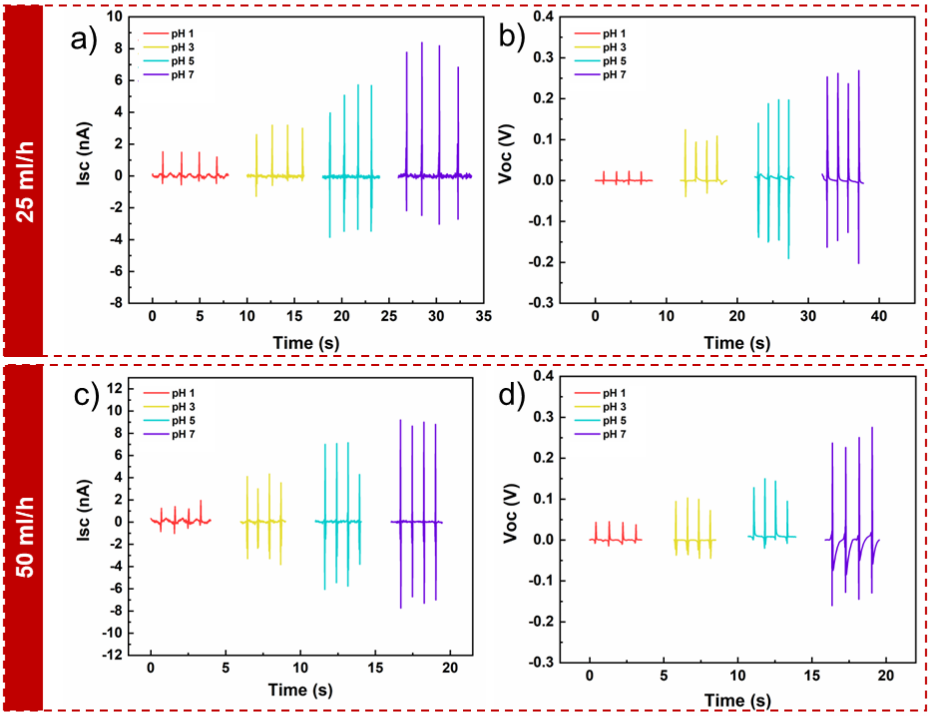

Figure 3.10 The pH sensing capabilities of the TENGs. a) Isc and b) Voc values obtained at a flow rate of 25 ml/h. c) Isc and d) Voc values obtained at a flow rate of 50 ml/h.

The concentration sensing capabilities of the device was realized by dropping aqueous NaCl solutions onto the TENG. The solutions were categorized by molarity and their electrical outputs were realized at flow rates of 25 and 50 ml/h. The electrical outputs of different NaCl molarities are provided in Figures 3.11 (a-d). The results with increasing molarity were similar to the pH sensing measurements, where a decrease in the Isc and Voc values was observed. The average Isc values for 1 M, 0.1 M, 0.01 M NaCl and deionized water droplets were recorded as 1.11, 3.67, 5.86, and 7.6 nA, respectively. Furthermore, the average Voc values corresponding to the mentioned molarities were measured at 0.09, 0.14, 0.21, and 0.27 V, respectively.

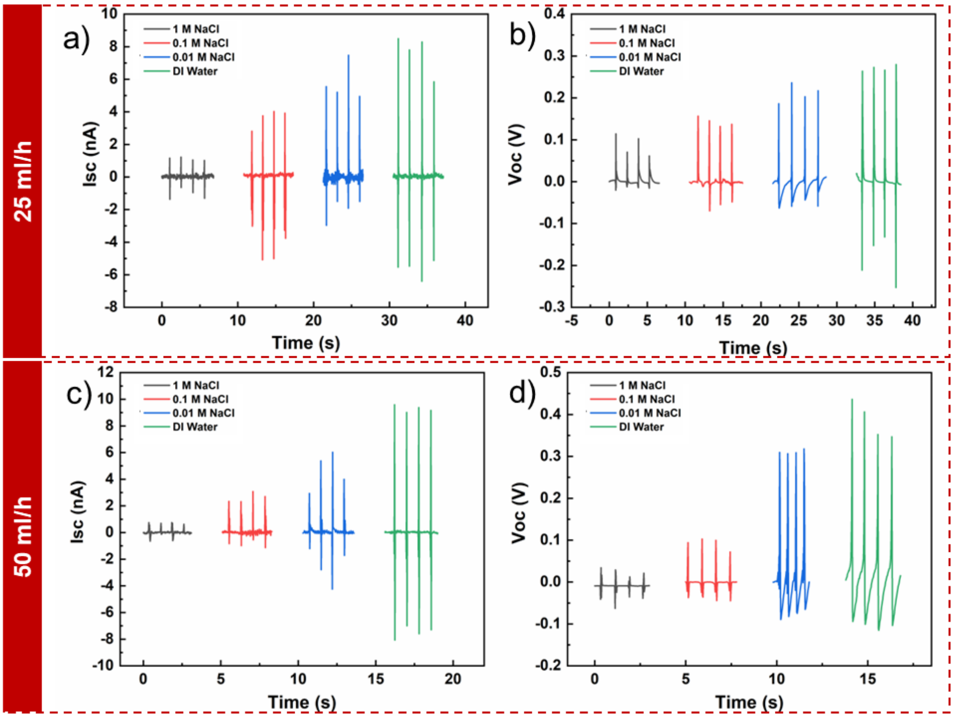

Figure 3.11 The chemical concentration sensing capabilities of the TENGs. a) Isc and b) Voc values obtained at a flow rate of 25 ml/h. c) Isc and d) Voc values obtained at a flow rate of 50 ml/h.

The TENG’s capability for sensing pH values and chemical concentrations were demonstrated. However, the electrical output was found to be limited, and TENG’s electrode structure was revised. A two-electrode setup was devised instead of the preexisting interdigitated electrode. Taking advantage of the Joule heating capability of an Ag NW network, a two-in-one device was designed. The device consisted of a sensor part at the top, and the large-area thin film heater part at the bottom side. A photograph of the finalized device is provided in Figure 3.12. The device could be applied to vehicle windshields and side mirrors as defrosting or defogging displays. The voltage generated through the droplets were measured through an Arduino chip and once the voltage baseline was surpassed, an external power supply started providing the current to generate heat in the transparent heater.

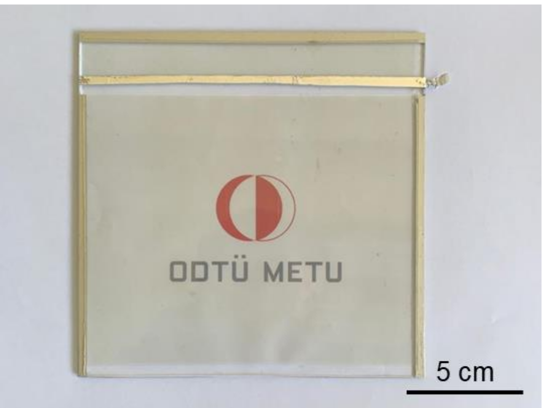

Figure 3.12 A photograph of the two-electrode TENG – thin film heater device.

The two-electrode setup generated electrical output differently compared to an interdigitated electrode setup. An illustration for the setup is given in Figure 3.13 (i-iv). The Ag NW network worked as the bottom electrode and a thin aluminum tape was used as the second electrode. Impinging droplets charged the PDMS layer negatively and the electrodes got charged positively. No current signal could be read from an impinging droplet. As it slide down, more of the PDMS surface was charged. Upon encountering the top Al electrode, the accumulated charge was transferred from the bottom electrode to the contact region between the droplet and PDMS (Figure 3.12 (iii)). As the droplet left the top electrode, charge returned to the bottom electrode.

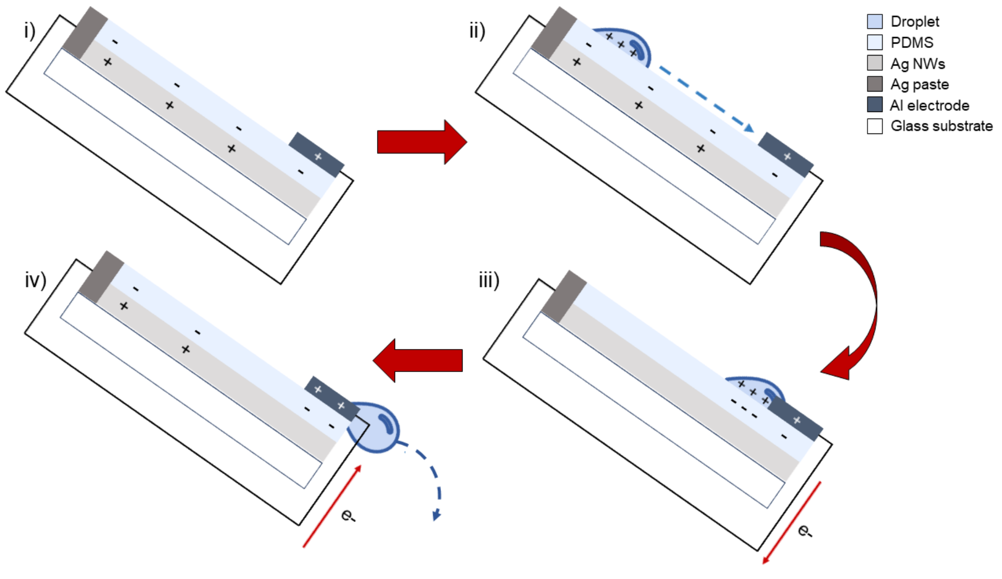

Figure 3.13 The working mechanism of the two-electrode TENG setup.

Positive Voc and Isc peaks were observed in this configuration with values significantly higher than that of the freestanding mode TENG. In addition, the measured Voc values were high enough to surpass the noise and voltage limit set by Arduino. The characteristics of the peaks coming from the two-electrode setup for Voc and Isc are shown in Figures 3.14 (a) and (b), respectively. Only positive peaks could be observed reaching peak Voc and Isc values of 5 V and 1.4 μA, respectively.

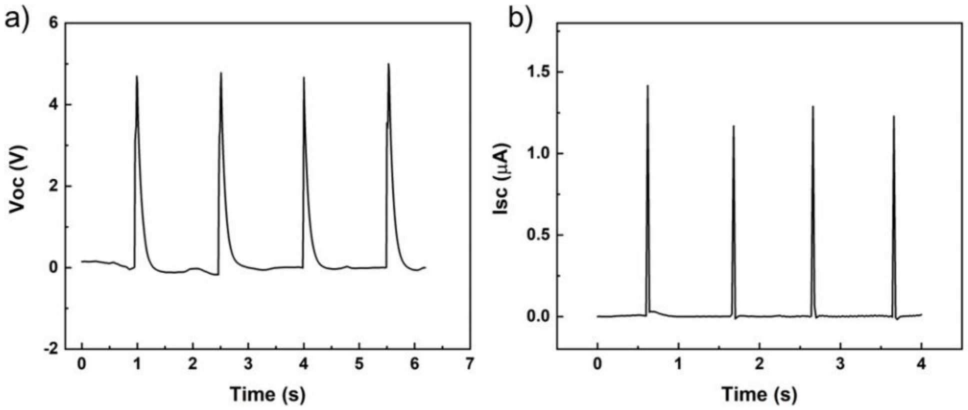

Figure 3.14 The Isc and b) the Voc outputs of the two-electrode TENG device.

The resulting high-voltage was used to control an Ag NW-based thin film heater activated by the droplet sensor. The device integrated the two with a two-electrode TENG droplet sensor at the top and an Ag NW thin film heater at the bottom side. The PDMS layer was encapsulating the entire surface of the device. In this direction, the sensor was used as a switch enabling a current through a MOSFET. This current provided Joule heating to power up the large-area Ag NW thin film heater. Figure 3.15 shows the test setup and the circuitry regarding the activation of the thin film heater. The droplet sensor was activated through droplets coming from a syringe. As droplets impinged on the PDMS, a signal on the Arduino interface could be observed in terms of a voltage value. When this voltage value surpassed the base limit, the MOSFET allowed current to pass through and the heater started working.

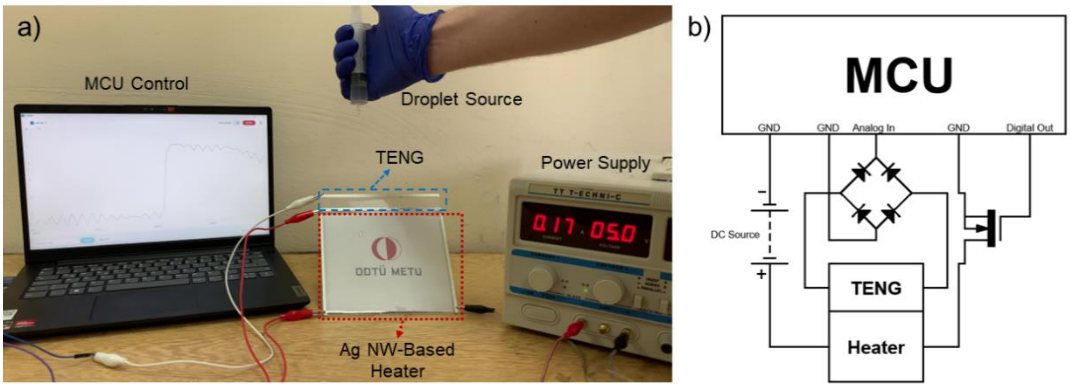

Figure 3.15 A photo of the integrated sensor and heater setup. b) Schematic circuit designed for heater activation.

Figures 3.16 (a-d) show thermal camera images at different instances during the sensor-activated heating process. The heater initially started with a slightly non-uniform distribution of temperature, yet with time, became more homogeneous. The darker streaks seen in the images displayed the water droplets sliding down. A temperature of 64°C could be reached at a bias of 30 V.

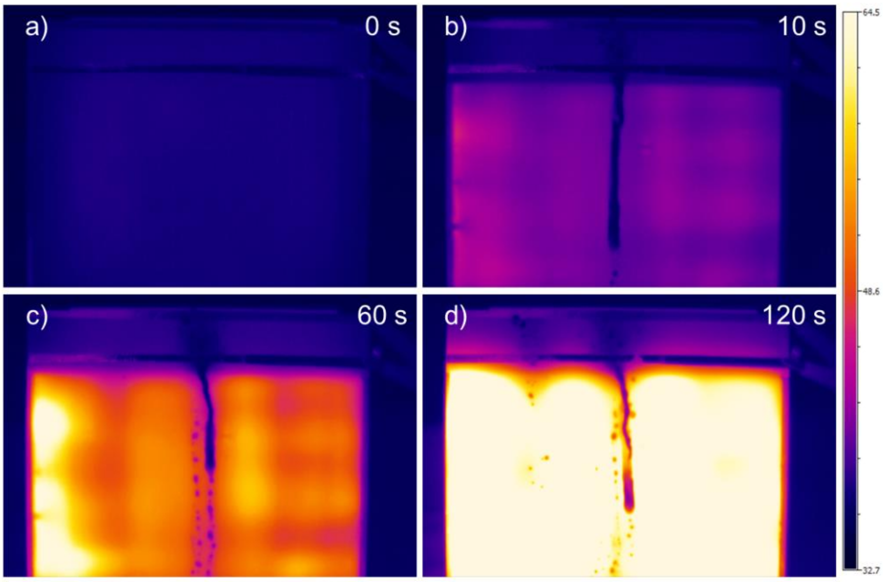

Figure 3.16 The thermal camera images of the sensor-activated Ag NW heater at various time intervals during heating.

CHAPTER 4

OPTIMIZED SILVER NANOWIRE NETWORKS FOR ELECTROCHROMIC DEVICES

4.1 Introduction

4.1.1 Electrochromic Devices

Electrochromism refers to the phenomenon wherein the optical properties of a material undergo reversible changes upon the application of an electric potential [120]. It has been used in everyday applications, such as smart windows for energy-saving buildings[121], automobile rearview mirrors[122], and low-power consumption displays[123]. The term electrochromism is often associated with an electrochromic device (ECD). Such devices have multiple layers, which typically are an electrochromic layer, an electrolyte, and an ion storage or a second electrochromic layer sandwiched between two transparent conductors constituting the working and counter electrodes. The structure of an ECD can be seen in Figure 4.1.

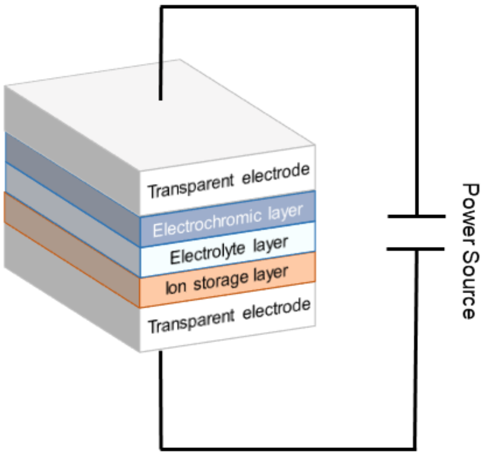

Figure 4.1 A schematic representation of the ECD constituents.

In an ECD, the transparent conductors provide the charge transfer through the device. The ion transfer throughout the ECD can be balanced with the electron transfer provided by the transparent conductors. Glass is common throughout many applications due to its convenience as a substrate. ITO[124] and FTO[125] are the main TCEs in ECDs. However, many alternative TCEs have been reported such as graphene[126], CNTs[127], and metallic nanowires[128] for devices with low cost or mechanical flexibility.

The electrolyte is situated at the center of the device and separates the electrochromic film and ion storage layer. It provides an interface between the two electrochromic layers and a media for ions to move within. High ionic conductivity, optical transmittance in the operating wavelength range, and electrical insulation are required for an electrolyte. Various liquids and salts are used for the preparation of transparent electrolytes. An electrolyte can be a liquid, gel-type, or solid state[129]. The most popular solvents are water and organic solvents, mainly propylene carbonate (PC). Once the salts are dissolved in the solvents, various polymers, such as polyethylene oxide or PMMA, are added to prepare a gel electrolyte[130]. Typically, dissolved ions in electrolytes are monovalent H^+, Li^+, Na^+, and K^+ though the use of multivalent ions such as Zn^{+2}, Ca^{+2}, and Al^{+3}, is also reported for the electrolyte [131]. The radii and valence of these ions affect the response and durability of the ECD.

The electrochromic layer consists of materials that change their color. For the electrochromic layer, different material classes, such as viologens[132], conjugated polymers[133], and transition metal oxides, are used in the literature. Viologens are polymeric materials with the chemical formula $(C_5H_4NR)_2^{n+}$ by convention. They are known for their fast switching times and cyclic durability. With two redox reactions, viologens can change colors twice. Conjugated polymers, mainly PEDOT:PSS[134], are conductive polymers with interesting optical properties. The conjugation of the polymers allows precise tuning of optical properties. Since this thesis focuses on transition metal oxide-based ECDs, the following discussion considers the transition metal oxides as electrochromic layers.

Among the transition metal oxide class, tungsten trioxide (WO_3)[135], nickel oxide[136] (NiO), vanadium pentoxide[137] (V_2O_5), and molybdenum trioxide[138] (MoO_3) are the most common materials that are used. The transition metal oxides can be utilized in primary and secondary electrochromic layers depending on whether they are cathodic or anodic. Figure 4.2 shows the transition metals primarily used as cathodic or anodic electrochromic layers.

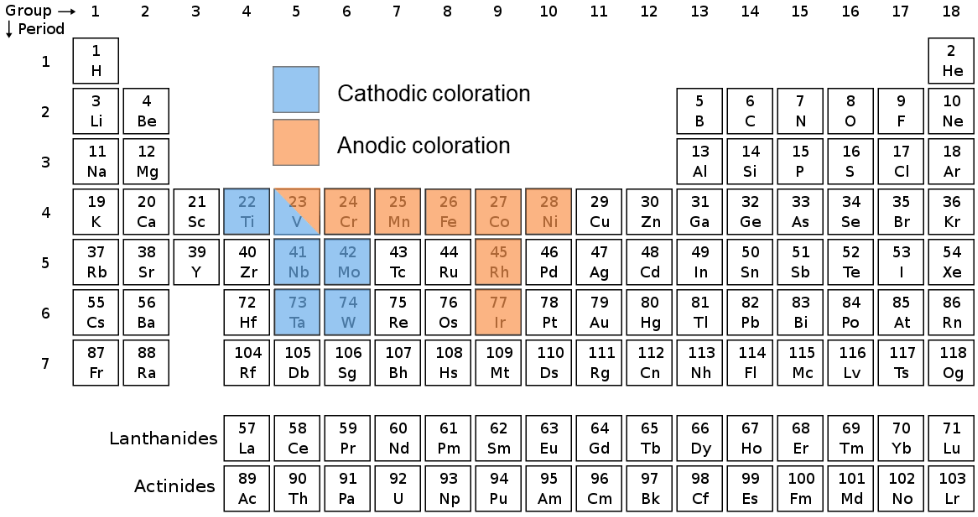

Figure 4.2 A periodic table with transition metal oxides highlighted based on their means of coloration.

WO_3 is the most studied electrochromic transition metal oxide. As a thin film, WO_3 has a pale-yellow color at the bleached state and a dark navy color at the colored state. In the bleached state, tungsten has a W^{+6} state and, by introducing cations into the structure, reaches the W^{+5} state. WO_3 is paired with NiO in multi-layered ECDs as a cation-anion pair[139]. NiO undergoes an anodic redox reaction where the Ni^{+2} state becomes Ni^{+1}. The reaction changes the film's color from a darker brown to a pale brown. The pair starts from a pale yellow and brown state for WO_3 and NiO, respectively. Through coloration, the constituents become dark navy and dark brown. The redox reaction regarding the change in a WO_3-NiO system with a Li-based electrolyte is given in Eq 4.1.

$$WO_3 + M_xNiO_{(1-y)} \rightarrow M_xWO_3 + NiO_{(1-y)} \qquad \text{Eq 4.1}$$

4.1.2 Performance Evaluation of Electrochromic Devices

Performance evaluation for an ECD is done through a few key aspects arising from the device characteristics. Namely, high optical modulation, low coloration time, high coloration efficiency, high long-term stability, and color retention are important for an ECD[131]. Optimizing these parameters allows the device to meet expectations and applications in smart windows and various other devices.

Optical modulation is the difference between the optical transmittance values in colored and bleached states (ΔT). Eq 4.1 shows the calculation of optical modulation, where T_b and T_c are the bleached and colored optical transmittance values, respectively.

$$\Delta T = T_b - T_c \qquad \text{Eq 4.1}$$

The contrast ratio (CR) can also be calculated through T_b and T_c. It is usually best quoted at the max wavelength for the colored state. A high CR is a desired property in ECDs[140].

$$CR = \frac{T_b}{T_c} \qquad \text{Eq 4.2}$$

The coloration time is defined as the time required to switch from the bleached state to the colored state or vice versa. Usually, the elapsed time from 0% to 90% color change is considered during coloration or bleaching, denoted as t_c and t_b, respectively. Many properties of the ECD, such as electrochromic film properties, the ionic conductivity of the electrolyte, the conductivity of the TCE, and the applied potential window, influence the coloration time. Having a fast response time is crucial for ECDs.

Coloration efficiency (CE) is often defined as the optical density change (ΔOD) at a specific wavelength upon being subjected to a charge per unit area (Q_D). Beer-Lambert Law is used to calculate the CE, and ΔOD can be replaced by the logarithm of CR, given in Eq 4.3.

$$CE(\lambda) = \frac{\Delta OD}{Q_D} = \frac{\log CR}{Q_D} \qquad \text{Eq 4.3}$$

Since CR is calculated at a specific wavelength, CE is also valid for the observation wavelength. Q_D is the charge density inserted into the system and has the units of C/cm^2.

The long-term performance of an ECD dictates its viability in practical applications and therefore is a crucial parameter. The cyclic stability of the ECD is measured in the amount of coloration and bleaching cycles the device can endure without appreciable loss in performance[141]. The redox capability of the electrochromic layer, device design, and the operating voltage window can also affect the cyclic stability.

The color retention ability of the ECD is another aspect of performance measurement[142]. It refers to the complete color change occurring in each on/off cycle. While the ECD performs well on the cyclic voltammetry tests, and the redox reactions' peaks are visible, the coloration or bleaching might not visually take place. Therefore, the extent of coloration is also measured along with cyclic stability.

4.2 Experimental Details

4.2.1 Preparation of Silver Nanowire Electrodes

The Ag NWs were synthesized and purified according to the procedures described in Chapter 2. Different sized soda-lime-silica glasses were used as substrates. 2.5 x 2.5 cm glasses were used for ECD applications, while 1.25 x 2.5 cm glasses were used for three-electrode measurements, and 0.8 x 5 cm glasses were prepared for

UV-Vis characterization inside the quartz cells. One side of each glass sample was lined with silver paste and used as the contacts. The deposition of Ag NWs to the glass substrates was performed as described in Chapter 2.

4.2.2 Synthesis of the Electrochromic Metal Oxide Nanoparticles

Three electrochromic metal oxide nanoparticles were used together in this work, namely tungsten trioxide (WO_3), tungsten peroxide hydrate (WO_x) as cathodic, and nickel oxide (NiO) as the anodic electrochromic materials. The synthesis of WO_3 and WO_x nanoparticles involved the use of hydrogen peroxide (H_2O_2, 35%, Sigma Aldrich) to oxidize W wire (Agar Scientific). In a typical synthesis, 1 g of the tungsten wire was cut into small segments and added into a glass bottle with 15.6 ml of hydrogen peroxide (H_2O_2). The beaker was placed onto a hot plate preheated to 100 °C and then stirred at 800 rpm for 5 hours. Once the solution was clear and the W wire was completely dissolved, the cap was opened, and the liquid was let to evaporate under a fume hood. The remaining hydrated orange powder was then collected. To achieve the monoclinic WO_3 phase and remove volatile compounds, the powder was annealed in a furnace at 450 °C for 2 hours. The resultant WO_3 nanoparticles were stored until further use.

To synthesize WO_x, excess H_2O_2 was introduced to the batch. 31.2 ml H_2O_2 was added to an capped bottle with 1 g W wire. The beaker was heated to 100 °C while being continuously stirred until all W wire was dissolved. Then, the bottle cap was opened and the liquid was allowed to evaporate under a fume hood at room temperature. The remaining white-pale yellow powder was used as WO_x.

NiO synthesis was conducted according to a previous work[143]. Simply, an aqueous solution of 0.1 M, 100 ml $Ni(NO_3)_2 \cdot 6H_2O$ was prepared. Then, a 0.1 M, 100 ml NaOH solution was slowly added to that solution. The two solutions were stirred at room temperature for 2 hours until the formation of precipitates. The precipitates were collected and centrifuged at 5000 rpm for 5 minutes and washed with deionized water and ethanol. The washed precipitates were collected and dried for 12 hours to eliminate all water. Finally, the obtained powder was annealed at 400 °C for 2 hours in a furnace.

4.2.3 Preparation of the Silver Nanowire Electrochromic Devices

Optimized Ag NW networks were used as the TCEs for the electrochromic devices. An ultrasonic spray coater (Sonotek ExactaCoat) was used to deposit the electrochromic metal oxides.

First, the deposition solutions were prepared. For the WO_3 and WO_x solutions, 0.3 g of the synthesized powders were added to a capped bottle with 15 ml each of deionized water and isopropyl alcohol. The solution was placed in an ultrasonic bath for 6 hours in 2-hour intervals to keep the water temperature as cool as possible. Between the intervals, the water in the ultrasonic bath was refreshed with cold water. The bottle was cooled to room temperature before the other 2-hour interval. After sonication, the solution was stirred overnight.

The NiO coating solution was prepared by mixing 0.1 g NiO powder and 30 ml ethanol overnight.

For the deposition of WO_3 and WO_x, the prepared Ag NW TCEs were placed onto a hot plate heated to 150 °C. The air pressure and atomizer power were set at 3 kPa and 4 W, respectively. The solution flow rate, nozzle distance, and cycle amount were investigated to achieve a homogeneous coating of the nanoparticles.

The deposition of NiO using ultrasonic spray deposition was adapted from a previous work. Same air pressure and atomizer power values were used with the WO_3 and WO_x powders. The solution flow rate was 0.2 ml/min, nozzle distance was 4 cm, and 20 deposition cycles were utilized.

A 1 M lithium perchlorate ($LiClO_4$) in propylene carbonate (PC) was used as the electrolyte. Upon full dissolution of $LiClO_4$/PC, PMMA dissolved in acetonitrile was added. As acetonitrile was evaporated, a viscous gel was obtained, which was then dropped by a pipette and spread carefully between the WO_3/Ag NW and NiO/Ag NW electrodes for further experiments.

4.3 Characterization

4.3.1 Scanning Electron Microscopy (SEM) Analysis

The SEM images of the synthesized nanoparticles were obtained to analyze the particle size and morphology. The homogeneity of ultrasonic spray-coated nanoparticles was also examined. FEI NOVA NANO SEM 430 was used at an operating voltage of 20 kV. SEM images were taken from glass and silicon wafers. A very thin layer of gold coating was applied to glass samples. The deposition uniformity and nanoparticle sizes were considered. Deposition parameters were adjusted accordingly.

4.3.2 X-Ray Diffraction (XRD) Analysis

The crystal structure of the obtained powders was determined through XRD analysis using Rigaku D/MAX 2200 ULTIMA/PC. Cu Kα radiation (wavelength of 1.5406 Å) was utilized.

4.3.3 Electrochemical Measurements

For the electrochemical characterization of the ECDs, a Biologic (VMP3) workstation was utilized. Cyclic voltammetry (CV) analyses were conducted in a three-electrode setup for determining the electrochromic performance of WO_3/Ag NW electrodes and in a two-electrode setup for ECDs. In the three-electrode setup, WO_3/Ag NW electrode was used as the working electrode (WE), a silver wire was used as the reference electrode (RE), and a platinum wire was used as the counter electrode (CE). A voltage range of -0.8 – 0.3 V was used. In ECD measurements, the WO_3/Ag NW electrode was the WE, and NiO/Ag NW, NiO/FTO, and bare FTO electrodes were used as CE. For the coloring/bleaching cyclic tests of the ECDs, chronoamperometry (CA) measurements were made between -1.0 V and 0.3 V.

4.3.4 Optical Transmittance Analysis

The optical transmittance measurements were performed using Shimadzu 3600 UV-Vis-NIR spectrophotometer equipped with an integrated sphere. The overall transmittance of each sample was assessed within the wavelength range of 300 to 1400 nm. The colored and bleached transmittance values were determined. At the highest transmittance difference, coloration efficiency of the ECDs was analyzed during CA measurements.

4.3.5 Thin Film Thickness Measurements

The thickness of WO_x thin films were measured using the Woollam M2000V spectroscopic ellipsometer. Angles of 60, 65, and 70° were used for precise fitting during data acquisition.

4.4 Results and Discussion

Through the synthesis of WO_3 nanoparticles, an orange-yellow powder as a hydrated tungstic acid was obtained. The physically and chemically bonded water needed to be evaporated through an annealing process. In the literature, a monoclinic WO_3 was reported to be obtained at annealing temperatures above 425 °C and below 500 °C. The reported annealing times were over an hour. Therefore, the obtained powders were annealed at 450 °C for 1, 2, and 4 hours. The change in the powder’s color indicated successful synthesis of WO_3, as evidenced by a pale yellow-green color. Annealing for 1 hour resulted in a mixed-phase powder, with some of the material in the crucible failing to transform into WO_3. The color of the resultant powder was different in different parts, necessitating a longer annealing time. Annealing for 2 hours proved successful, as all the powder had a pale yellow-green color. To monitor the evolution of microstructure and crystal structure, XRD and SEM analyses were conducted from both 2-hour and 4-hour annealed samples, results of which are provided in Figures 4.3 (a-c). The same crystal structure was observed for both 2-hour and 4-hour annealed powders, as can be seen in Figure 4.3 (a). The peaks match with JCPDS Card No: 43-1035 well. The major peaks correspond to (002), (020), (200), (120), (-112), and (202) planes at peak positions of 23.06, 23.65, 24.27, 26.64, 28.75, and 34.12°, respectively. SEM images provided in Figures 4.3 (b) and (c) show the 4- and 2-hour annealed nanoparticles, respectively. With increasing annealing time, the fusion of nanoparticles was observed. The particles aggregate and increase in size, as can be seen in Figure 4.3 (b), and are considerably larger than those in Figure 4.3 (c). Therefore, 2-hour annealed nanoparticles are preferred in electrochromic applications.

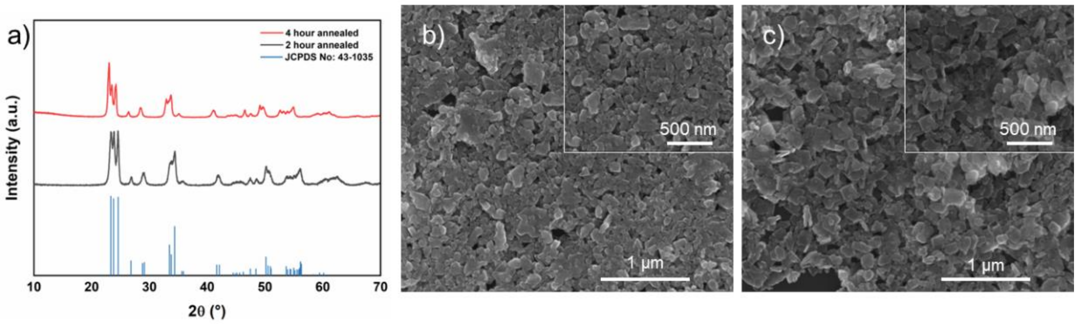

Figure 4.3 a) XRD pattern of 4 and 2-hour annealed WO_3 powder. SEM images of b) 4-hour and c) 2 hour annealed WO_3 powder.

For WO_x nanoparticles, the powder obtained through the first part of the synthesis was characterized. The results of XRD and SEM analyses are provided in Figures 4.4 (a) and (b), respectively. The XRD pattern matched well with JCPDS Card No: 050-0234 and the powder was identified as tungsten peroxide hydrate. The primary peaks correspond to (20-1), (200), (20-2), and (111) planes in 14.48, 16.12, 18.84, 19.74, and 27.73°, respectively. The SEM image in Figure 4.4 (b) shows small features with no specific nanoparticle formation observed. This was found to be a characteristic of the acidic metal salts since they dissolve in the solution rather than being dispersed.

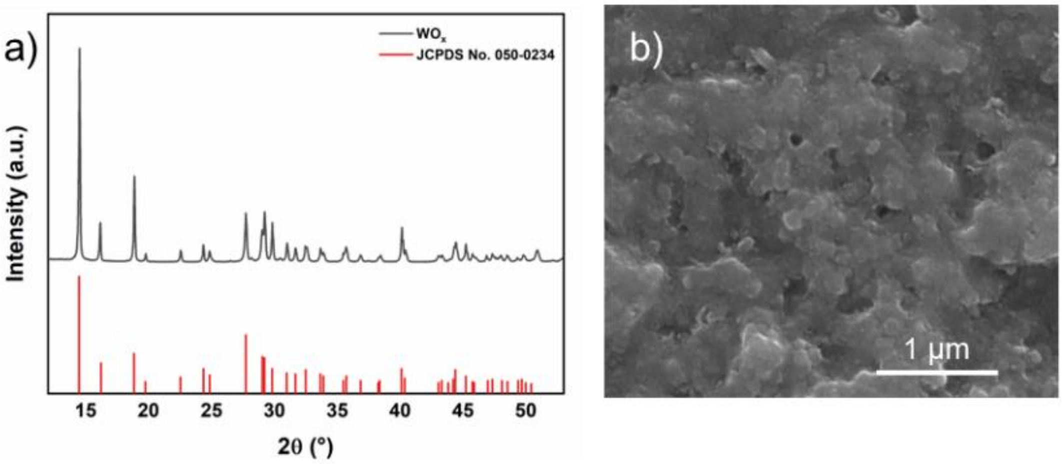

Figure 4.4 a) the XRD pattern and b) the SEM image of WO$_x$ powders.

The chemical and visual characterization of the NiO powder, and the NiO films can be found in the Appendix.

Following the characterization of the obtained powders, their coating onto Ag NWs was practiced by ultrasonic spray deposition. Basic spray parameters were adapted from previous studies and precise values were obtained by a parametric study. The SEM images from coatings of WO$_3$ nanoparticles are provided in Figures 4.5 (a), (b), and (c) for samples 1, 2, and 3, respectively. The coating thickness and uniformity were controlled through the number of cycles. It was seen that the nanoparticles could effectively coat the entire surface upon applying more than 20 coating cycles. 8 and 12 cycles of coating provided subpar coverage of the Ag NW network. Therefore, the deposition amount was set as 20 cycles for the initial electrochemical three-electrode tests.

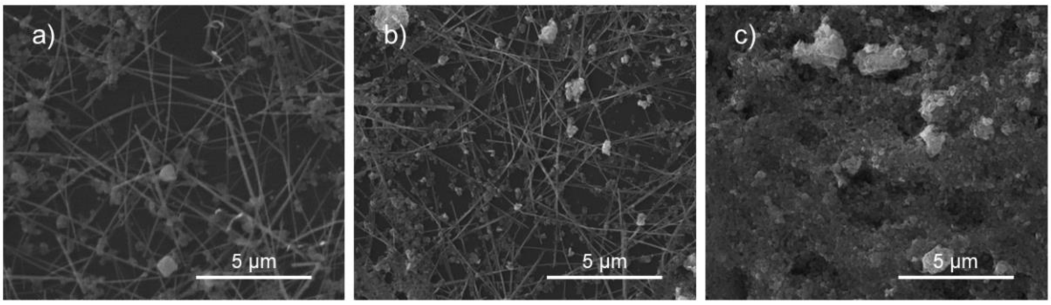

Figure 4.5 Ultrasonic spray deposition of a) 8, b) 12, and c) 20 cycles of WO_3 nanoparticles.

For the WO_x deposition, Table 4.1 shows the deposition parameters 1 through 4. The flow rate, nozzle height, and number of deposition cycles were analyzed. The solution concentration, hot plate temperature, air pressure, and power were kept constant. Similar to the SEM samples, parameters 1, 2, 3, and 4 showed a lack of crystalline nanoparticles. Some areas on the samples had an excess amount of WO_x, which could be seen especially in Figures 4.6 (a) and (b). Parameters 3 and 4 allowed deposition of a thin layer of coating with visible Ag NWs shown in Figures 4.6 (c) and (d). The thicknesses of the films were measured using spectroscopic ellipsometry. Parameters 1, 2, and 3 resulted in the film with higher thicknesses compared to that of parameter 4 which had a thickness of 128 ± 10 nm.

Table 4.1 Ultrasonic spray deposition parameters.

Parameter No:	*Flow Rate (ml/min)*	*Nozzle Distance (cm)*	*Number of Cycles*	*Film Thickness (nm)*
1	0.1	6.5	40	173
2	0.2	6.5	20	194
3	0.3	6.5	20	214
4	0.05	5	20	128

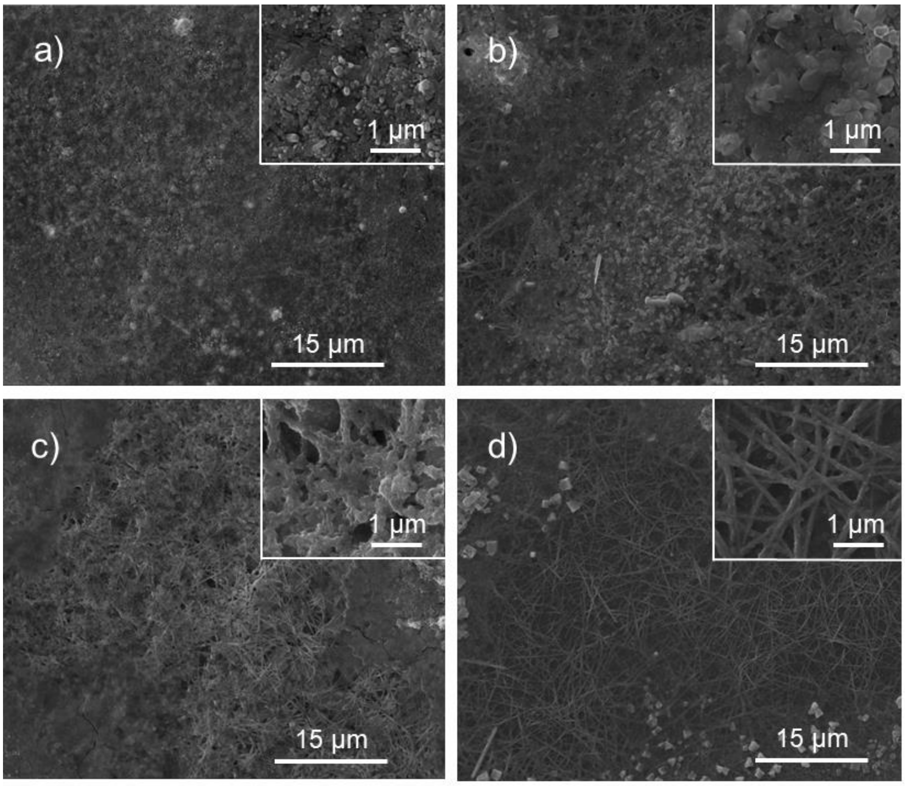

Figure 4.6 Ultrasonic spray deposition of WO_x nanoparticles onto Ag NWs using parameters of a) 1, b) 2, c) 3, and d) 4.

Later, the 20 cycle deposited WO_3/Ag NW electrodes were placed in a three-electrode setup as the working electrode with an Ag wire as the reference electrode and a Pt wire as the counter electrode. The CV curve and photos showing the coloration of the electrode is shown in Figure 4.7. The peaks appearing on the CV curves were typical to that of WO_3 electrodes[144], and the inset photographs showed the weak coloration of the WO_3/Ag NW electrodes. The electrodes showed some degree of coloration but a complete bleaching was not observed. This was attributed to the crystalline nature of WO_3 nanoparticles. The plate-like structure of WO_3 did not allow enough Li^+ ions to pass through for intercalation to take place. Therefore, the use of WO_3 nanoparticles were discontinued and instead, WO_x nanoparticles were utilized in the further experiments.

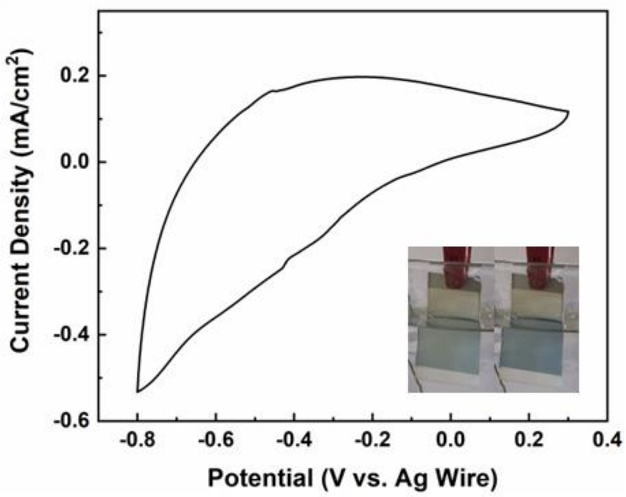

Figure 4.7 The CV curve of WO_3/Ag NW electrode with inset photographs of the colored/bleached states.

Then, WO_x/Ag NW electrodes were placed in a three-electrode setup using the four deposition parameters provided in Table 4.1. The results and photos of colored and bleached forms of the electrodes are provided in Figures 4.8 (a-d). Optically, Parameters 2 and 3 exhibited inferior performance in comparison to Parameters 1 and 4. The samples' bleaching performance did not meet expectations. This was attributed to the thickness of the films. Since parameter 1 resulted in the deposition of a comparably thicker WO_x film of 173 nm thickness, parameter 4 was selected to be used further in ECDs.

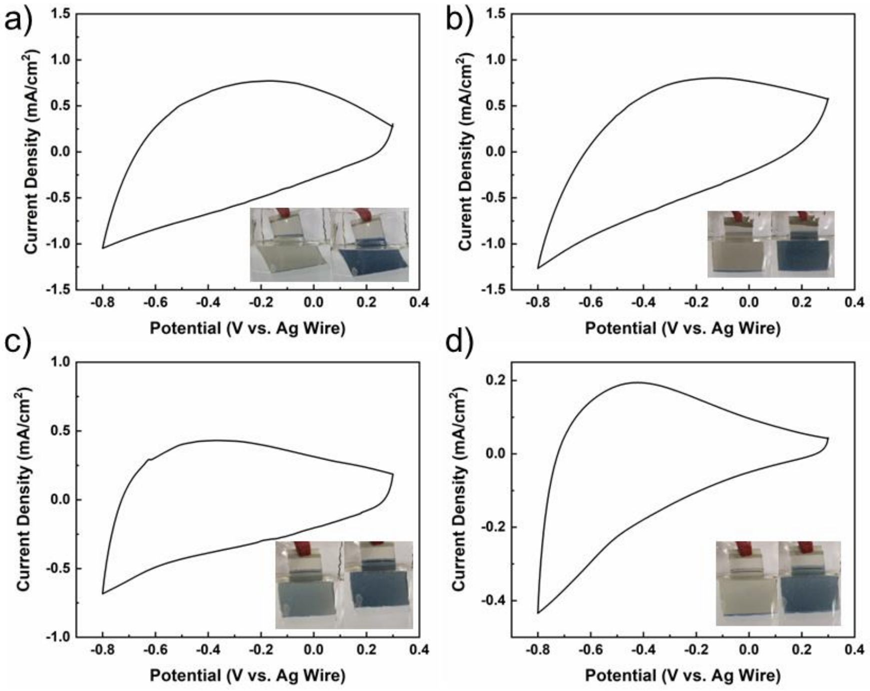

Figure 4.8 The CV curves and corresponding colored/bleached state photographs for deposition parameters a) 1, b) 2, c) 3, and d) 4.

To visualize the effectiveness of the optimized Ag NW network electrodes for electrochromics, WO_x was deposited onto an untreated Ag NW network. The untreated Ag NW network had a sheet resistance of 61 Ω/sq. The three-electrode CV performance of the film is displayed in Figure 4.9. The inset photographs show the coloration performance of the electrodes. A lower current density was observed due to the higher resistance provided by the Ag NWs, compared to that of the treated and optimized electrodes. Since the amount of charge transferred to the WO_x film was not sufficient due to the higher sheet resistance, the coloration performance of the films did not meet that of the electrodes using post-treated Ag NW networks.

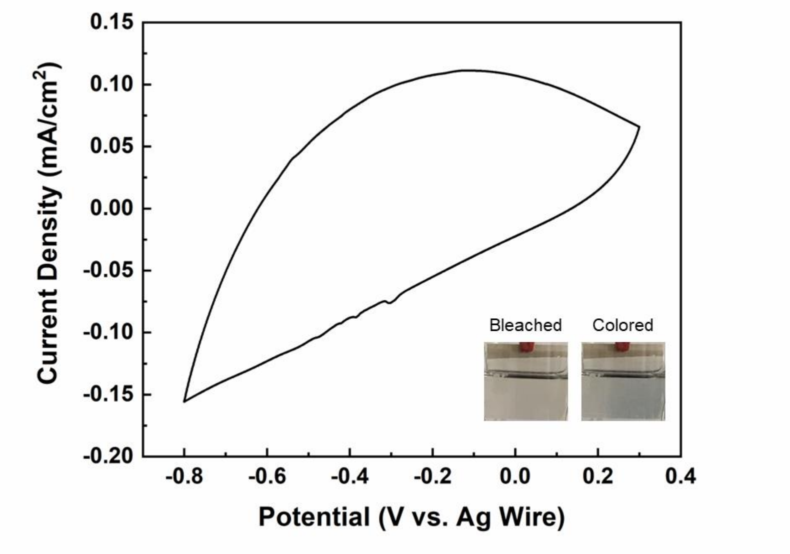

Figure 4.9 The CV curve of the WO_x electrochromic film using an untreated Ag NW network as the transparent conductor.

Using parameter 4, ECDs were prepared with NiO/Ag NW counter electrode. However, the ECDs did not work as intended, mainly due to the oxidation of Ag NWs when used as anode. The continuous charge carrier exchange process resulted in the degradation of the Ag NW network[145]. The SEM images of the degraded electrodes are provided in Appendix A. Therefore, FTO electrodes were used to compensate for the electrochemical shortcomings of the Ag NW network as the anode. ECDs were then characterized through chronoamperometry and UV-Vis spectroscopy. The optical transmittance spectra of the colored and bleached states of the ECD were measured to calculate the contrast ratio and ΔT of the device. The results are provided in Figure 4.10. Herein, the baseline was taken as the bare Ag NW electrode, therefore only the WO_x layer's coloration was considered. Consequently, the ΔT was found to be 28.3, 53.9, and 81.3% at wavelengths of 550, 650, and 1000 nm, respectively. The contrast ratios were 1.63, 3.01, and 9.2 for the mentioned wavelengths, respectively. Many works have reported the optoelectronic properties of tungsten oxide-based films at a wavelength of 650 nm [146]. Consequently, this work considered 650 nm as the baseline for optical transmittance.

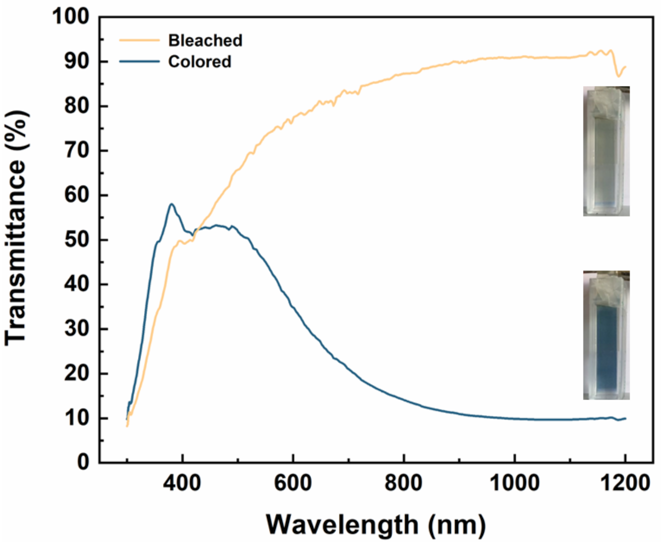

Figure 4.10 The optical transmittance spectra of the colored and bleached state of WO_x/Ag NW electrodes.

The coloration time of the device was investigated, where 40-second-long coloration and bleaching cycles were applied from -3 V to 1.8 V. 650 nm was taken as the wavelength of the contrast ratio, and the baseline was taken from air. Therefore, the transmittance belongs to the entire ECD. Coloration and bleaching times were found as 22 and 15 seconds, respectively (Figure 4.11 (a)). These results were quite high compared to the numbers achieved in the literature using tungsten-based materials. The coloration efficiency was calculated through combining the current density and optical transmittance values obtained from the ECD, given in Figure 4.11 (b). The achieved coloration efficiency of 142.3 cm^2/C is highly promising, proving that the fabricated device is power- efficient during coloration and bleaching[147]. Figure 4.11 (c) shows the current density and transmittance characteristics of the ECD during the chronoamperometry and kinetic optical transmittance measurements.

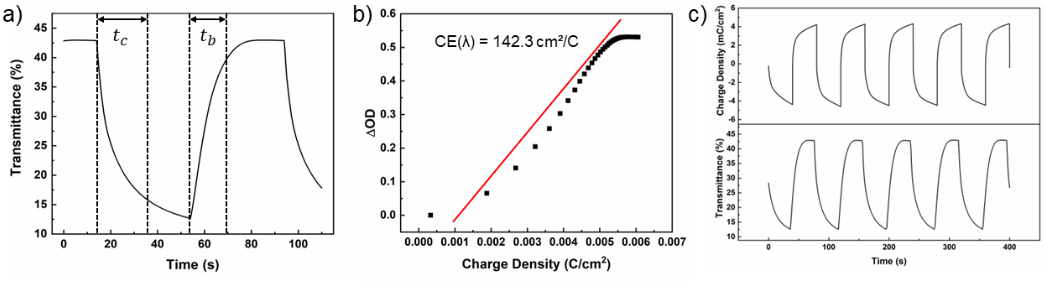

Figure 4.11 a) The coloration and bleaching times, b) the coloration efficiency, and c) the chronoamperometry and kinetic optical transmittance measurements at a wavelength of 650 nm.

Table 4.2 presents a comparison between the ECDs documented in existing literature and the findings presented in this thesis. The change in optical transmittance (ΔT), coloration (t_c) and bleaching (t_b) times, and coloration efficiency (CE) were the focal points of comparison. It was found that the coloration efficiency of the ECD achieved in this work rivals that of the highest performing ECDs in the literature. Despite the promising CE, the coloration and bleaching times failed to meet the standards set by previous works.

Table 4.2 A comparison of tungsten-oxide based ECDs using Ag NW electrodes as TCEs.

Type of Electrode	*Deposition Method*	*ΔT (%)*	*t_c (s)*	*t_b (s)*	*CE (cm²/C)*	*Ref.*
WO_3/Ag NWs	Electro-deposition	76.03	12	2	45.3	Park et al.[148]
WO_3/Ag NWs	Sol-gel	40	31.72	9.58	34.8	Au et al.[149]
WO_3/Ag NWs	Thermal evaporation	44.1	1.7	1	80.2	Shen et al.[150]
$W_{18}O_{49}$/Ag NWs	Spray coating	53.8	7.1	4.3	45.95	Zheng et al.[151]
WO_x/Ag NWs	Spray coating	53.9	22	15	142.3	This work

CHAPTER 5

CONCLUSIONS AND FUTURE RECOMMENDATIONS

5.1 Conclusions

In this thesis, the focus was on studying the enhancement of optoelectronic properties in Ag NW networks through post-treatment optimization. Since Ag NWs used in the literature have various different properties such as length, thickness, PVP thickness, and deposition method, the effectiveness of the reported treatments on different nanowires was unknown. Hence, a parametric study of various post-treatment methods was conducted on Ag NW networks to determine the most suitable treatment approach.

In Chapter 2, a single batch of synthesized Ag NWs were deposited on glass substrates through spray coating. Each sample was standardized to have a sheet resistance and optical transmittance of 50 Ω/sq and 90%, respectively. For the sake of convenience and scalability, predominantly solution-based post-treatments were employed. A comprehensive literature survey was conducted to explore facile and effective post-treatment approaches, and several methods were developed in-house. Heat treatment, AA solder, electroless welding, $NaBH_4$ cleaning, HNO_3-Ag welding, hot water treatment, and halide welding were applied on the Ag NW networks. It was found that $NaBH_4$ cleaning was able to remove the PVP layers around the nanowires and reduce the junction resistance, and HNO_3-Ag treatment was capable of welding the junctions effectively without hindering the optical transmittance. Since the two treatment methods had different aims, the combination of the two proved to be effective in removing the capping agent and welding the Ag NWs. The optimized treatment enabled the attainment of FoM values surpassing 300.

In Chapter 3, the optimized Ag NW network was utilized in a transparent liquid-solid interface TENG as the current collector. The Ag NWs were spin-coated with PDMS to provide a negatively charged triboelectric layer. The incident water droplets provided the liquid-solid interface and acted as the positive triboelectric layer. The contact electrification induced between PDMS and the water droplets created the electrical output. The obtained transparent TENG was found to be pH and chemical concentration sensitive. In comparison, the TENG using an untreated Ag NW network provided a slightly lower signal magnitude. In addition, a large-area device was fabricated combining the sensing ability of the TENG and the Joule heating ability of Ag NWs. The droplet sensor activated the power supply, which provided the necessary current to power up the transparent heater.

Chapter 3 focuses on the use of Ag NW networks in ECDs as transparent conductors. WO_3, WO_x, and NiO nanoparticles were synthesized to serve as the electrochromic layers. The nanoparticles were then prepared as inks to be deposited onto Ag NW networks by ultrasonic spray deposition. The resultant electrodes were first characterized in a three-electrode setup. The WO_3/Ag NW electrodes did not display a complete coloration or bleaching, whereas the WO_x/Ag NW electrodes had a full coloration and bleaching. The WO_x/Ag NW electrodes using an untreated Ag NW network had a coloration performance below that of the post-treated ones, therefore, a fully treated Ag NW network was necessary to ensure a high performanc ECD. Then, ECDs were prepared with WO_x/Ag NW on the cathodic side and NiO/Ag NW or FTO on the anodic side. The coloration efficiency of the devices were measured as 143.2 cm^2/C. The achieved coloration efficiency was quite high, whereas the coloration and bleaching times did not meet expectations.

5.2 Future Recommendations

In this thesis, strategies for improving the optoelectronic performance of Ag NW networks were investigated. Post-treatment methods were applied to the same Ag NW batch to eliminate variance in nanowire characteristics. Different post-treatment methods were analyzed and compared in terms of effectiveness. The reduction in sheet resistance and the change in optical transmittance was monitored.

In the first part of the thesis, it is documented that different post-treatment modalities are viable, but some important shortcomings prevent them from being the most effective. More work can be done on the scalability of treatments to make them feasible. In addition, Ag NWs were deposited using a hand-controlled spray coater. Although the Ag NWs used are the same, human involvement in the process led to some unwanted discrepancies. Therefore, it will be better to use an automized spray coating process or the use of more precise methods such as slot-die coating could remove any doubt about the nanowire deposition. These deposition processes are applicable to many flexible substrates as well. By doing post-deposition treatments, Ag NWs' optoelectronic properties can be pushed closer to 100% optical transmittance and 0 Ω/sq values. Therefore, high-performance flexible photovoltaics, screens and OLEDs could be designed exploiting the shortcomings of ITO and moving further with innovation.

In the second part, transparent liquid-solid interface TENGs were prepared using Ag NWs as the current collector layer. Herein, PDMS was used as the tribonegative layer and water droplets constituted the tribopositive layer. In this case, the generated electrical output was on the lower end, not enough to light up LEDs or power up digital watches as usually displayed in the literature. This can be reduced to two main reasons. Firstly, PDMS is not documented to be the most negative polymer in TENG studies. PTFE and FEP are more negatively charged, and can be used to coat the Ag NWs as the tribonegative layer. The second reason is the electrode setup, as the heater activation mechanism displayed, the two-electrode system provided better results, and the sensor could provide a higher electrical output. More work on this setup can be made using Ag NWs as the current collector. In addition, there is the case of sticky charges on the electrode surface. A universal method to fully neutralize the surface of the TENG must be developed and studied. As for the heater device, large-area manual deposition of Ag NWs can lead to inconsistencies. The temperature distribution on the device's surface is less than ideal, exhibiting inhomogeneous heating in certain areas. Resolving this issue, the setup is could be implemented in vehicle windshields and side mirrors as defrosting or defogging glasses. In addition, the substrates can be shaped according to the incident water droplets and their flow, showcasing a primary advantage of Ag NWs over ITO. The use of a transparent flexible electrode could maximize the energy harvesting potential of water droplets.

Since the liquid-solid interface TENG devices have sensitivity for ions dissolved in the contacting solvent, the response coming from charged organic molecules, such as surfactants, could be investigated. The capability of the device to identify signals coming from organic or weak acids could also be studied.

In the third pard, ECDs were developed using Ag NWs as the transparent conductor layer. WO_3 coated devices performed relatively poorly, and the initial optical transmittance of WO_x-coated devices was low. To attain a higher optical contrast, a more comprehensive parametric study for the nanoparticle coating could be conducted. The coloration time was found to be quite long. Therefore, a study focused on reducing the coloration time is necessary, and one possible approach is to decrease the thickness while maintaining the coating's uniformity.

Furthermore, the prepared ECDs did not function optimally due to difficulties faced by the NiO/Ag NW electrode in withstanding the positive voltage bias. FTO and NiO/FTO devices had much more success as a counter electrode to WO_x/Ag NW. Therefore, the protection of Ag NWs on the anodic electrode can be investigated. Some promising materials that could protect Ag NWs while not hindering the optical transmittance of the networks can be employed. These materials might include ALD-deposited metal oxides and 2D materials such as graphene, reduced graphene oxide (rGO), and MXene.

Further, a flexible substrate such as polyethylene terephthalate (PET), polydimethylsiloxane (PDMS), or polyvinyl chloride (PVC) can be utilized, which would allow realization of flexible electrochromic displays with Ag NW electrodes.

REFERENCES

(1) Bädeker, K. Über Die Elektrische Leitfähigkeit Und Die Thermoelektrische Kraft Einiger Schwermetallverbindungen. *Ann Phys* **1907**, *327* (4), 749–766. https://doi.org/10.1002/ANDP.19073270409.

(2) Maurya, S. K.; Galvan, H. R.; Gautam, G.; Xu, X. Recent Progress in Transparent Conductive Materials for Photovoltaics. *Energies 2022, Vol. 15, Page 8698* **2022**, *15* (22), 8698. https://doi.org/10.3390/EN15228698.

(3) Lei, T.; Peng, R.; Song, W.; Hong, L.; Huang, J.; Fei, N.; Ge, Z. Bendable and Foldable Flexible Organic Solar Cells Based on Ag Nanowire Films with 10.30% Efficiency. *J Mater Chem A Mater* **2019**, *7* (8), 3737–3744. https://doi.org/10.1039/C8TA11293B.

(4) Yu, S.; Liu, X.; Yang, P.; Zhao, L.; Dong, H.; Wu, C.; Li, X.; Xiong, J. Highly Stable Silver Nanowire Networks with Tin Oxide Shells for Freestanding Transparent Conductive Nanomembranes through All-solution Processes. *Chemical Engineering Journal* **2022**, *446*, 137481. https://doi.org/10.1016/J.CEJ.2022.137481.

(5) Hao, T.; Wang, S.; Xu, H.; Zhang, X.; Magdassi, S.; Pan, L.; Song, Y.; Li, Y.; Zhao, J. Novel Transparent TiO2/AgNW-Si(NH2)/PET Hybrid Films for Flexible Smart Windows. *ACS Appl Mater Interfaces* **2022**. https://doi.org/10.1021/ACSAMI.1C25002/SUPPL_FILE/AM1C25002_SI_001.PDF.

(6) Sheng, S.-Z.; Wang, J.-L.; Zhao, B.; He, Z.; Feng, X.-F.; Shang, Q.-G.; Chen, C.; Pei, G.; Zhou, J.; Liu, J.-W.; Yu, S.-H. Nanowire-Based Smart Windows Combining Electro- and Thermochromics for Dynamic Regulation of Solar Radiation. *Nature Communications 2023 14:1* **2023**, *14* (1), 1–9. https://doi.org/10.1038/s41467-023-38353-4.

(7) Wang, P.; Jian, M.; Wu, M.; Zhang, C.; Zhou, C.; Ling, X.; Zhang, J.; Yang, L. Highly Sandwich-Structured Silver Nanowire Hybrid Transparent Conductive Films for Flexible Transparent Heater Applications. *Compos Part A Appl Sci Manuf* **2022**, *159*, 106998. https://doi.org/10.1016/J.COMPOSITESA.2022.106998.

(8) Shin, H.; Sharma, B. K.; Lee, S. W.; Lee, J. B.; Choi, M.; Hu, L.; Park, C.; Choi, J. H.; Kim, T. W.; Ahn, J. H. Stretchable Electroluminescent Display Enabled by Graphene-Based Hybrid Electrode. *ACS Appl Mater Interfaces* **2019**, *11* (15), 14222–14228. https://doi.org/10.1021/ACSAMI.8B22135/ASSET/IMAGES/LARGE/AM-2018-22135P_0005.JPEG.

(9) Qian, G.; Lin, Y.; Wantz, G.; Davis, A. R.; Carter, K. R.; Watkins, J. J. Saturated and Multi-Colored Electroluminescence from Quantum Dots Based Light Emitting Electrochemical Cells. *Adv Funct Mater* **2014**, *24* (28), 4484–4490. https://doi.org/10.1002/ADFM.201400167.

(10) Kim, H.; Seo, M.; Kim, J.-W.; Kwon, D.-K.; Choi, S.-E.; Woong Kim, J.; Myoung, J.-M.; Kim, H.; Kim, J.; Kwon, D.; Myoung, J.; Seo, M.; Choi, S.; Kim, J. W. Highly Stretchable and Wearable Thermotherapy Pad with Micropatterned Thermochromic Display Based on Ag Nanowire–Single-Walled Carbon Nanotube Composite. *Adv Funct Mater* **2019**, *29* (24), 1901061. https://doi.org/10.1002/ADFM.201901061.

(11) Papanastasiou, D. T.; Schultheiss, A.; Muñoz-Rojas, D.; Celle, C.; Carella, A.; Simonato, J. P.; Bellet, D. Transparent Heaters: A Review. *Adv Funct Mater* **2020**, *30* (21). https://doi.org/10.1002/ADFM.201910225.

(12) Fu, Y.; Liang, F.; Tian, H.; Hu, J. Nonenzymatic Glucose Sensor Based on ITO Electrode Modified with Gold Nanoparticles by Ion Implantation. *Electrochim Acta* **2014**, *120*, 314–318. https://doi.org/10.1016/J.ELECTACTA.2013.12.082.

(13) Gui, Y.; Miscuglio, M.; Ma, Z.; Tahersima, M. H.; Sun, S.; Amin, R.; Dalir, H.; Sorger, V. J. Towards Integrated Metatronics: A Holistic Approach on Precise Optical and Electrical Properties of Indium Tin Oxide. *Scientific Reports 2019 9:1* **2019**, *9* (1), 1–10. https://doi.org/10.1038/s41598-019-47631-5.

(14) Bok, S.; Seok, H. J.; Kim, Y. A.; Park, J. H.; Kim, J.; Kang, J.; Kim, H. K.; Lim, B. Transparent Molecular Adhesive Enabling Mechanically Stable ITO Thin Films. *ACS Appl Mater Interfaces* **2021**, *13* (2), 3463–3470. https://doi.org/10.1021/ACSAMI.0C20582/ASSET/IMAGES/MEDIUM/AM0C20582_M002.GIF.

(15) Chen, Z.; Li, W.; Li, R.; Zhang, Y.; Xu, G.; Cheng, H. Fabrication of Highly Transparent and Conductive Indium-Tin Oxide Thin Films with a High Figure of Merit via Solution Processing. *Langmuir* **2013**, *29* (45), 13836–13842. https://doi.org/10.1021/LA4033282/SUPPL_FILE/LA4033282_SI_001.PDF.

(16) Ellmer, K. Past Achievements and Future Challenges in the Development of Optically Transparent Electrodes. *Nature Photonics 2012 6:12* **2012**, *6* (12), 809–817. https://doi.org/10.1038/nphoton.2012.282.

(17) Klein, E.; Huber, K.; Paul, O.; Ruther, P. Low-Temperature Plasma Annealing of Sputtered Indium Tin Oxide for Transparent and Conductive Thin-Films on Glass and Polymer Substrates. *Thin Solid Films* **2020**, *693*, 137715. https://doi.org/10.1016/J.TSF.2019.137715.

(18) Nam, E.; Kang, Y. H.; Son, D. J.; Jung, D.; Hong, S. J.; Kim, Y. S. Electrical and Surface Properties of Indium Tin Oxide (ITO) Films by Pulsed DC Magnetron Sputtering for Organic Light Emitting Diode as Anode Material. *Surf Coat Technol* **2010**, *205* (SUPPL. 1), S129–S132. https://doi.org/10.1016/J.SURFCOAT.2010.06.060.

(19) Yang, C. W.; Park, J. W. The Cohesive Crack and Buckle Delamination Resistances of Indium Tin Oxide (ITO) Films on Polymeric Substrates with Ductile Metal Interlayers. *Surf Coat Technol* **2010**, *204* (16–17), 2761–2766. https://doi.org/10.1016/J.SURFCOAT.2010.02.033.

(20) Peng, C.; Jia, Z.; Bianculli, D.; Li, T.; Lou, J. In Situ Electro-Mechanical Experiments and Mechanics Modeling of Tensile Cracking in Indium Tin Oxide Thin Films on Polyimide Substrates. *J Appl Phys* **2011**, *109* (10). https://doi.org/10.1063/1.3592341/984627.

(21) Kawajiri, K.; Tahara, K.; Uemiya, S. Lifecycle Assessment of Critical Material Substitution: Indium Tin Oxide and Aluminum Zinc Oxide in Transparent Electrodes. *Resources, Environment and Sustainability* **2022**, *7*, 100047. https://doi.org/10.1016/J.RESENV.2022.100047.

(22) Reina, A.; Jia, X.; Ho, J.; Nezich, D.; Son, H.; Bulovic, V.; Dresselhaus, M. S.; Jing, K. Large Area, Few-Layer Graphene Films on Arbitrary Substrates by Chemical Vapor Deposition. *Nano Lett* **2009**, *9* (1), 30–35. https://doi.org/10.1021/NL801827V/SUPPL_FILE/NL801827V_SI_003.PDF.

(23) Novoselov, K. S.; Geim, A. K.; Morozov, S. V.; Jiang, D.; Zhang, Y.; Dubonos, S. V.; Grigorieva, I. V.; Firsov, A. A. Electric Field in Atomically Thin Carbon Films. *Science (1979)* **2004**, *306* (5696), 666–669. https://doi.org/10.1126/SCIENCE.1102896/SUPPL_FILE/NOVOSELOV.SOM.PDF.

(24) Paton, K. R.; Varrla, E.; Backes, C.; Smith, R. J.; Khan, U.; O’Neill, A.; Boland, C.; Lotya, M.; Istrate, O. M.; King, P.; Higgins, T.; Barwich, S.; May, P.; Puczkarski, P.; Ahmed, I.; Moebius, M.; Pettersson, H.; Long, E.; Coelho, J.; O’Brien, S. E.; McGuire, E. K.; Sanchez, B. M.; Duesberg, G. S.; McEvoy, N.; Pennycook, T. J.; Downing, C.; Crossley, A.; Nicolosi, V.; Coleman, J. N. Scalable Production of Large Quantities of Defect-Free Few-

Layer Graphene by Shear Exfoliation in Liquids. *Nature Materials 2014 13:6* **2014**, *13* (6), 624–630. https://doi.org/10.1038/nmat3944.

(25) Sa, K.; Mahanandia, P. Conducting Reduced Graphene Oxide Film as Transparent Electrode. *Thin Solid Films* **2019**, *692*, 137594. https://doi.org/10.1016/J.TSF.2019.137594.

(26) Wang, S.; Tian, Y.; Wang, C.; Hang, C.; Huang, Y.; Liao, C. Chemical and Thermal Robust Tri-Layer RGO/Ag NWs/GO Composite Film for Wearable Heaters. *Compos Sci Technol* **2019**, *174*, 76–83. https://doi.org/10.1016/J.COMPSCITECH.2019.02.022.

(27) Nirmalraj, P. N.; Lyons, P. E.; De, S.; Coleman, J. N.; Boland, J. J. Electrical Connectivity in Single-Walled Carbon Nanotube Networks. *Nano Lett* **2009**, *9* (11), 3890–3895. https://doi.org/10.1021/NL9020914/SUPPL_FILE/NL9020914_SI_001.PDF.

(28) Fuhrer, M. S.; Nygård, J.; Shih, L.; Forero, M.; Yoon, Y. G.; Mazzoni, M. S. C.; Choi, H. J.; Ihm, J.; Louie, S. G.; Zettl, A.; McEuen, P. L. Crossed Nanotube Junctions. *Science (1979)* **2000**, *288* (5465), 494–497. https://doi.org/10.1126/SCIENCE.288.5465.494/SUPPL_FILE/1048209.XHTML.

(29) Tsapenko, A. P.; Goldt, A. E.; Shulga, E.; Popov, Z. I.; Maslakov, K. I.; Anisimov, A. S.; Sorokin, P. B.; Nasibulin, A. G. Highly Conductive and Transparent Films of HAuCl 4-Doped Single-Walled Carbon Nanotubes for Flexible Applications. **2018**. https://doi.org/10.1016/j.carbon.2018.01.016.

(30) Jiang, S.; Hou, P. X.; Chen, M. L.; Wang, B. W.; Sun, D. M.; Tang, D. M.; Jin, Q.; Guo, Q. X.; Zhang, D. D.; Du, J. H.; Tai, K. P.; Tan, J.; Kauppinen, E. I.; Liu, C.; Cheng, H. M. Ultrahigh-Performance Transparent Conductive Films of Carbon-Welded Isolated Single-Wall Carbon Nanotubes. *Sci Adv* **2018**, *4* (5).

https://doi.org/10.1126/SCIADV.AAP9264/SUPPL_FILE/AAP9264_SM.PDF.

(31) Li, M.; Wang, T.; Liu, X. Le; Bao, Z. L.; Qian, P. F.; Liu, K.; Shi, Y.; Ming, X.; Geng, H. Z. Highly Stable Phosphotungstic Acid/Au Dual Doped Carbon Nanotube Transparent Conductive Films for Transparent Flexible Heaters. *Carbon N Y* **2023**, *207*, 219–229. https://doi.org/10.1016/J.CARBON.2023.03.018.

(32) Gueye, M. N.; Carella, A.; Demadrille, R.; Simonato, J. P. All-Polymeric Flexible Transparent Heaters. *ACS Appl Mater Interfaces* **2017**, *9* (32), 27250–27256. https://doi.org/10.1021/ACSAMI.7B08578/ASSET/IMAGES/LARGE/AM-2017-085785_0004.JPEG.

(33) Dupont, S. R.; Novoa, F.; Voroshazi, E.; Dauskardt, R. H. Decohesion Kinetics of PEDOT:PSS Conducting Polymer Films. *Adv Funct Mater* **2014**, *24* (9), 1325–1332. https://doi.org/10.1002/ADFM.201302174.

(34) Kiebooms, R.; Aleshin, A.; Hutchison, K.; Wudl, F.; Heeger, A. Doped Poly(3,4-Ethylenedioxythiophene) Films: Thermal, Electromagnetical and Morphological Analysis. *Synth Met* **1999**, *101* (1–3), 436–437. https://doi.org/10.1016/S0379-6779(98)01121-7.

(35) Stepien, L.; Roch, A.; Tkachov, R.; Leupolt, B.; Han, L.; van Ngo, N.; Leyens, C. Thermal Operating Window for PEDOT:PSS Films and Its Related Thermoelectric Properties. *Synth Met* **2017**, *225*, 49–54. https://doi.org/10.1016/J.SYNTHMET.2016.11.017.

(36) Kim, W.; Kim, S.; Kang, I.; Jung, M. S.; Kim, S. J.; Kim, J. K.; Cho, S. M.; Kim, J. H.; Park, J. H. Hybrid Silver Mesh Electrode for ITO-Free Flexible Polymer Solar Cells with Good Mechanical Stability. *ChemSusChem* **2016**, *9* (9), 1042–1049. https://doi.org/10.1002/CSSC.201600070.

(37) Hwang, B. U.; Lee, J. H.; Trung, T. Q.; Roh, E.; Kim, D. Il; Kim, S. W.; Lee, N. E. Transparent Stretchable Self-Powered Patchable Sensor Platform with Ultrasensitive Recognition of Human Activities. *ACS Nano* **2015**, *9* (9), 8801–8810. https://doi.org/10.1021/ACSNANO.5B01835/ASSET/IMAGES/LARGE/NN-2015-01835H_0004.JPEG.

(38) Nguyen, V. H.; Papanastasiou, D. T.; Resende, J.; Bardet, L.; Sannicolo, T.; Jiménez, C.; Muñoz-Rojas, D.; Nguyen, N. D.; Bellet, D. Advances in Flexible Metallic Transparent Electrodes. *Small* **2022**, *18* (19), 2106006. https://doi.org/10.1002/SMLL.202106006.

(39) Lee, S. M.; Oh, S.; Chang, S. T. Highly Transparent, Flexible Conductors and Heaters Based on Metal Nanomesh Structures Manufactured Using an All-Water-Based Solution Process. *ACS Appl Mater Interfaces* **2019**, *11* (4), 4541–4550. https://doi.org/10.1021/ACSAMI.8B17415/ASSET/IMAGES/LARGE/AM-2018-17415Z_0008.JPEG.

(40) Li, Z.; Li, H.; Zhu, X.; Peng, Z.; Zhang, G.; Yang, J.; Wang, F.; Zhang, Y. F.; Sun, L.; Wang, R.; Zhang, J.; Yang, Z.; Yi, H.; Lan, H. Directly Printed Embedded Metal Mesh for Flexible Transparent Electrode via Liquid Substrate Electric-Field-Driven Jet. *Advanced Science* **2022**, *9* (14), 2105331. https://doi.org/10.1002/ADVS.202105331.

(41) Qi, X.; Zhou, J.; Zhu, X.; Li, H.; Zhang, G.; Sun, L.; Wang, R.; Huang, Y.; Yang, W.; Zhang, Y. F.; Li, Z.; Zhang, H.; Zhao, J.; Xu, Q.; Lan, H. Microscale Hybrid 3D Printed Ultrahigh Aspect Ratio Embedded Silver Mesh for Flexible Transparent Electrodes. *Materials Today Physics* **2023**, *33*, 101044. https://doi.org/10.1016/J.MTPHYS.2023.101044.

(42) Zhou, W.; Li, Y.; Li, P.; Chen, J.; Xu, R.; Yao, S.; Cui, Z.; Booth, R.; Mi, B.; Wang, D.; Ma, Y.; Huang, W. Metal Mesh as a Transparent

Omnidirectional Strain Sensor. *Adv Mater Technol* **2019**, *4* (4), 1800698. https://doi.org/10.1002/ADMT.201800698.

(43) Hu, L.; Wu, H.; Cui, Y. Metal Nanogrids, Nanowires, and Nanofibers for Transparent Electrodes. *MRS Bull* **2011**, *36* (10), 760–765. https://doi.org/10.1557/MRS.2011.234/FIGURES/4.

(44) Chang, Y.; Lye, M. L.; Zeng, H. C. Large-Scale Synthesis of High-Quality Ultralong Copper Nanowires. *Langmuir* **2005**, *21* (9), 3746–3748. https://doi.org/10.1021/LA050220W/SUPPL_FILE/LA050220WSI20050311_010814.PDF.

(45) Gall, K.; Diao, J.; Dunn, M. L. The Strength of Gold Nanowires. *Nano Lett* **2004**, *4* (12), 2431–2436. https://doi.org/10.1021/NL048456S/ASSET/IMAGES/LARGE/NL048456SF00004.JPEG.

(46) Sun, Y.; Gates, B.; Mayers, B.; Xia, Y. Crystalline Silver Nanowires by Soft Solution Processing. *Nano Lett* **2002**, *2* (2), 165–168. https://doi.org/10.1021/NL010093Y/ASSET/IMAGES/LARGE/NL010093YF00004.JPEG.

(47) Sharma, N.; Nair, N. M.; Nagasarvari, G.; Ray, D.; Swaminathan, P. A Review of Silver Nanowire-Based Composites for Flexible Electronic Applications. *Flexible and Printed Electronics* **2022**, *7* (1), 014009. https://doi.org/10.1088/2058-8585/AC5214.

(48) Li, X.; Wang, Y.; Yin, C.; Yin, Z. Copper Nanowires in Recent Electronic Applications: Progress and Perspectives. *J Mater Chem C Mater* **2020**, *8* (3), 849–872. https://doi.org/10.1039/C9TC04744A.

(49) Sun, Y.; Mayers, B.; Herricks, T.; Xia, Y. Polyol Synthesis of Uniform Silver Nanowires: A Plausible Growth Mechanism and the Supporting Evidence. *Nano Lett* **2003**, *3* (7), 955–960.

https://doi.org/10.1021/NL034312M/ASSET/IMAGES/LARGE/NL034312MF00005.JPEG.

(50) Sun, Y.; Yin, Y.; Mayers, B. T.; Herricks, T.; Xia, Y. Uniform Silver Nanowires Synthesis by Reducing AgNO3 with Ethylene Glycol in the Presence of Seeds and Poly(Vinyl Pyrrolidone). *Chemistry of Materials* **2002**, *14* (11), 4736–4745. https://doi.org/10.1021/CM020587B/ASSET/IMAGES/LARGE/CM020587BF00010.JPEG.

(51) Zeng, X. Y.; Zhang, Q. K.; Yu, R. M.; Lu, C. Z. A New Transparent Conductor: Silver Nanowire Film Buried at the Surface of a Transparent Polymer. *Advanced Materials* **2010**, *22* (40), 4484–4488. https://doi.org/10.1002/ADMA.201001811.

(52) Kim, S. H.; Choi, B. S.; Kang, K.; Choi, Y. S.; Yang, S. I. Low Temperature Synthesis and Growth Mechanism of Ag Nanowires. *J Alloys Compd* **2007**, *433* (1–2), 261–264. https://doi.org/10.1016/J.JALLCOM.2006.06.053.

(53) Bari, B.; Lee, J.; Jang, T.; Won, P.; Ko, S. H.; Alamgir, K.; Arshad, M.; Guo, L. J. Simple Hydrothermal Synthesis of Very-Long and Thin Silver Nanowires and Their Application in High Quality Transparent Electrodes. *J Mater Chem A Mater* **2016**, *4* (29), 11365–11371. https://doi.org/10.1039/C6TA03308C.

(54) Lu, J.; Yang, L.; Xie, A.; Shen, Y. DNA-Templated Photo-Induced Silver Nanowires: Fabrication and Use in Detection of Relative Humidity. *Biophys Chem* **2009**, *145* (2–3), 91–97. https://doi.org/10.1016/J.BPC.2009.09.005.

(55) Kumar, A.; Shaikh, M. O.; Chuang, C. H. Silver Nanowire Synthesis and Strategies for Fabricating Transparent Conducting Electrodes. *Nanomaterials 2021, Vol. 11, Page 693* **2021**, *11* (3), 693. https://doi.org/10.3390/NANO11030693.

(56) Coskun, S.; Aksoy, B.; Unalan, H. E. Polyol Synthesis of Silver Nanowires: An Extensive Parametric Study. *Cryst Growth Des* **2011**, *11* (11), 4963–4969. https://doi.org/10.1021/CG200874G/SUPPL_FILE/CG200874G_SI_001.PDF.

(57) Mayousse, C.; Celle, C.; Moreau, E.; Mainguet, J. F.; Carella, A.; Simonato, J. P. Improvements in Purification of Silver Nanowires by Decantation and Fabrication of Flexible Transparent Electrodes. Application to Capacitive Touch Sensors. *Nanotechnology* **2013**, *24* (21), 215501. https://doi.org/10.1088/0957-4484/24/21/215501.

(58) Li, B.; Ye, S.; Stewart, I. E.; Alvarez, S.; Wiley, B. J. Synthesis and Purification of Silver Nanowires to Make Conducting Films with a Transmittance of 99%. *Nano Lett* **2015**, *15* (10), 6722–6726. https://doi.org/10.1021/ACS.NANOLETT.5B02582/ASSET/IMAGES/LARGE/NL-2015-02582X_0002.JPEG.

(59) Jarrett, R.; Crook, R. Silver Nanowire Purification and Separation by Size and Shape Using Multi-Pass Filtration. *http://dx.doi.org/10.1179/1433075X15Y.0000000016* **2016**, *20* (2), 86–91. https://doi.org/10.1179/1433075X15Y.0000000016.

(60) Pradel, K. C.; Sohn, K.; Huang, J. Cross-Flow Purification of Nanowires. *Angewandte Chemie International Edition* **2011**, *50* (15), 3412–3416. https://doi.org/10.1002/ANIE.201100087.

(61) Li, W.; Zhang, H.; Shi, S.; Xu, J.; Qin, X.; He, Q.; Yang, K.; Dai, W.; Liu, G.; Zhou, Q.; Yu, H.; Silva, S. R. P.; Fahlman, M. Recent Progress in Silver Nanowire Networks for Flexible Organic Electronics. *J Mater Chem C Mater* **2020**, *8* (14), 4636–4674. https://doi.org/10.1039/C9TC06865A.

(62) Sahu, N.; Parija, B.; Panigrahi, S. Fundamental Understanding and Modeling of Spin Coating Process: A Review. *Indian Journal of Physics* **2009**, *83* (4), 493–502. https://doi.org/10.1007/S12648-009-0009-Z/METRICS.

(63) Sim, H.; Kim, C.; Bok, S.; Kim, M. K.; Oh, H.; Lim, G. H.; Cho, S. M.; Lim, B. Five-Minute Synthesis of Silver Nanowires and Their Roll-to-Roll Processing for Large-Area Organic Light Emitting Diodes. *Nanoscale* **2018**, *10* (25), 12087–12092. https://doi.org/10.1039/C8NR02242A.

(64) Zhang, S.; Liu, X.; Lin, T.; He, P. A Method to Fabricate Uniform Silver Nanowires Transparent Electrode Using Meyer Rod Coating and Dynamic Heating. *Journal of Materials Science: Materials in Electronics* **2019**, *30* (20), 18702–18709. https://doi.org/10.1007/S10854-019-02223-X/FIGURES/9.

(65) Scardaci, V.; Coull, R.; Lyons, P. E.; Rickard, D.; Coleman, J. N.; Scardaci, V.; Lyons, P. E.; Coleman, N.; Rickard, D. Spray Deposition of Highly Transparent, Low-Resistance Networks of Silver Nanowires over Large Areas. *Small* **2011**, *7* (18), 2621–2628. https://doi.org/10.1002/SMLL.201100647.

(66) Preston, C.; Xu, Y.; Han, X.; Munday, J. N.; Hu, L. Optical Haze of Transparent and Conductive Silver Nanowire Films. *Nano Res* **2013**, *6* (7), 461–468. https://doi.org/10.1007/S12274-013-0323-9/METRICS.

(67) Langley, D.; Giusti, G.; Mayousse, C.; Celle, C.; Bellet, D.; Simonato, J. P. Flexible Transparent Conductive Materials Based on Silver Nanowire Networks: A Review. *Nanotechnology* **2013**, *24* (45), 452001. https://doi.org/10.1088/0957-4484/24/45/452001.

(68) Xiong, J.; Li, S.; Ye, Y.; Wang, J.; Qian, K.; Cui, P.; Gao, D.; Lin, M.-F.; Chen, T.; See Lee, P.; Xiong, J. Q.; Li, S. H.; Wang, J. X.; Qian, K.; Cui, P.; Gao, D. C.; Lin, M.; Lee, P. S.; Ye, Y. Y.; Chen, T. P. A Deformable and Highly Robust Ethyl Cellulose Transparent Conductor with a Scalable Silver

Nanowires Bundle Micromesh. *Advanced Materials* **2018**, *30* (36), 1802803. https://doi.org/10.1002/ADMA.201802803.

(69) Gaynor, W.; Burkhard, G. F.; McGehee, M. D.; Peumans, P. Smooth Nanowire/Polymer Composite Transparent Electrodes. *Advanced Materials* **2011**, *23* (26), 2905–2910. https://doi.org/10.1002/ADMA.201100566.

(70) Haacke, G. New Figure of Merit for Transparent Conductors. *J Appl Phys* **1976**, *47* (9), 4086–4089. https://doi.org/10.1063/1.323240.

(71) Feng, X.; Wang, L.; Huang, Y. Y. S.; Luo, Y.; Ba, J.; Shi, H. T. H.; Pei, Y.; Zhang, S.; Zhang, Z.; Jia, X.; Lu, B. Cost-Effective Fabrication of Uniformly Aligned Silver Nanowire Microgrid-Based Transparent Electrodes with Higher than 99% Transmittance. *ACS Appl Mater Interfaces* **2022**, *14* (34), 39199–39210. https://doi.org/10.1021/ACSAMI.2C09672/SUPPL_FILE/AM2C09672_SI_004.MP4.

(72) Sohn, H.; Park, C.; Oh, J. M.; Kang, S. W.; Kim, M. J. Silver Nanowire Networks: Mechano-Electric Properties and Applications. *Materials 2019, Vol. 12, Page 2526* **2019**, *12* (16), 2526. https://doi.org/10.3390/MA12162526.

(73) Hu, L.; Kim, H. S.; Lee, J. Y.; Peumans, P.; Cui, Y. Scalable Coating and Properties of Transparent, Flexible, Silver Nanowire Electrodes. *ACS Nano* **2010**, *4* (5), 2955–2963. https://doi.org/10.1021/NN1005232/ASSET/IMAGES/LARGE/NN-2010-005232_0002.JPEG.

(74) Langley, D. P.; Lagrange, M.; Giusti, G.; Jiménez, C.; Bréchet, Y.; Nguyen, N. D.; Bellet, D. Metallic Nanowire Networks: Effects of Thermal Annealing on Electrical Resistance. *Nanoscale* **2014**, *6* (22), 13535–13543. https://doi.org/10.1039/C4NR04151H.

(75) Yu, X.; Liang, X.; Zhao, T.; Zhu, P.; Sun, R.; Wong, C. P. Thermally Welded Honeycomb-like Silver Nanowires Aerogel Backfilled with Polydimethylsiloxane for Electromagnetic Interference Shielding. *Mater Lett* **2021**, *285*, 129065. https://doi.org/10.1016/J.MATLET.2020.129065.

(76) Liang, C.; Sun, X.; Su, W.; Hu, Y.; Duan, J. Fast Welding of Silver Nanowires for Flexible Transparent Conductive Film by Spatial Light Modulated Femtosecond Laser. *Adv Eng Mater* **2021**, *23* (12), 2100584. https://doi.org/10.1002/ADEM.202100584.

(77) Hu, Y.; Liang, C.; Sun, X.; Zheng, J.; Duan, J.; Zhuang, X. Enhancement of the Conductivity and Uniformity of Silver Nanowire Flexible Transparent Conductive Films by Femtosecond Laser-Induced Nanowelding. *Nanomaterials 2019, Vol. 9, Page 673* **2019**, *9* (5), 673. https://doi.org/10.3390/NANO9050673.

(78) Song, T. Bin; Chen, Y.; Chung, C. H.; Yang, Y.; Bob, B.; Duan, H. S.; Li, G.; Tu, K. N.; Huang, Y. Nanoscale Joule Heating and Electromigration Enhanced Ripening of Silver Nanowire Contacts. *ACS Nano* **2014**, *8* (3), 2804–2811. https://doi.org/10.1021/NN4065567/SUPPL_FILE/NN4065567_SI_001.PDF.

(79) Seong, B.; Chae, I.; Lee, H.; Nguyen, V. D.; Byun, D. Spontaneous Self-Welding of Silver Nanowire Networks. *Physical Chemistry Chemical Physics* **2015**, *17* (12), 7629–7633. https://doi.org/10.1039/C5CP00035A.

(80) Garnett, E. C.; Cai, W.; Cha, J. J.; Mahmood, F.; Connor, S. T.; Greyson Christoforo, M.; Cui, Y.; McGehee, M. D.; Brongersma, M. L. Self-Limited Plasmonic Welding of Silver Nanowire Junctions. *Nature Materials 2012 11:3* **2012**, *11* (3), 241–249. https://doi.org/10.1038/nmat3238.

(81) Park, J. H.; Hwang, G. T.; Kim, S.; Seo, J.; Park, H. J.; Yu, K.; Kim, T. S.; Lee, K. J. Flash-Induced Self-Limited Plasmonic Welding of Silver

Nanowire Network for Transparent Flexible Energy Harvester. *Advanced Materials* **2017**, *29* (5). https://doi.org/10.1002/ADMA.201603473.

(82) Kang, H.; Song, S. J.; Sul, Y. E.; An, B. S.; Yin, Z.; Choi, Y.; Pu, L.; Yang, C. W.; Kim, Y. S.; Cho, S. M.; Kim, J. G.; Cho, J. H. Epitaxial-Growth-Induced Junction Welding of Silver Nanowire Network Electrodes. *ACS Nano* **2018**, *12* (5), 4894–4902. https://doi.org/10.1021/ACSNANO.8B01900/ASSET/IMAGES/LARGE/NN-2018-01900F_0004.JPEG.

(83) Kang, H.; Kim, Y.; Cheon, S.; Yi, G. R.; Cho, J. H. Halide Welding for Silver Nanowire Network Electrode. *ACS Appl Mater Interfaces* **2017**, *9* (36), 30779–30785. https://doi.org/10.1021/ACSAMI.7B09839/SUPPL_FILE/AM7B09839_SI_001.PDF.

(84) Ge, Y.; Liu, J.; Liu, X.; Hu, J.; Duan, X.; Duan, X. Rapid Electrochemical Cleaning Silver Nanowire Thin Films for High-Performance Transparent Conductors. *J Am Chem Soc* **2019**, *141* (31), 12251–12257. https://doi.org/10.1021/JACS.9B02497/ASSET/IMAGES/LARGE/JA-2019-024976_0006.JPEG.

(85) Tseng, J.-Y.; Lee, L.; Huang, Y.-C.; Chang, J.-H.; Su, T.-Y.; Shih, Y.-C.; Lin, H.-W.; Chueh, Y.-L.; Tseng, J.; Lee, L.; Huang, Y.; Chang, J.; Su, T.; Shih, Y.; Lin, H.; Chueh, Y. Pressure Welding of Silver Nanowires Networks at Room Temperature as Transparent Electrodes for Efficient Organic Light-Emitting Diodes. *Small* **2018**, *14* (38), 1800541. https://doi.org/10.1002/SMLL.201800541.

(86) Liu, Y.; Zhang, J.; Gao, H.; Wang, Y.; Liu, Q.; Huang, S.; Guo, C. F.; Ren, Z. Capillary-Force-Induced Cold Welding in Silver-Nanowire-Based Flexible Transparent Electrodes. *Nano Lett* **2017**, *17* (2), 1090–1096.

https://doi.org/10.1021/ACS.NANOLETT.6B04613/ASSET/IMAGES/LARGE/NL-2016-04613D_0004.JPEG.

(87) Xiong, W.; Liu, H.; Chen, Y.; Zheng, M.; Zhao, Y.; Kong, X.; Wang, Y.; Zhang, X.; Kong, X.; Wang, P.; Jiang, L.; Xiong, W. W.; Liu, H. L.; Zhang, X. Q.; Kong, X. Y.; Jiang, L.; Chen, Y. Z.; Kong, X. B.; Wang, Y.; Wang, F.; Zhao, Y. Y.; Zheng, M. L. Highly Conductive, Air-Stable Silver Nanowire@Iongel Composite Films toward Flexible Transparent Electrodes. *Advanced Materials* **2016**, *28* (33), 7167–7172. https://doi.org/10.1002/ADMA.201600358.

(88) Lu, H.; Zhang, D.; Cheng, J.; Liu, J.; Mao, J.; Choy, W. C. H. Locally Welded Silver Nano-Network Transparent Electrodes with High Operational Stability by a Simple Alcohol-Based Chemical Approach. *Adv Funct Mater* **2015**, *25* (27), 4211–4218. https://doi.org/10.1002/ADFM.201501004.

(89) Kim, Y.; Sul, Y. E.; Kang, H.; Choi, Y.; Lim, H. S.; Lee, S.; Pu, L.; Yi, G. R.; Cho, S. M.; Cho, J. H. Roll-to-Roll Redox-Welding and Embedding for Silver Nanowire Network Electrodes. *Nanoscale* **2018**, *10* (39), 18627–18634. https://doi.org/10.1039/C8NR01040D.

(90) Ge, Y.; Duan, X.; Zhang, M.; Mei, L.; Hu, J.; Hu, W.; Duan, X. Direct Room Temperature Welding and Chemical Protection of Silver Nanowire Thin Films for High Performance Transparent Conductors. *J Am Chem Soc* **2018**, *140* (1), 193–199. https://doi.org/10.1021/JACS.7B07851/SUPPL_FILE/JA7B07851_SI_001.PDF.

(91) Mao, H.; Feng, J.; Ma, X.; Wu, C.; Zhao, X. One-Dimensional Silver Nanowires Synthesized by Self-Seeding Polyol Process. *Journal of Nanoparticle Research* **2012**, *14* (6), 1–15. https://doi.org/10.1007/S11051-012-0887-4/FIGURES/14.

(92) Wang, M.; Cheng, J.; Li, M.; He, F. Raman Spectra of Soda–Lime–Silicate Glass Doped with Rare Earth. *Physica B Condens Matter* **2011**, *406* (20), 3865–3869. https://doi.org/10.1016/J.PHYSB.2011.07.014.

(93) Gao, X. Y.; Wang, S. Y.; Li, J.; Zheng, Y. X.; Zhang, R. J.; Zhou, P.; Yang, Y. M.; Chen, L. Y. Study of Structure and Optical Properties of Silver Oxide Films by Ellipsometry, XRD and XPS Methods. *Thin Solid Films* **2004**, *455–456*, 438–442. https://doi.org/10.1016/J.TSF.2003.11.242.

(94) Wang, Z. L.; Wang, A. C. On the Origin of Contact-Electrification. *Materials Today* **2019**, *30*, 34–51. https://doi.org/10.1016/J.MATTOD.2019.05.016.

(95) Fan, F. R.; Tian, Z. Q.; Lin Wang, Z. Flexible Triboelectric Generator. *Nano Energy* **2012**, *1* (2), 328–334. https://doi.org/10.1016/J.NANOEN.2012.01.004.

(96) Konda, A.; Prakash, A.; Moss, G. A.; Schmoldt, M.; Grant, G. D.; Guha, S. Aerosol Filtration Efficiency of Common Fabrics Used in Respiratory Cloth Masks. *ACS Nano* **2020**, *14* (5), 6339–6347. https://doi.org/10.1021/ACSNANO.0C03252/ASSET/IMAGES/MEDIUM/NN0C03252_M001.GIF.

(97) Camara, C. G.; Escobar, J. V.; Hird, J. R.; Putterman, S. J. Correlation between Nanosecond X-Ray Flashes and Stick–Slip Friction in Peeling Tape. *Nature 2008 455:7216* **2008**, *455* (7216), 1089–1092. https://doi.org/10.1038/nature07378.

(98) Hao, Y.; Zhang, Y.; Mensah, A.; Liao, S.; Lv, P.; Wei, Q. Scalable, Ultra-High Stretchable and Conductive Fiber Triboelectric Nanogenerator for Biomechanical Sensing. *Nano Energy* **2023**, *109*, 108291. https://doi.org/10.1016/J.NANOEN.2023.108291.

(99) Cho, S.; Lee, D.; Jang, S.; Cho, S.; Shim, J.; Jang, Y.; Lin, Z. H.; Choi, K.; Choi, D. Physical Intelligence-Based Working Mode Adaptable

Triboelectric Nanogenerator for Effective Wind Energy Harvesting in Broad Range. *Nano Energy* **2023**, *113*, 108608. https://doi.org/10.1016/J.NANOEN.2023.108608.

(100) Tan, D.; Zhou, J.; Wang, K.; Zhang, C.; Li, Z.; Xu, D. Wearable Bistable Triboelectric Nanogenerator for Harvesting Torsional Vibration Energy from Human Motion. *Nano Energy* **2023**, *109*, 108315. https://doi.org/10.1016/J.NANOEN.2023.108315.

(101) He, W.; Shan, C.; Fu, S.; Wu, H.; Wang, J.; Mu, Q.; Li, G.; Hu, C.; He, W.; Shan, C.; Fu, S.; Wu, H.; Wang, J.; Mu, Q.; Li, G.; Hu, C. Large Harvested Energy by Self-Excited Liquid Suspension Triboelectric Nanogenerator with Optimized Charge Transportation Behavior. *Advanced Materials* **2023**, *35* (7), 2209657. https://doi.org/10.1002/ADMA.202209657.

(102) Wang, W.; Zhang, L.; Wang, H.; Zhao, Y.; Cheng, J.; Meng, J.; Wang, D.; Liu, Y. High-Output Single-Electrode Droplet Triboelectric Nanogenerator Based on Asymmetrical Distribution Electrostatic Induction Enhancement. *Small* **2023**, 2301568. https://doi.org/10.1002/SMLL.202301568.

(103) So, M. Y.; Xu, B.; Li, Z.; Lai, C. L.; Jiang, C. Flexible Corrugated Triboelectric Nanogenerators for Efficient Biomechanical Energy Harvesting and Human Motion Monitoring. *Nano Energy* **2023**, *106*, 108033. https://doi.org/10.1016/J.NANOEN.2022.108033.

(104) Jung, H.; Friedman, B.; Hwang, W.; Copping, A.; Branch, R.; Deng, Z. D. Self-Powered Arctic Satellite Communication System by Harvesting Wave Energy Using a Triboelectric Nanogenerator. *Nano Energy* **2023**, *114*, 108633. https://doi.org/10.1016/J.NANOEN.2023.108633.

(105) Zhong, Y.; Wang, J.; Han, L.; Dai, S.; Zhu, H.; Hua, J.; Cheng, G.; Ding, J. High-Performance Flexible Self-Powered Triboelectric Pressure Sensor Based on Chemically Modified Micropatterned PDMS Film. *Sens Actuators A Phys* **2023**, *349*, 114013. https://doi.org/10.1016/J.SNA.2022.114013.

(106) Jin, T.; Sun, Z.; Li, L.; Zhang, Q.; Zhu, M.; Zhang, Z.; Yuan, G.; Chen, T.; Tian, Y.; Hou, X.; Lee, C. Triboelectric Nanogenerator Sensors for Soft Robotics Aiming at Digital Twin Applications. *Nature Communications 2020 11:1* **2020**, *11* (1), 1–12. https://doi.org/10.1038/s41467-020-19059-3.

(107) Zhang, H.; Zhang, D.; Wang, Z.; Xi, G.; Mao, R.; Ma, Y.; Wang, D.; Tang, M.; Xu, Z.; Luan, H. Ultrastretchable, Self-Healing Conductive Hydrogel-Based Triboelectric Nanogenerators for Human-Computer Interaction. *ACS Appl Mater Interfaces* **2023**, *15* (4), 5128–5138. https://doi.org/10.1021/ACSAMI.2C17904/ASSET/IMAGES/LARGE/AM2C17904_0008.JPEG.

(108) Park, S. J.; Lee, S. H.; Seol, M. L.; Jeon, S. B.; Bae, H.; Kim, D.; Cho, G. H.; Choi, Y. K. Self-Sustainable Wind Speed Sensor System with Omni-Directional Wind Based Triboelectric Generator. *Nano Energy* **2019**, *55*, 115–122. https://doi.org/10.1016/J.NANOEN.2018.10.063.

(109) Yang, H.; Lai, J.; Li, Q.; Zhang, X.; Li, X.; Yang, Q.; Hu, Y.; Xi, Y.; Wang, Z. L. High-Sensitive and Ultra-Wide Spectrum Multifunctional Triboelectric Acoustic Sensor for Broad Scenario Applications. *Nano Energy* **2022**, *104*, 107932. https://doi.org/10.1016/J.NANOEN.2022.107932.

(110) Lin, Z.-H.; Cheng, G.; Lin, L.; Lee, S.; Lin Wang, Z.; Lin, Z.; Cheng, G.; Lin, L.; Lee, S.; Wang, Z. L. Water–Solid Surface Contact Electrification and Its Use for Harvesting Liquid-Wave Energy. *Angewandte Chemie International Edition* **2013**, *52* (48), 12545–12549. https://doi.org/10.1002/ANIE.201307249.

(111) Cai, C.; Luo, B.; Liu, Y.; Fu, Q.; Liu, T.; Wang, S.; Nie, S. Advanced Triboelectric Materials for Liquid Energy Harvesting and Emerging Application. *Materials Today* **2022**, *52*, 299–326. https://doi.org/10.1016/J.MATTOD.2021.10.034.

(112) Nie, J.; Ren, Z.; Xu, L.; Lin, S.; Zhan, F.; Chen, X.; Lin Wang, Z.; Nie, J.; Ren, Z.; Xu, L.; Lin, S.; Zhan, F.; Chen, X.; Wang, Z. L. Probing Contact-Electrification-Induced Electron and Ion Transfers at a Liquid–Solid Interface. *Advanced Materials* **2020**, *32* (2), 1905696. https://doi.org/10.1002/ADMA.201905696.

(113) Lin, S.; Xu, L.; Chi Wang, A.; Wang, Z. L. Quantifying Electron-Transfer in Liquid-Solid Contact Electrification and the Formation of Electric Double-Layer. *Nature Communications 2020 11:1* **2020**, *11* (1), 1–8. https://doi.org/10.1038/s41467-019-14278-9.

(114) Zou, H.; Zhang, Y.; Guo, L.; Wang, P.; He, X.; Dai, G.; Zheng, H.; Chen, C.; Wang, A. C.; Xu, C.; Wang, Z. L. Quantifying the Triboelectric Series. *Nature Communications 2019 10:1* **2019**, *10* (1), 1–9. https://doi.org/10.1038/s41467-019-09461-x.

(115) Yoo, D.; Jang, S.; Cho, S.; Choi, D.; Kim, D. S. A Liquid Triboelectric Series. *Advanced Materials* **2023**, *35* (26), 2300699. https://doi.org/10.1002/ADMA.202300699.

(116) Hu, S.; Shi, Z.; Zheng, R.; Ye, W.; Gao, X.; Zhao, W.; Yang, G. Superhydrophobic Liquid-Solid Contact Triboelectric Nanogenerator as a Droplet Sensor for Biomedical Applications. *ACS Appl Mater Interfaces* **2020**, *12* (36), 40021–40030. https://doi.org/10.1021/ACSAMI.0C10097/ASSET/IMAGES/LARGE/AM0C10097_0006.JPEG.

(117) Xu, W.; Zheng, H.; Liu, Y.; Zhou, X.; Zhang, C.; Song, Y.; Deng, X.; Leung, M.; Yang, Z.; Xu, R. X.; Wang, Z. L.; Zeng, X. C.; Wang, Z. A Droplet-Based Electricity Generator with High Instantaneous Power Density. *Nature 2020 578:7795* **2020**, *578* (7795), 392–396. https://doi.org/10.1038/s41586-020-1985-6.

(118) Hu, S.; Ding, X.; Fan, B.; Zhang, C.; Zhang, B.; Shi, X.; Peng, Z. Position Sensing of Jetting Droplets Enabled by Triboelectric Nanogenerators. *Nano Energy* **2023**, *109*, 108289. https://doi.org/10.1016/J.NANOEN.2023.108289.

(119) Kil Yun, B.; Soo Kim, H.; Joon Ko, Y.; Murillo, G.; Hoon Jung, J. Interdigital Electrode Based Triboelectric Nanogenerator for Effective Energy Harvesting from Water. *Nano Energy* **2017**, *36*, 233–240. https://doi.org/10.1016/J.NANOEN.2017.04.048.

(120) Farahmand Nejad, M. A.; Ranjbar, S.; Parolo, C.; Nguyen, E. P.; Álvarez-Diduk, R.; Hormozi-Nezhad, M. R.; Merkoçi, A. Electrochromism: An Emerging and Promising Approach in (Bio)Sensing Technology. *Materials Today* **2021**, *50*, 476–498. https://doi.org/10.1016/J.MATTOD.2021.06.015.

(121) Kammen, D. M.; Sunter, D. A. City-Integrated Renewable Energy for Urban Sustainability. *Science (1979)* **2016**, *352* (6288), 922–928. https://doi.org/10.1126/SCIENCE.AAD9302.

(122) Wang, J. L.; Sheng, S. Z.; He, Z.; Wang, R.; Pan, Z.; Zhao, H. Y.; Liu, J. W.; Yu, S. H. Self-Powered Flexible Electrochromic Smart Window. *Nano Lett* **2021**, *21* (23), 9976–9982. https://doi.org/10.1021/ACS.NANOLETT.1C03438/ASSET/IMAGES/LARGE/NL1C03438_0005.JPEG.

(123) Granqvist, C. G. Out of a Niche. *Nature Materials 2006 5:2* **2006**, *5* (2), 89–90. https://doi.org/10.1038/nmat1577.

(124) Zhao, Q.; Fang, Y.; Qiao, K.; Wei, W.; Yao, Y.; Gao, Y. Printing of WO3/ITO Nanocomposite Electrochromic Smart Windows. *Solar Energy Materials and Solar Cells* **2019**, *194*, 95–102. https://doi.org/10.1016/J.SOLMAT.2019.02.002.

(125) Sivakumar, R.; Gopalakrishnan, R.; Jayachandran, M.; Sanjeeviraja, C. Investigation of X-Ray Photoelectron Spectroscopic (XPS), Cyclic

Voltammetric Analyses of WO3 Films and Their Response in FTO/WO3/Electrolyte/FTO Cells. *Smart Mater Struct* **2006**, *15* (3), 877. https://doi.org/10.1088/0964-1726/15/3/025.

(126) Ko, J. H.; Yeo, S.; Park, J. H.; Choi, J.; Noh, C.; Son, S. U. Graphene -Based Electrochromic Systems: The Case of Prussian Blue Nanoparticles on Transparent Graphene Film. *Chemical Communications* **2012**, *48* (32), 3884–3886. https://doi.org/10.1039/C2CC30161J.

(127) Kandpal, S.; Ghosh, T.; Rani, C.; Tanwar, M.; Sharma, M.; Rani, S.; Pathak, D. K.; Bhatia, R.; Sameera, I.; Jayabalan, J.; Kumar, R. Bifunctional Application of Viologen-MoS2-CNT/Polythiophene Device as Electrochromic Diode and Half-Wave Rectifier. *ACS Materials Au* **2021**, *2*, 300. https://doi.org/10.1021/ACSMATERIALSAU.1C00064/SUPPL_FILE/MG1C00064_SI_002.MP4.

(128) Fan, Q.; Fan, H.; Li, K.; Hou, C.; Zhang, Q.; Li, Y.; Wang, H.; Fan, Q.; Li, K.; Hou, C.; Wang, H.; Fan, H.; Zhang, Q.; Li, Y. Stretchable, Electrochemically-Stable Electrochromic Devices Based on Semi-Embedded Ag@Au Nanowire Network. *Small* **2023**, *19* (22), 2208234. https://doi.org/10.1002/SMLL.202208234.

(129) Zhou, D.; Xie, D.; Xia, X.; Wang, X.; Gu, C.; Tu, J. All-Solid-State Electrochromic Devices Based on WO3||NiO Films: Material Developments and Future Applications. *Sci China Chem* **2017**, *60* (1), 3–12. https://doi.org/10.1007/S11426-016-0279-3/METRICS.

(130) Cai, G.; Wang, J.; Lee, P. S. Next-Generation Multifunctional Electrochromic Devices. *Acc Chem Res* **2016**, *49* (8), 1469–1476. https://doi.org/10.1021/ACS.ACCOUNTS.6B00183/ASSET/IMAGES/LARGE/AR-2016-00183H_0008.JPEG.

(131) Bayzi Isfahani, V.; Silva, M. M. Fundamentals and Advances of Electrochromic Systems: A Review. *Adv Eng Mater* **2021**, *23* (12), 2100567. https://doi.org/10.1002/ADEM.202100567.

(132) Madasamy, K.; Velayutham, D.; Suryanarayanan, V.; Kathiresan, M.; Ho, K. C. Viologen-Based Electrochromic Materials and Devices. *J Mater Chem C Mater* **2019**, *7* (16), 4622–4637. https://doi.org/10.1039/C9TC00416E.

(133) Wang, Z.; Liu, R. PEDOT:PSS-Based Electrochromic Materials for Flexible and Stretchable Devices. *Materials Today Electronics* **2023**, *4*, 100036. https://doi.org/10.1016/J.MTELEC.2023.100036.

(134) Kawahara, J.; Ersman, P. A.; Engquist, I.; Berggren, M. Improving the Color Switch Contrast in PEDOT:PSS-Based Electrochromic Displays. *Org Electron* **2012**, *13* (3), 469–474. https://doi.org/10.1016/J.ORGEL.2011.12.007.

(135) Xie, H.; Wang, Z.; Khalifa, M. A.; Ke, Y.; Zheng, J.; Xu, C. Proton and Redox Couple Synergized Strategy for Aqueous Low Voltage-Driven WO 3 Electrochromic Devices . *ACS Appl Mater Interfaces* **2023**, *15* (25), 30469–30478. https://doi.org/10.1021/ACSAMI.3C04442/ASSET/IMAGES/LARGE/AM3C04442_0007.JPEG.

(136) Wang, J.; Zhu, R.; Gao, Y.; Jia, Y.; Cai, G. Unveiling the Multistep Electrochemical Desorption Mechanism of Cubic NiO Films for Transmissive-to-Black Electrochromic Energy Storage Devices. *Journal of Physical Chemistry Letters* **2023**, *14* (9), 2284–2291. https://doi.org/10.1021/ACS.JPCLETT.3C00050/ASSET/IMAGES/LARGE/JZ3C00050_0005.JPEG.

(137) Zhang, W.; Li, H.; Al-Hussein, M.; Elezzabi, A. Y.; Zhang, W.; Li, H.; Elezzabi, A. Y.; Al-Hussein, M. Electrochromic Battery Displays with Energy Retrieval Functions Using Solution-Processable Colloidal Vanadium

Oxide Nanoparticles. *Adv Opt Mater* **2020**, *8* (2), 1901224. https://doi.org/10.1002/ADOM.201901224.

(138) Han, Q.; Wang, R.; Zhu, H.; Wan, M.; Mai, Y. The Preparation and Investigation of All Thin Film Electrochromic Devices Based on Reactively Sputtered MoO3 Thin Films. *Mater Sci Semicond Process* **2021**, *126*, 105686. https://doi.org/10.1016/J.MSSP.2021.105686.

(139) Chen, P. W.; Chang, C. Te; Ko, T. F.; Hsu, S. C.; Li, K. D.; Wu, J. Y. Fast Response of Complementary Electrochromic Device Based on WO3/NiO Electrodes. *Scientific Reports 2020 10:1* **2020**, *10* (1), 1–12. https://doi.org/10.1038/s41598-020-65191-x.

(140) Monk, P. M. S.; Mortimer, R. J.; Rosseinsky, D. R. Electrochromism and Electrochromic Devices. *Electrochromism and Electrochromic Devices* **2007**, *9780521822695*, 1–488. https://doi.org/10.1017/CBO9780511550959.

(141) Gu, C.; Jia, A. B.; Zhang, Y. M.; Zhang, S. X. A. Emerging Electrochromic Materials and Devices for Future Displays. *Chem Rev* **2022**, *122* (18), 14679–14721. https://doi.org/10.1021/ACS.CHEMREV.1C01055/ASSET/IMAGES/LARGE/CR1C01055_0032.JPEG.

(142) Liu, Q.; Dong, G.; Chen, Q.; Guo, J.; Xiao, Y.; Delplancke-Ogletree, M. P.; Reniers, F.; Diao, X. Charge-Transfer Kinetics and Cyclic Properties of Inorganic All-Solid-State Electrochromic Device with Remarkably Improved Optical Memory. *Solar Energy Materials and Solar Cells* **2018**, *174*, 545–553. https://doi.org/10.1016/J.SOLMAT.2017.09.012.

(143) Tutel, Y.; Koylan, S.; Tunca, S.; Unalan, H. E. Nanometer-Thick Mn:NiO and Co:NiO Films for High Performance Nonenzymatic Biosensors. *ACS Appl Nano Mater* **2021**, *4* (12), 13871–13883. https://doi.org/10.1021/ACSANM.1C03221/ASSET/IMAGES/LARGE/AN1C03221_0007.JPEG.

(144) Kim, D. J.; Pyun, S. Il; Choi, Y. M. A Study on the Hydrogen Intercalation into Rf-Magnetron Sputtered Amorphous WO3 Film Using Cyclic Voltammetry Combined with Electrochemical Quartz Crystal Microbalance Technique. *Solid State Ion* **1998**, *109* (1–2), 81–87. https://doi.org/10.1016/S0167-2738(98)00099-X.

(145) Huang, S.; Liu, Y.; Jafari, M.; Siaj, M.; Wang, H.; Xiao, S.; Ma, D.; Huang, S.; Liu, Y.; Ma, D.; Jafari, M.; Siaj, M.; Wang, H.; Xiao, S. Highly Stable Ag–Au Core–Shell Nanowire Network for ITO-Free Flexible Organic Electrochromic Device. *Adv Funct Mater* **2021**, *31* (14), 2010022. https://doi.org/10.1002/ADFM.202010022.

(146) Chang, C. M.; Chiang, Y. C.; Cheng, M. H.; Lin, S. H.; Jian, W. Bin; Chen, J. T.; Cheng, Y. J.; Ma, Y. R.; Tsukagoshi, K. Fabrication of WO3 Electrochromic Devices Using Electro-Exploding Wire Techniques and Spray Coating. *Solar Energy Materials and Solar Cells* **2021**, *223*, 110960. https://doi.org/10.1016/J.SOLMAT.2021.110960.

(147) Zhou, Z.; Chen, Z.; Ma, D.; Wang, J. Porous WO3·2H2O Film with Large Optical Modulation and High Coloration Efficiency for Electrochromic Smart Window. *Solar Energy Materials and Solar Cells* **2023**, *253*, 112226. https://doi.org/10.1016/J.SOLMAT.2023.112226.

(148) Park, Y. T.; Lee, S. H.; Lee, K. T. Electrochromic Properties of Silver Nanowire-Embedded Tungsten Trioxide Thin Films Fabricated by Electrodeposition. *Ceram Int* **2020**, *46* (18), 29052–29059. https://doi.org/10.1016/J.CERAMINT.2020.08.076.

(149) Wen-Cheun Au, B.; Chan, K. Y.; Knipp, D. Effect of Film Thickness on Electrochromic Performance of Sol-Gel Deposited Tungsten Oxide (WO3). *Opt Mater (Amst)* **2019**, *94*, 387–392. https://doi.org/10.1016/J.OPTMAT.2019.05.051.

(150) Shen, L.; Du, L.; Tan, S.; Zang, Z.; Zhao, C.; Mai, W. Flexible Electrochromic Supercapacitor Hybrid Electrodes Based on Tungsten Oxide Films and Silver Nanowires. *Chemical Communications* **2016**, *52* (37), 6296–6299. https://doi.org/10.1039/C6CC01139J.

(151) Zheng, J.; Zhao, Y.; Chen, L.; Zheng, Y.; Wang, X.; Xu, G.; Xiao, X. Unveiling the Function and Mechanism of the Ordered Alignment Silver Nanowires on Boosting the Electrochromic Performance. *Chemical Engineering Journal* **2023**, *463*, 142524. https://doi.org/10.1016/J.CEJ.2023.142524.

APPENDICES

A. Supporting information for Chapter 4

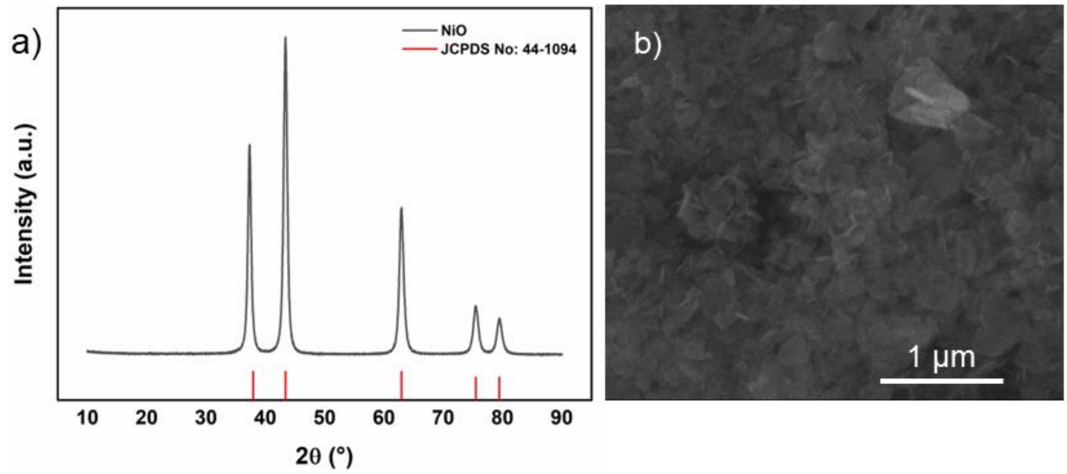

Figure A. 2 a) The XRD pattern and b) the SEM images from NiO nanoparticles

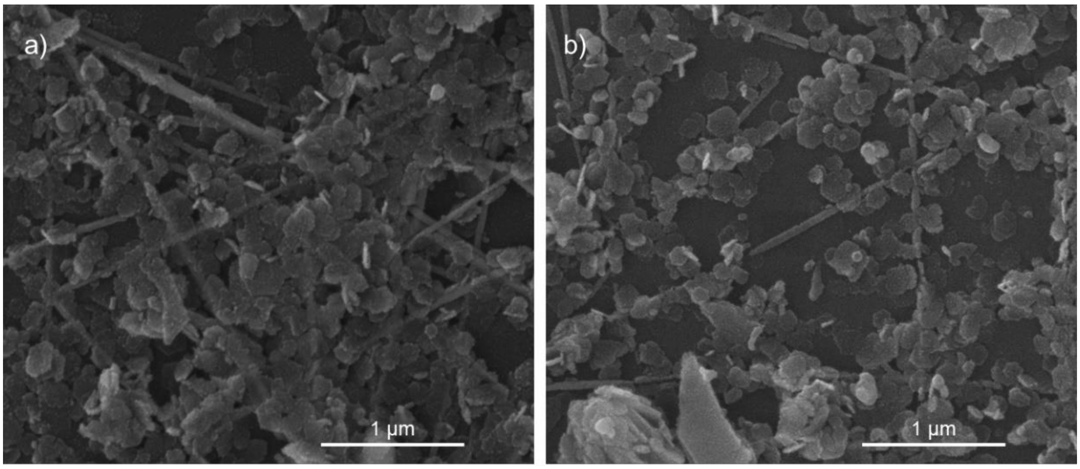

Figure A. 1 SEM images from NiO/AgNW electrodes a) As-deposited and b) degraded after CV.